

Stephen F. Austin State University

SFA ScholarWorks

Electronic Theses and Dissertations

5-2020

Characterization of Surface Karst Using LiDAR and Field Traverses, Fort Hood Military Installation, Coryell County, Texas

Heather Jaclyn Dailey

Stephen F Austin State University, daileyhj@jacks.sfasu.edu

Follow this and additional works at: <https://scholarworks.sfasu.edu/etds>



Part of the [Geology Commons](#), [Geomorphology Commons](#), and the [Speleology Commons](#)

Tell us how this article helped you.

Repository Citation

Dailey, Heather Jaclyn, "Characterization of Surface Karst Using LiDAR and Field Traverses, Fort Hood Military Installation, Coryell County, Texas" (2020). *Electronic Theses and Dissertations*. 297.

<https://scholarworks.sfasu.edu/etds/297>

This Thesis is brought to you for free and open access by SFA ScholarWorks. It has been accepted for inclusion in Electronic Theses and Dissertations by an authorized administrator of SFA ScholarWorks. For more information, please contact cdsscholarworks@sfasu.edu.

Characterization of Surface Karst Using LiDAR and Field Traverses, Fort Hood Military Installation, Coryell County, Texas

Creative Commons License



This work is licensed under a [Creative Commons Attribution-Noncommercial-No Derivative Works 4.0 License](https://creativecommons.org/licenses/by-nc-nd/4.0/).

**Characterization of Surface Karst Using LiDAR and Field Traverses,
Fort Hood Military Installation, Coryell County, Texas**

By

Heather Dailey, Bachelor of Science

Presented to the Faculty of the Graduate School of

Stephen F. Austin State University

In Partial Fulfillment

Of the Requirements

For the Degree of

Master of Science

Stephen F. Austin State University

May 2020

**Characterization of Surface Karst Using LiDAR and Field Traverses,
Fort Hood Military Installation, Coryell County, Texas**

By

Heather Dailey, Bachelor of Science

APPROVED:

Dr. Melinda Faulkner, Thesis Director

Dr. Kevin Stafford, Committee Member

Dr. I-Kuai Hung, Committee Member

Dr. Daniel Unger, Committee Member

Pauline M. Sampson, Ph. D.
Dean of Research and Graduate Studies

ABSTRACT

The Fort Hood Military Installation is a karst landscape that has been significantly altered for training exercises that include heavy vehicle maneuvers and simulated combat. Traditional karst surveys are often time-consuming and require extensive field analyses to adequately characterize large areas. Bias is given to areas that are most easily accessible and false negatives are common. Previous studies conducted in the eastern and western portion of the base have understated the abundance and spatial distribution of karst, particularly in the western portion.

This study used field traverses and 0.5-meter Light Detection and Ranging (LiDAR) data to characterize surface karst depressions, create a set of new and refined filters and buffering mechanisms to remove non-karst depressions, and determine the accuracy of the model. LiDAR data was used to create a digital elevation model (DEM), which was used to extract areas with localized depressions at a sub-meter scale. In order to isolate features that were formed through karst processes, data were processed through a series of filters with parameters based on features found during traverse surveys.

Field verifications to assess the accuracy of the LiDAR conducted with previous filters and buffering mechanisms had an overall accuracy of 77.3%,

indicating this model overestimated the number of features in the study area. To assess the accuracy of the new filters and buffering parameters, field verified features from a random point survey and a remote verification survey of features within each of the filters was conducted. The overall accuracy was 84.1%, indicating that the new filters and buffering parameters improved depression characterization and the ability to determine those features that were influenced by natural and anthropogenic processes.

ACKNOWLEDGEMENTS

This project could not have been done without the help of a lot of people who have each played very important roles. I am very appreciative to the Fort Hood Natural Resource Management Branch, specifically Charles Pekins, for providing awareness about Fort Hood and allowing access to the installation and the GIS data. I would like to thank my fellow geology students: Colby Reece, Melanie Ertons, Andrew Henry, Andrew Brillion, and Annie Robison for their help during long hours in the field. I also want to thank my committee members: Dr. Kevin Stafford, Dr. I-Kuai Hung, and Dr. Daniel Unger for all their contributions and dedication to this project. I also want to thank the Department of Geology at Stephen F. Austin for access to their facilities and the department vehicle for the many trips. My family is forever my support group that is there to help me reach my life goals. They always did everything they could to lend a helping hand whether it was giving me uplifting advice or unconditional love and I can't thank them enough. Finally, I would like to acknowledge my thesis advisor, Dr. Melinda Faulkner, for her constant encouragement and guidance. Thank you for always being there through all the good and bad times, but most of all for constantly believing in me.

TABLE OF CONTENTS

ABSTRACT	i
ACKNOWLEDGEMENTS	iii
TABLE OF CONTENTS	iv
LIST OF FIGURES	vi
LIST OF TABLES	xii
LIST OF EQUATIONS.....	xiii
PREFACE.....	xiv
ABSTRACT	1
INTRODUCTION	3
LITERATURE REVIEW	8
Regional Setting.....	8
Karst Development.....	12
Previous Karst Studies	14
METHODOLOGY	19
Field Traverses	19
Geographic Information Systems	30
Light Detection and Ranging	31
LAS Dataset and DEM	36
Depression Identification.....	42
Geometric Properties of Depressions.....	45
Depression Classification	49
RESULTS.....	70
Sinkhole Morphology and Lineament Analyses.....	70
Depression Density and Surface Area	75

Accuracy Assessment	78
Remote Verification	86
DISCUSSION	92
CONCLUSIONS	99
FUTURE WORK.....	101
REFERENCES	102
APPENDIX (A) DATA	106
TRAVERSE FEATURES IDENTIFIED	106
Traverse 1	106
Traverse 2.....	107
Traverse 3.....	107
VITA	113

LIST OF FIGURES

Figure 1: The location and extent of Fort Hood Military Installation. The eastern and western portions of Fort Hood are separated by the impact range. The study area is located in western Fort Hood.....	4
Figure 2: The location and extent of the study area within the western portion of Fort Hood Military Installation. There are major roads that have been built in order for military personnel and equipment to travel through the training areas.....	6
Figure 3: Physiographic map of Texas showing the ecoregions and location of Fort Hood Military Installation.....	9
Figure 4: Geologic map and stratigraphic column (from Faulkner, 2016) showing the units present in the study area.....	11
Figure 5: Spatial distribution of known karst features identified in Fort Hood.....	15
Figure 6: Map showing the previous areas where karst studies have been conducted within Fort Hood Military Installation.....	16
Figure 7: Location and extent of the three north-south traverse-based survey sections running through the eastern, middle, and western portions of the study area. The enlarged region shows the 10 m spacing spatial distribution of the traverse lines in the traverse-based survey. The DOQQ digital aerial imagery was collected by the National Agriculture Imagery Program during the 2018 agricultural growing season and through the winter and spring of 2019. They were downloaded from the Texas Natural Resources Information Systems on August 30, 2019.....	20
Figure 8: The karst features identified during the traverse-based survey. Many of the features are found in high elevated regions. The DOQQ digital aerial imagery was collected by the National Agriculture Imagery Program during the 2018 agricultural growing season and through the winter and spring of 2019.	22

They were downloaded from the Texas Natural Resources Information Systems on August 30, 2019.....	
Figure 9: An example of a collapsed feature found during the traverse-based survey.....	23
Figure 10: An example of a bowl like depression resulting from the subsidence of the ground.....	24
Figure 11: An example of a shelter cave found during the traverse-based survey.....	26
Figure 12: An example of a root hole (solutional conduit) found during the traverse-based survey.....	27
Figure 13: Diagram showing the data collection process for airborne surveys (Kao et. al., 2005).....	33
Figure 14: LiDAR grid tiles for all of Fort Hood Military Installation from the LiDAR survey acquired from the Natural Resources Management Branch.....	35
Figure 15: LiDAR grid tiles from the LiDAR survey acquired from the Natural Resources Management Branch that contain the study area.....	37
Figure 16: LAS Dataset Toolbar options as seen in ArcMap for Desktop V. 10.6.....	39
Figure 17: A screenshot of the LAS Dataset to Raster tool parameters. Interpolation type: Triangulation, Interpolation Method: Natural Neighbor, Sampling Type: Cell Size.....	41
Figure 18: A 0.5-meter resolution digital elevation model of the study area created from ground returns.....	43
Figure 19: A) Fill difference DEM displaying delineated features. B) Fill difference DEM converted to integer displaying only depressions that are greater than the 0.08 m vertical accuracy. C) Polygon features created by running the <i>Raster to Polygon</i> tool. D) Polygons of delineated features with 0.5 m buffer, dissolved, smoothed, and simplified.....	46
Figure 20: Flow chart for delineating features from the DEM and gathering geometric properties such as length, width, depth, etc.....	47

Figure 21: Map showing the extent of the Edwards and Comanche Peak formations, which are the only two formations within the study area that are susceptible to karst development.....	50
Figure 22: A map showing the stream network that was created using the <i>Flow Accumulation</i> tool. The DOQQ digital aerial imagery was collected by the National Agriculture Imagery Program during the 2018 agricultural growing season and through the winter and spring of 2019. They were downloaded from the Texas Natural Resources Information Systems on August 30, 2019.....	52
Figure 23: A slope analysis map used to characterize streams as major or minor streams based on slope breaks.....	53
Figure 24: A map showing the major and minor streams filters. The DOQQ digital aerial imagery was collected by the National Agriculture Imagery Program during the 2018 agricultural growing season and through the winter and spring of 2019. They were downloaded from the Texas Natural Resources Information Systems on August 30, 2019.....	54
Figure 25: A map showing the water bodies that were digitized using the 60-centimeter high resolution digital aerial image. The imagery was collected by the National Agriculture Imagery Program during the 2018 agricultural growing season and through the winter and spring of 2019. They were downloaded from the Texas Natural Resources Information Systems on August 30, 2019.....	56
Figure 26: A slope analysis map used to digitize the full extent of water bodies to help characterize them into water bodies with an area greater than 1000 m ² and water bodies with an area less than 1000 m ²	57
Figure 27: A map showing the water bodies with an area greater than 1000 m ² and water bodies with an area less than 1000 m ² . The DOQQ digital aerial imagery was collected by the National Agriculture Imagery Program during the 2018 agricultural growing season and through the winter and spring of 2019. They were downloaded from the Texas Natural Resources Information Systems on August 30, 2019.....	58
Figure 28: A map showing the paved and unpaved major roads delineated. The DOQQ digital aerial imagery was collected by the National Agriculture	

Imagery Program during the 2018 agricultural growing season and through the winter and spring of 2019. They were downloaded from the Texas Natural Resources Information Systems on August 30, 2019.....	60
Figure 29: Minor roads delineated through digitization using 60-centimeter high resolution digital aerial imagery. The DOQQ digital aerial imagery was collected by the National Agriculture Imagery Program during the 2018 agricultural growing season and through the winter and spring of 2019. They were downloaded from the Texas Natural Resources Information Systems on August 30, 2019.....	62
Figure 30: Intensity values for bare ground and disturbed vegetation were determined using the above intensity image that was acquired from the LiDAR survey data acquired by the Natural Resources Management Branch at Fort Hood.....	63
Figure 31: Landcover map showing the areas of healthy vegetation, bare ground, and disturbed vegetation. An existing vegetation map was updated using digital aerial imagery from TNRIS and the intensity images acquired with the LiDAR survey from the Natural Resource Management Branch at Fort Hood.....	65
Figure 32: A figure illustrating the purpose of removing artificially inflated artifacts with an area less than 4m ² as a result of processing.....	66
Figure 33: A map showing the remaining 4,886 potential features after the depression classification process. The DOQQ digital aerial imagery was collected by the National Agriculture Imagery Program during the 2018 agricultural growing season and through the winter and spring of 2019. They were downloaded from the Texas Natural Resources Information Systems on August 30, 2019.....	69
Figure 34: A graph plotting all features remaining after the filtering mechanisms were applied (n=1,253). The width vs length ratio in the potential karst features where length represents the major axis. The lower trend represents circular shaped features (L/W = 1) and the upper trend represents elliptical shaped features (L/W = 2).....	71

Figure 35: Histogram showing the circularity distribution of potential features with an area greater than 10 m ² (n=1,253). Many of the points are within the circular shape and have an average circularity ration of 1.55:1	73
Figure 36: A rose diagram representing the orientations of the major axis of features with an area greater than 10 m ² (n=1,253).....	74
Figure 37: Depression density map for all delineated depressions within the database (n = 60,437).....	76
Figure 38: Depression density map of non-interfering depressions after filtering (n = 4,886).....	77
Figure 39: Surface area density map for all delineated depressions within the database (n = 60,437).....	79
Figure 40: Surface area density map for all non-interfering depressions after filtering (n = 4,886).....	80
Figure 41: A previously mapped feature in the study area from Brokeback Cave.....	81
Figure 42: Map showing the location of the location of the random evaluation points (n=110). The DOQQ digital aerial imagery was collected by the National Agriculture Imagery Program during the 2018 agricultural growing season and through the winter and spring of 2019. They were downloaded from the Texas Natural Resources Information Systems on August 30, 2019.....	83
Figure 43: Map showing the location of the random evaluation points that were verified as true and false features with the new filters and buffering parameters (n=107) The DOQQ digital aerial imagery was collected by the National Agriculture Imagery Program during the 2018 agricultural growing season and through the winter and spring of 2019. They were downloaded from the Texas Natural Resources Information Systems on August 30, 2019.....	85
Figure 44: A subsidence feature that was detected by the LiDAR survey and verified during the random point sample survey and agreed with both sets of filters and buffering parameters.....	87

Figure 45: An example of a feature that was delineated during the depression identification process, but removed by the water body filter in both sets of filters and buffering parameters.....	88
Figure 46: Map showing the location of the remote verification points (n=111). The DOQQ digital aerial imagery was collected by the National Agriculture Imagery Program during the 2018 agricultural growing season and through the winter and spring of 2019. They were downloaded from the Texas Natural Resources Information Systems on August 30, 2019.....	90
Figure 47: The vegetation in the study area during the peak growing season (September 2019).....	93
Figure 48: The vegetation defoliation during the winter season (December 2019).....	94
Figure 49: An area where deforestation and mulching has been done.....	95
Figure 50: An area where recent controlled burns were conducted.....	96

LIST OF TABLES

Table 1: A table showing the previous interference type of each filter and the filters buffering parameters.....	17
Table 2: Summary table of karst features identified in traverse surveys 1-3.....	25
Table 3: Summary table of the average geometric properties of each type of karst feature identified in traverse survey 1.....	29
Table 4: Summary table of the average geometric properties of traverse survey 2.....	29
Table 5: Summary table of the average geometric properties of traverse survey 3.....	29
Table 6: Table that contains the filter mechanisms and buffering distances used to remove features during the classification process and the number of features that interfered with each filter. Some features interfered with more than one filter and resulted in the interference count being greater than the total number of features in the database.....	68
Table 7: Confusion matrix with the features that were surveyed to assess the accuracy of the previous filters and buffering parameters.....	84
Table 8: Confusion matrix with the features that were surveyed to assess the accuracy of the new filters and buffering parameters.....	89
Table 9: Summary table of the Geometric properties for each karst feature found in traverse survey 1.....	108
Table 10: Summary table of the geometric properties for each karst feature found in traverse 2.....	110
Table 11: Summary table of the geometric properties for each karst feature found in traverse 3.....	111

LIST OF EQUATIONS

Equation 1: $S = \sqrt{\frac{A}{n}}$ equation used to calculate the cell size.....	40
---	----

PREFACE

The Fort Hood Military Installation is a karst landscape that covers an area of 880 km². Most of the previous studies conducted to characterize and document karst features have been focused on the eastern side of the installation, associated with endangered species habitat and wildlife management areas. Traditional field surveys are often expensive and time consuming, but more importantly the rough terrain and dense vegetation across the installation can make it challenging to traverse these areas on foot. Many of the documented karst features became areas of interest when military personnel or other individuals would discover a new cave or sinkhole and report it to the Natural Resource Management Branch. Previous surveys were conducted in areas of interest and all karst features were entered into an existing database. Even though the surveys were thorough, they were most often conducted in high traffic areas being used by the military for training exercises, resulting in uneven coverage. Remote sensing has become a more prominent tool in geologic studies, with an increased ability to characterize large-scale areas with reasonable accuracy. LiDAR surveys specifically, are used by geologists and spatial scientists to study remote or inaccessible areas without having to be physically present.

The following research was done to aid the Natural Resources Management Branch of Fort Hood in expanding the existing karst database and design a karst potential model that can be used in future karst characterization studies. This study focused primarily on karst characterization in western Fort Hood, specifically the Royalty Ridge and Shell Mountain provinces; both provinces have been heavily altered by military training activities.

The following manuscript utilizes a karst potential model to investigate the distribution and modes of formation of the karst depressions in western Fort Hood. The main paper will be submitted to peer reviewed journal for publication. Appendix A contains additional data associated with this research.

ABSTRACT

The Fort Hood Military Installation is a karst landscape that has been significantly altered for training exercises that include heavy vehicle maneuvers and simulated combat. Traditional karst surveys are often time-consuming and require extensive field analyses to adequately characterize large areas. Bias is given to areas that are most easily accessible and false negatives are common. Previous studies conducted in the eastern and western portion of the base have understated the abundance and spatial distribution of karst, particularly in the western portion.

This study used field traverses and 0.5-meter Light Detection and Ranging (LiDAR) data to characterize surface karst depressions, create a set of new and refined filters and buffering mechanisms to remove non-karst depressions, and determine the accuracy of the model. LiDAR data was used to create a digital elevation model (DEM), which was used to extract areas with localized depressions at a sub-meter scale. In order to isolate features that were formed through karst processes, data were processed through a series of filters with parameters based on features found during traverse surveys.

Field verifications to assess the accuracy of the LiDAR conducted with previous filters and buffering mechanisms had an overall accuracy of 77.3%,

indicating this model overestimated the number of features in the study area. To assess the accuracy of the new filters and buffering parameters, field verified features from a random point survey and a remote verification survey of features within each of the filters was conducted. The overall accuracy was 84.1%, indicating that the new filters and buffering parameters improved depression characterization and the ability to determine those features that were influenced by natural and anthropogenic processes.

INTRODUCTION

The Fort Hood Military Installation is one of the largest military training bases in the United States, as well as one of the largest in the world. Before the base was established in 1942, the land was mostly undeveloped with small communities, farms and ranches connected by dirt roads, wire lines, and typical rural landmarks (Pugsley, 2001). The base is located in northern part of Bell County and the southern part of Coryell County in north-central Texas and covers an area of approximately 880 km² (Figure 1). It is divided into four main regions for training. The western side of the installation is mainly used for heavy mechanical (tracked and wheeled) maneuver training. In the center of the installation is the Live Fire Impact Range used for artillery drills and contains unexploded ordinance. It is restricted from civilian access and acts as a boundary between the eastern and western portions of the base. The eastern side of the installation and a small area in West Fort Hood are mainly used for exercises that include dismounted and wheeled vehicles and small-scale tracked vehicles.

The eastern side is characterized by exposures of Lower Cretaceous Comanchean Series carbonates of the Trinity and Fredericksburg Groups, with numerous outcrops exposed in the creek beds and along the flanks of smaller

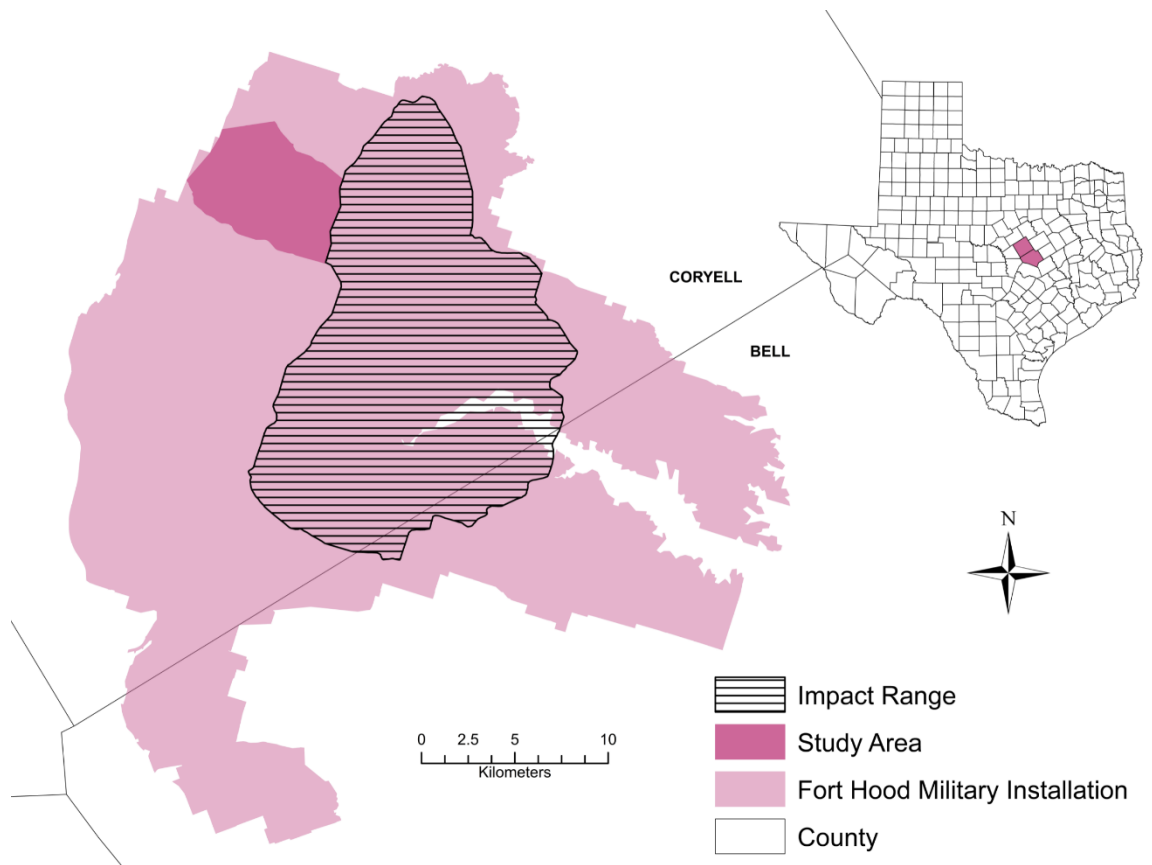


Figure 1: The location and extent of Fort Hood Military Installation. The eastern and western portions of Fort Hood are separated by the impact range. The study area is located in western Fort Hood.

plateaus (Wermund, 1996; Adkins and Arick, 1930). This area hosts significant karst features that are environmentally and structurally sensitive to surrounding activity and are often homes for endangered species. The features found are primarily sinkholes, pits, and caves that are typically less than a few meters in depth or diameter, as well as springs and rock shelters (Hammer, 2011).

Although it is important to consider the safety of the military personnel and the equipment since the installation is a karst landscape used for a wide range of different training exercises, it is especially important to preserve the land and protect the environmentally sensitive species habitats from human disturbances within the installation. The study area extends across the Shell Mountain and Royalty Ridge provinces in western Fort Hood, covering approximately 40 km² (Figure 2). It is bounded by the western border of the installation and the central “live-fire” range and has been significantly altered and developed for training exercises that include heavy vehicle maneuvers and simulated combat.

Sinkhole characterization is crucial for understanding hydrological processes and mitigating geologic hazards in karst landscapes such as Fort Hood (Wu et al., 2016). Sinkholes are closed surficial depressions that form due to subsurface dissolution of soluble underlying materials. They are classified into three different types: dissolution, subsidence, and collapse. Previous karst studies at Fort Hood were conducted using selective ground surveys and subsequent site verification, which often understated the abundance and spatial

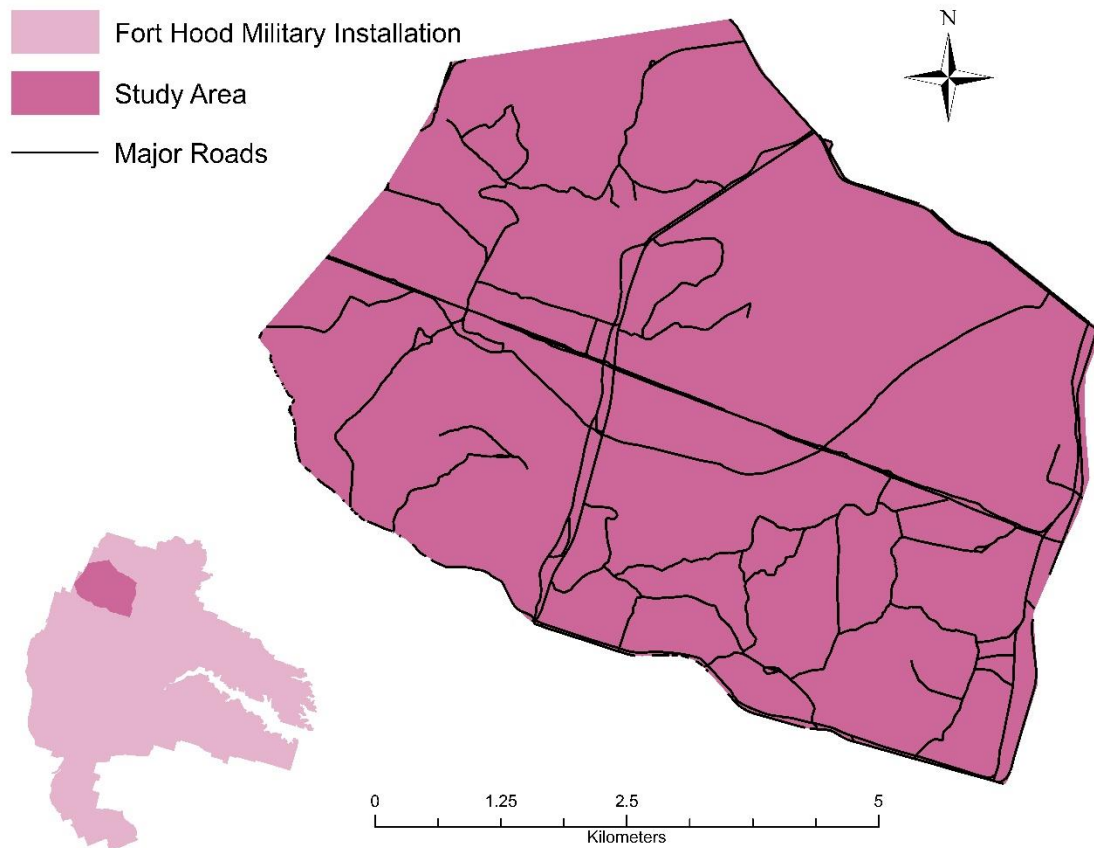


Figure 2: The location and extent of the study area within the western portion of Fort Hood Military Installation. There are major roads that have been built in order for military personnel and equipment to travel through the training areas.

distribution of karst features. These surveys were often biased and targeted areas near established roads with significantly large features. Transect surveys have also been conducted, but dense vegetation and the extensive surface area made surveying labor intensive and time consuming (Reddell et al., 2011).

In recent studies, Light Detection and Ranging (LiDAR) has been used to conduct terrain analyses, providing an alternative for high-density and high-accuracy three-dimensional terrain point data collection (Liu, 2008). This modern surveying method can detect surface depressions with greater accuracy and less bias than traditional surveying methods. The purpose of this study is to characterize surface karst depressions through field traverses to refine the filters and buffering mechanisms and assess the relative accuracy of LiDAR. The resulting karst features found during the study will be added to the Natural Resources Management Branch karst database at Fort Hood.

LITERATURE REVIEW

Regional Setting

Fort Hood Military Installation lies within the Lampasas Cut Plain physiographic region, located at the northwestern edge of the Edwards Plateau (Figure 3). The Lampasas Cut Plain is characterized as a transition zone between the Edwards Plateau and the North-Central Plains, spanning over 18,000 km². The topography is gently sloping with higher elevations occurring on the mesa ridges in the northwest while lower elevations occur on the rolling uplands and canyons associated with stream valleys and drainages in the southeast.

The Lampasas Cut Plain region is dominated by Cretaceous carbonates from the Trinity, Fredericksburg, and Washita Groups (Amsbury et al., 1984). The eastern section of Fort Hood is a range of steep plateaus and valleys where karst features such as shelter caves, pits, and sinkholes appear. The relief is typically high, with steep escarpments separated by sweeping, flat lowlands (Bryant, 2012). The topography in western Fort Hood is broad with extensive plateaus. This area is less susceptible to karst development because of underlying lithology, hydrologic processes, and lower relief (Faulkner, 2016). Exposed surficial outcrops in the study area are primarily Lower Cretaceous Trinity and

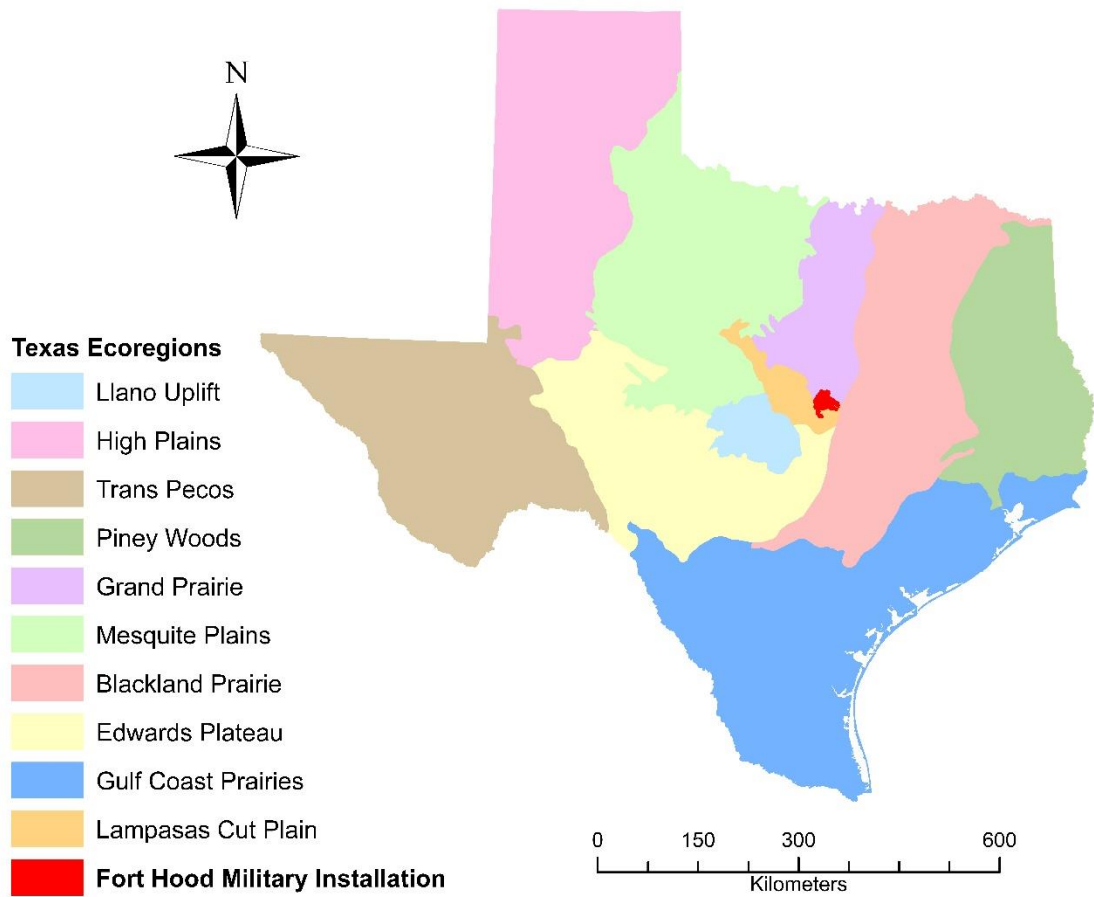


Figure 3: Physiographic map of Texas showing the ecoregions and location of Fort Hood Military Installation.

Fredericksburg Group carbonates. These units were deposited approximately 110 mya along the Central Texas Reef Trend across the Comanche Shelf. The Trinity Group, including the Glen Rose Formation, outcrops only where overlying strata has been eroded by incision in stream valleys and other topographic lows. The Fredericksburg Group is found in areas of higher elevations on escarpment faces and hilltops where erosion is less extensive (Faulkner, 2016; Nelson, 1973).

The most important karst-forming units in this study are the Edwards and Comanche Peak formations (Figure 4). Most of the karst in the area is found in outcrops of these units and at their contact boundaries, which form permeability transitions that promote dissolution (Reece, 2018). The Comanche Peak Formation is a chalky, nodular limestone with a marl or clay-like matrix (Adkins & Arick, 1930). Its thickness ranges between 12 m to 21 m, with the maximum thickness in Coryell County (Collins, 2005). The Comanche Peak and Edwards formations often exhibit complex interfingering at their boundary (Rose, 1972). The Edwards Formation is a series of medium to massive, thick-bedded limestones, dolostones, and marls. It is specifically described as carbonate grainstones, wackestones, and mudstones, including rudist bioherms and biostromes that are typically light in color (Fisher & Rodda, 1969). The most characteristic features of the Edwards Formation are its erosional features: it is often heavily karsted, exhibits abundant karren of different forms and sizes, and

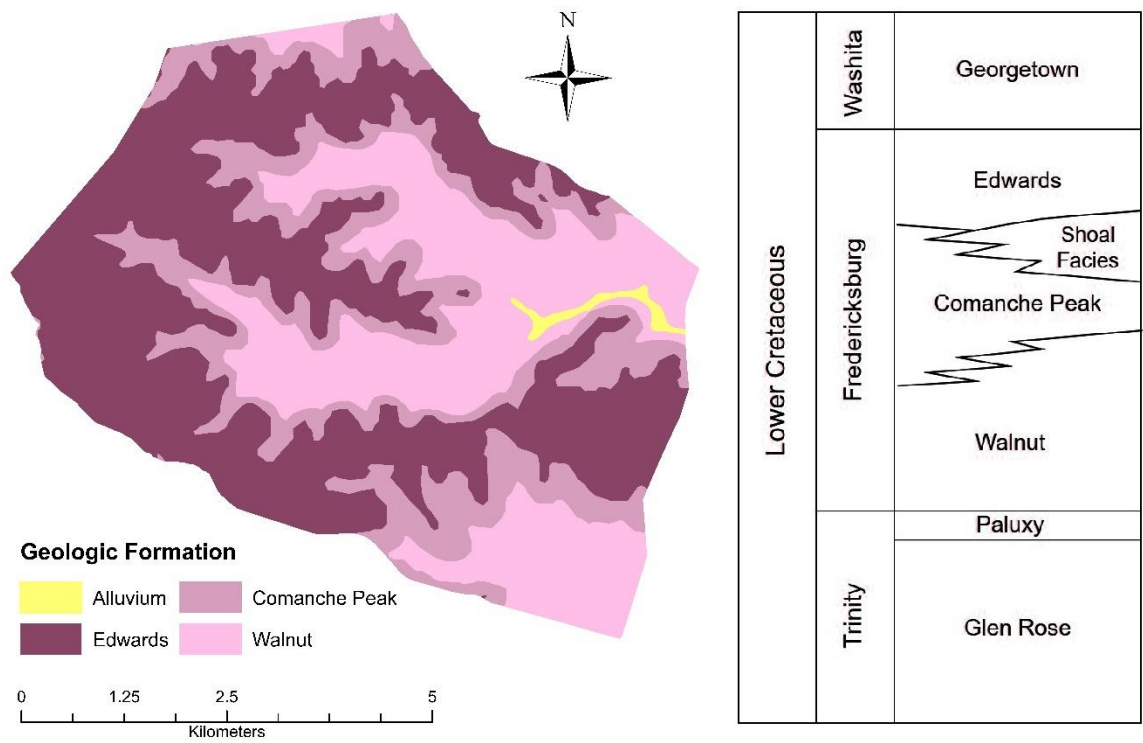


Figure 4: Geologic map and stratigraphic column (from Faulkner, 2016) showing the units present in the study area.

hosts sinks, collapse breccias, and highly transmissive zones (Jones, 2003). The thickness of the Edwards Formation tends to range from approximately 25 m to 90 m, thinning southward in Bell County (Adkins & Arick, 1930).

Karst Development

Karst typically forms in three different settings: eogenetic, hypogenic, and epigenic. Eogenetic is the coastal and oceanic karst that occurs in geologically young rocks with high matrix porosity and permeability (Klimchouk, 2009). Caves form where there is mixing of fresh and saline waters with other fluids from meteoric and marine sources. Hypogenic karst forms in semi-confined to confined soluble rocks, and enters a formation from below the surface. Epigenic karst forms in unconfined conditions where geologically mature rock at or near the surface are exposed to meteoric water that has been recharged from the earth's surface (Klimchouk, 2009). The order in which these are described correlate directly to their sequence of karst evolution (Klimchouk, 2009). Since the study of karst began, epigenic karst systems are the most widely studied and well understood systems. Recently hypogenic karst systems are becoming an area of interest in speleogenetic research, but is still not well understood (Klimchouk, 2007). The Edwards Plateau and Lampasas Cut Plain are major karst areas that consist of carbonate rocks exposed at the surface from uplifting that occurred since Cretaceous time, allowing the development of secondary porosity. Many of the caves at Fort Hood host features that can be characterized

by epigenic and hypogenic processes (Elliot and Veni, 1994). Sinkholes are subsidence and collapse sinkholes. Dissolution (solutional) sinkholes have particularly prominent at Fort Hood; the three major types found this region are dissolution (solutional), little to no overlying sediment. They tend to form as fractures are widened by water at the surface and are prominent in the eastern portion of Fort Hood (Bryant, 2012; Faulkner, 2016). Subsidence sinks form where loosely consolidated material (i.e. soil) is piped into voids and fractures in the underlying bedrock; here, suffosion processes dominate, leaving bowl-like depressions as sediment is washed into the subsurface. Finally, collapse sinks are expressed where the structural integrity of the bedrock is compromised by the dissolution beneath a point in the subsurface. Collapse sinks typically intersect existing conduits and may provide cave access as well. They account for the majority of mapped features at Fort Hood; however, this is likely due to the bias given to caves over minor sinkholes (Reddell et al., 2011).

In the study area, karst is most prevalent on the escarpments and plateaus. Numerous features found in earlier studies by the Texas Speleological Society (TSS) and the Fort Hood Natural Resources Management Branch were mapped as they were discovered during military operations and road construction. The karst development in the area is mainly controlled by the lithology, specifically where the Edwards Group is exposed in areas of higher elevation. Karst features tend to form in clusters or roughly localized groups, due

to the geomorphology of the plateaus (Reece, 2018). Previous studies described a division between sinkholes related to the solutional widening of fractures and those that could be tied to the collapse of bedrock or suffusion processes (Faulkner et al., 2013; Reddell et al., 2011). Across the installation, 335 caves, 235 springs, 943 sinks, and 739 shelter caves have been discovered (Figure 5). Many of the known features are concentrated on the east side of the installation in the Owl Mountain and Nolan Creek provinces where the majority of previous studies have been conducted. Other areas, including western Fort Hood and the Impact Range, have not been adequately described due to lack of extensive research and restricted access.

Previous Karst Studies

Karst studies have been conducted in Fort Hood for many years, mostly focusing on the eastern side (Figure 6). This research is a continuation of previous studies that have been conducted in attempt to characterize karst features within Fort Hood Military Installation. The studies in the eastern portion of the base used 1-meter resolution LiDAR data collected in 2009 by Quantum Spatial for the Fort Hood Military Installation (Faulkner et al., 2013; Bryant, 2012). These studies used filters and buffering parameters to remove karst features influenced by infrastructure, water bodies, and anthropogenic processes (Table 1). The initial study in the western portion used 0.5-meter resolution LiDAR data with the same filters and buffering parameters (Reece, 2018), which resulted in

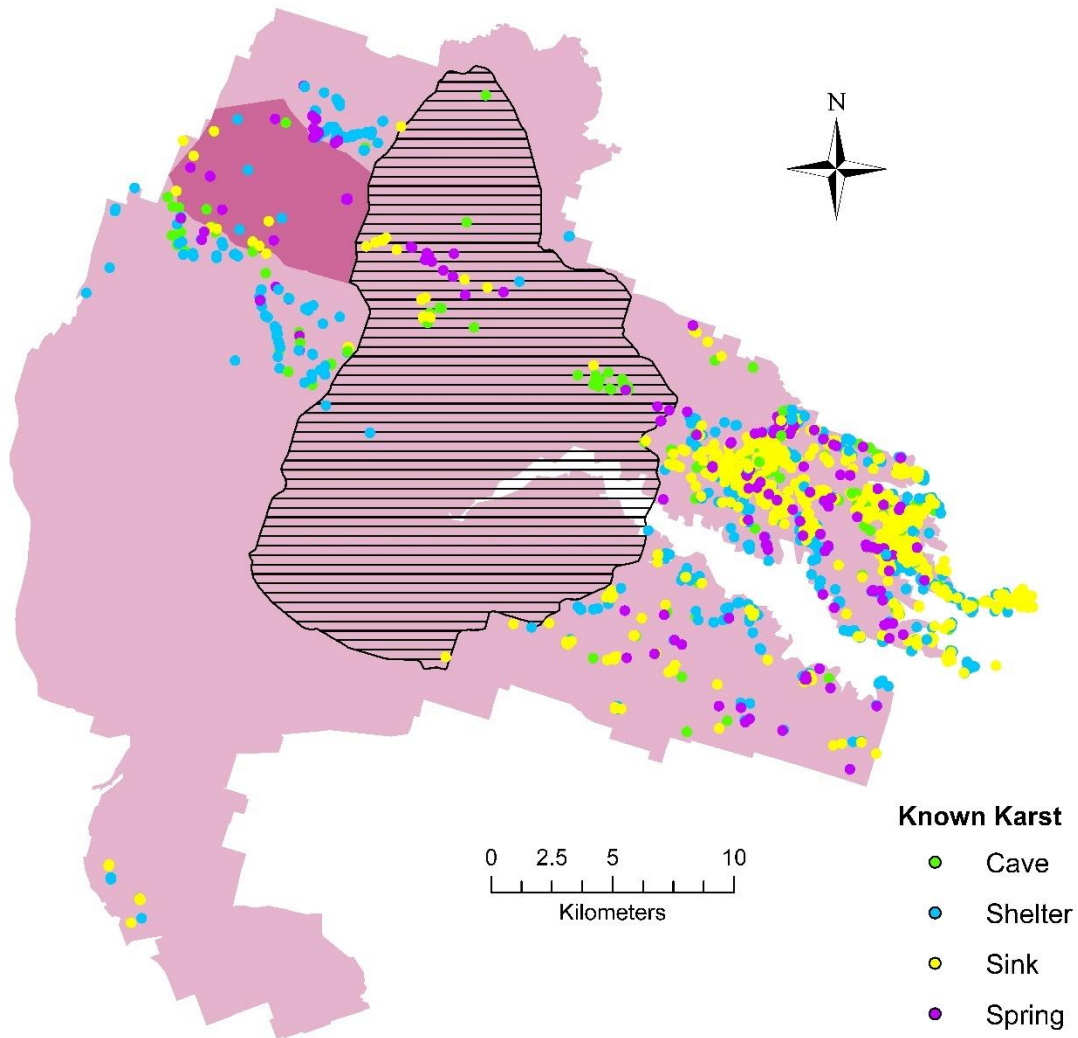


Figure 5: Spatial distribution of known karst features identified in Fort Hood.

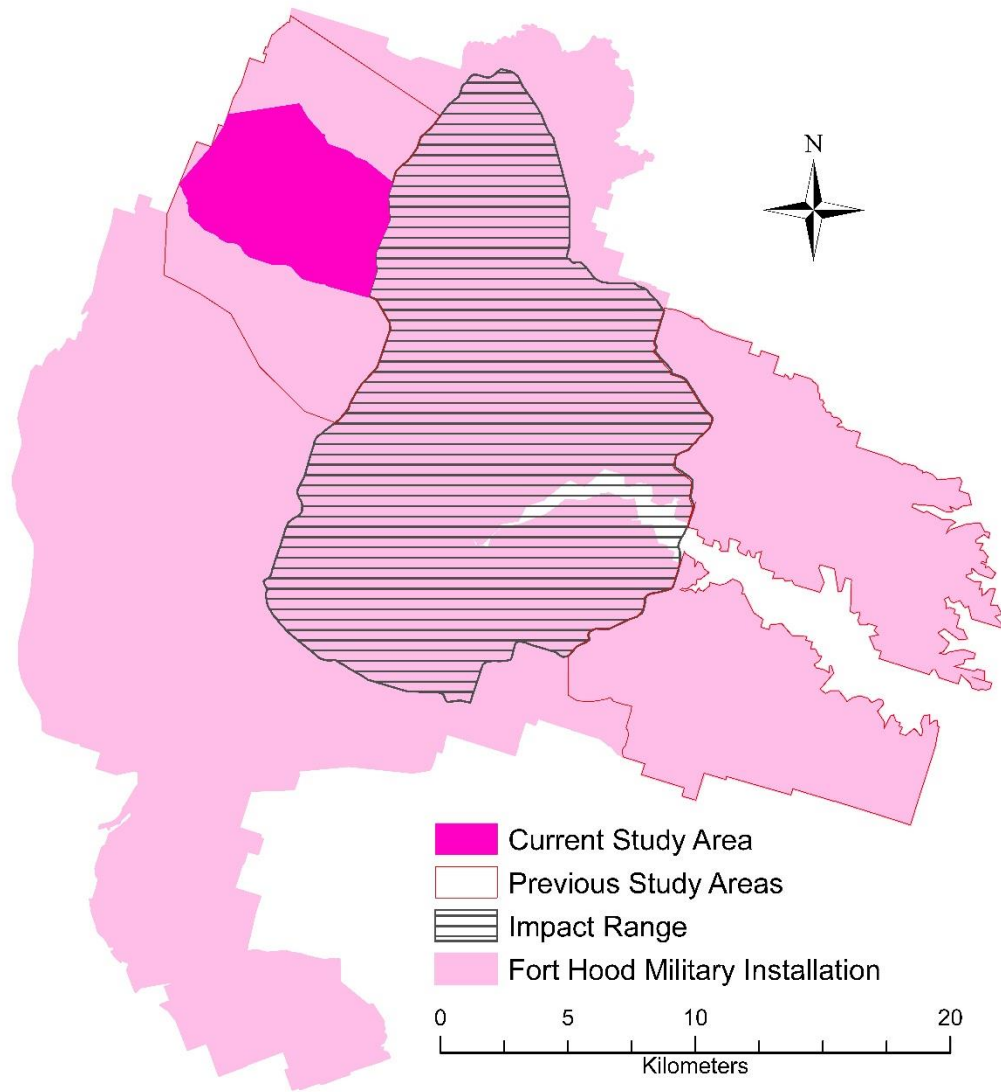


Figure 6: Map showing the previous areas where karst studies have been conducted within Fort Hood Military Installation.

Table 1: A table with the previous interference types and the filter buffering parameters.

Interference Type	Filter
Lithology	Geology Shapefile
Major Roads	15
Minor Roads	10
Streams	5
Water Bodies	20
Land Cover	Land Cover Shapefile

features that should have remained in the database. To more accurately assess features possibly being misidentified by incorrect filtering or removing true karst in western Fort Hood, points that were identified during traverse surveys were used to modify existing filters and create new filters and buffering parameters to make them more applicable to the higher resolution data set used in this current study.

METHODOLOGY

Field Traverses

Field traverses were conducted to delineate and classify karst features along three north-south survey sections in the study area, without bias associated with previously documented features. Karst features identified in these surveys were used to create and refine filters and buffering parameters to remove features that were influenced by infrastructure, water bodies, and anthropogenic activities. To ensure that the study area was adequately surveyed, survey sections were established running through the eastern, middle, and western portions of the study area. Each survey section contained 11 traverse lines in 10 m intervals and covered an east-west 100 m distance (Figure 7). The close spacing of traverse lines was necessary to be sure that all noticeable karst features in the survey would be located across the densely vegetated plateaus. A Garmin Rino 650 handheld GPS was used to accurately follow the traverse lines and document the location of karst features within the survey sections. Any karst feature within the survey section was recorded, described, and the geometric properties were measured. A total of 157 karst features including sinkholes, shelter caves, and solutional conduits augmented by root structures were recorded during the field traverses. These features were typically located on the

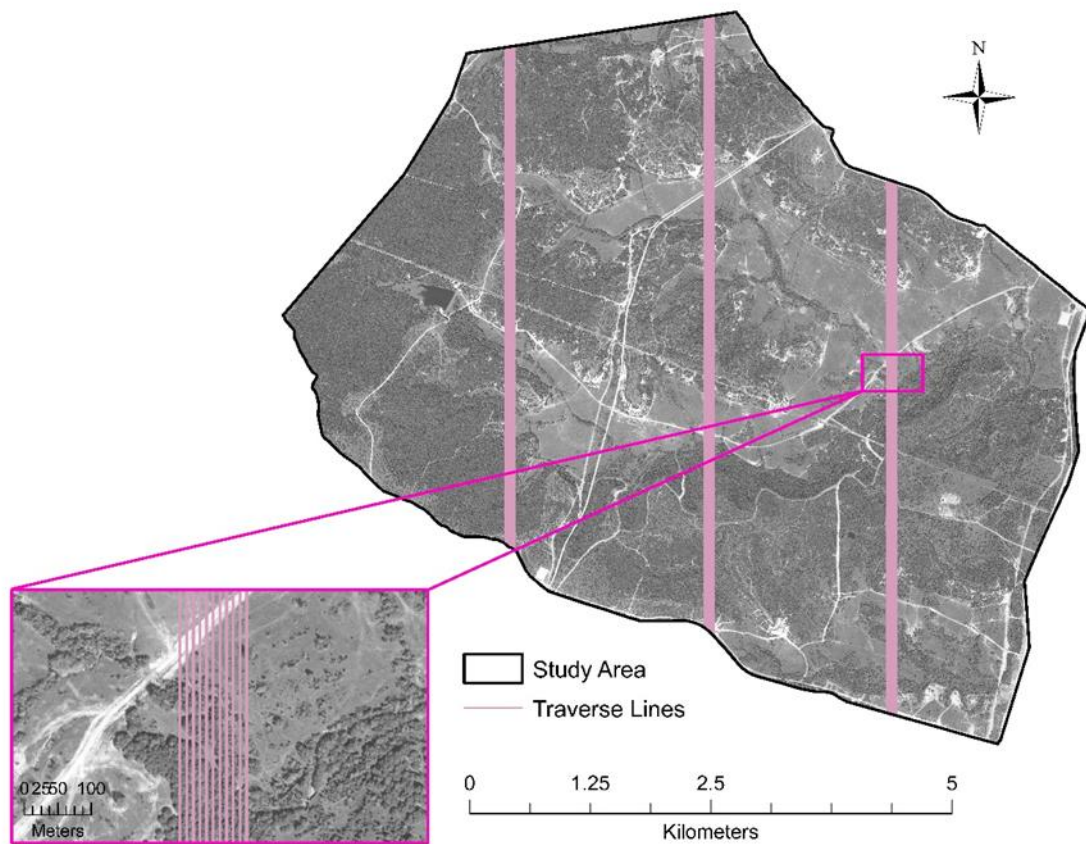


Figure 7: Location and extent of the three north-south traverse-based survey sections running through the eastern, middle, and western portions of the study area. The enlarged region shows the 10 m spacing spatial distribution of the traverse lines in the traverse-based survey. The DOQQ digital aerial imagery was collected by the National Agriculture Imagery Program during the 2018 agricultural growing season and through the winter and spring of 2019. They were downloaded from the Texas Natural Resources Information Systems on August 30, 2019.

ridges and plateaus, topographically high areas capped by the Edwards Formation and along the hydrogeologic boundary between the Edwards and Comanche Peak formations (Figure 8). Many of the sinkholes that were collapsed features were circular, with diameters no greater than 65 cm and depths no more than 30 cm (Figure 9) and contained an opening that was typically infilled with rock debris. The sinkholes that were shallow bowl like depressions discovered during the field surveys were circular or slightly ellipsoidal in shape with depths that rarely exceeded 30 cm (Figure 10). Table 2 shows the number of each feature located in each set of traverses. Shelter caves spanned along the edges of the plateaus (Figure 11), but these features would not be detected during LiDAR analyses. The most common features were small openings near root structures and shallow bowl like depressions with no opening that could potentially result in the formation of a collapsed sinkhole. The small openings near the root structures were commonly circular with a diameter no more than 45-65 cm and depths that could be measured no greater than 80 cm (Figure 12). These small openings were thought to be animal burrows, however as they became more prominent during field surveys, they were then reclassified as pathways for soil piping and fluvial transport. These openings can provide a pathway for water to infiltrate into the ground and eventually enable karst development in the sub surface and surficial carbonates and enhance dissolution associated with subsurface karst features.

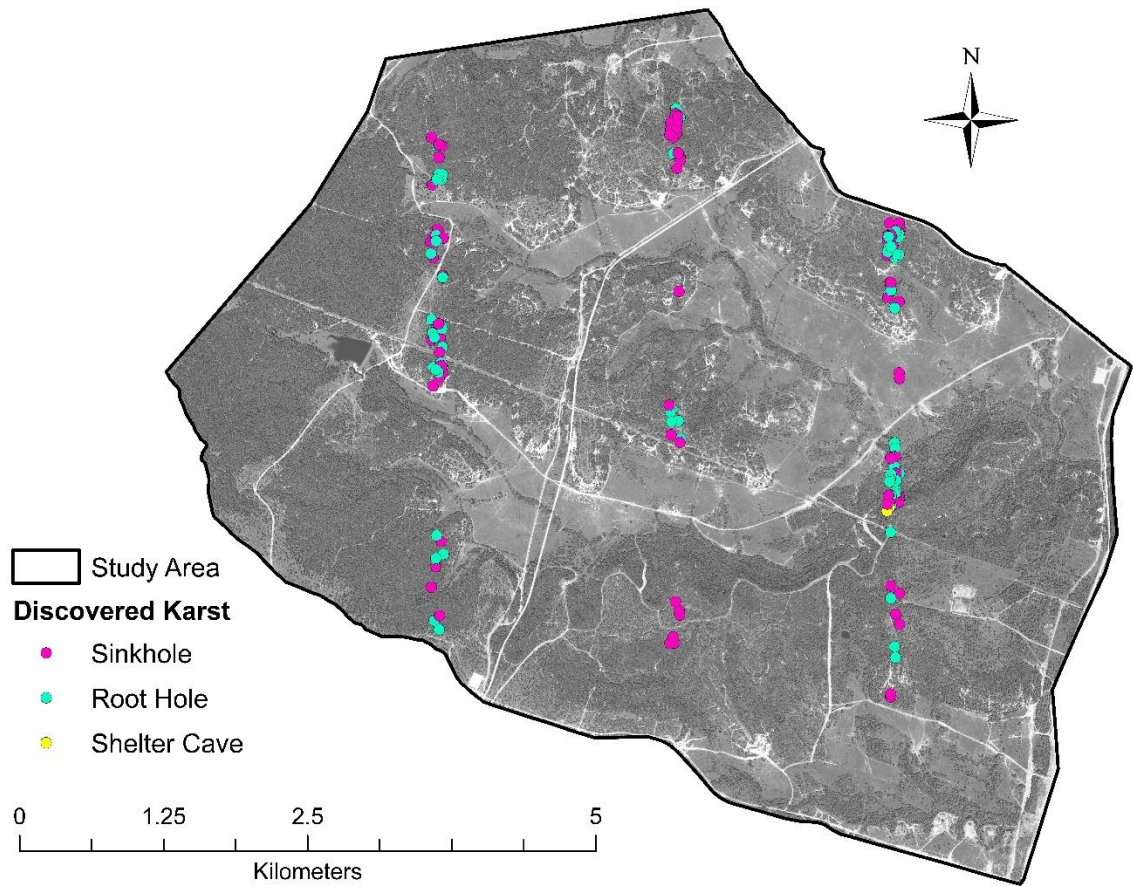


Figure 8: The karst features identified during the traverse-based survey. Many of the features are found in high elevated regions. The DOQQ digital aerial imagery was collected by the National Agriculture Imagery Program during the 2018 agricultural growing season and through the winter and spring of 2019. They were downloaded from the Texas Natural Resources Information Systems on August 30, 2019.

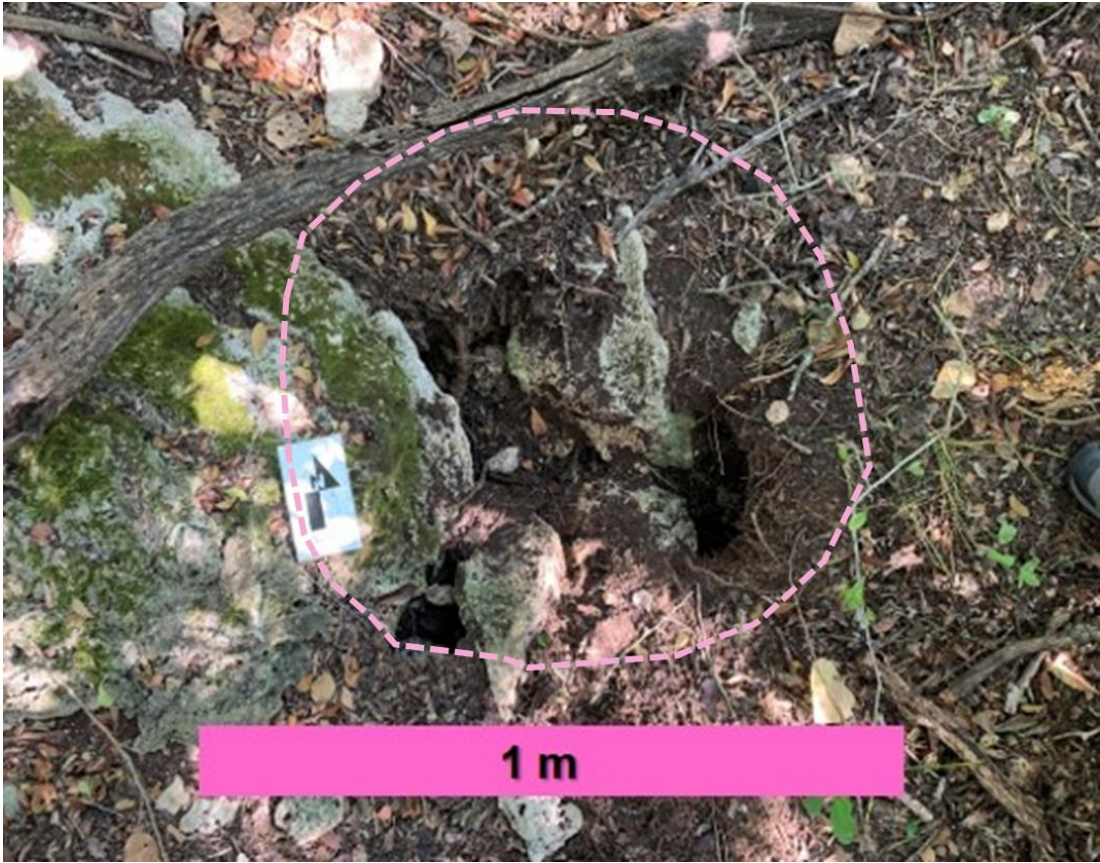


Figure 9: An example of a collapsed feature found during the traverse-based survey.

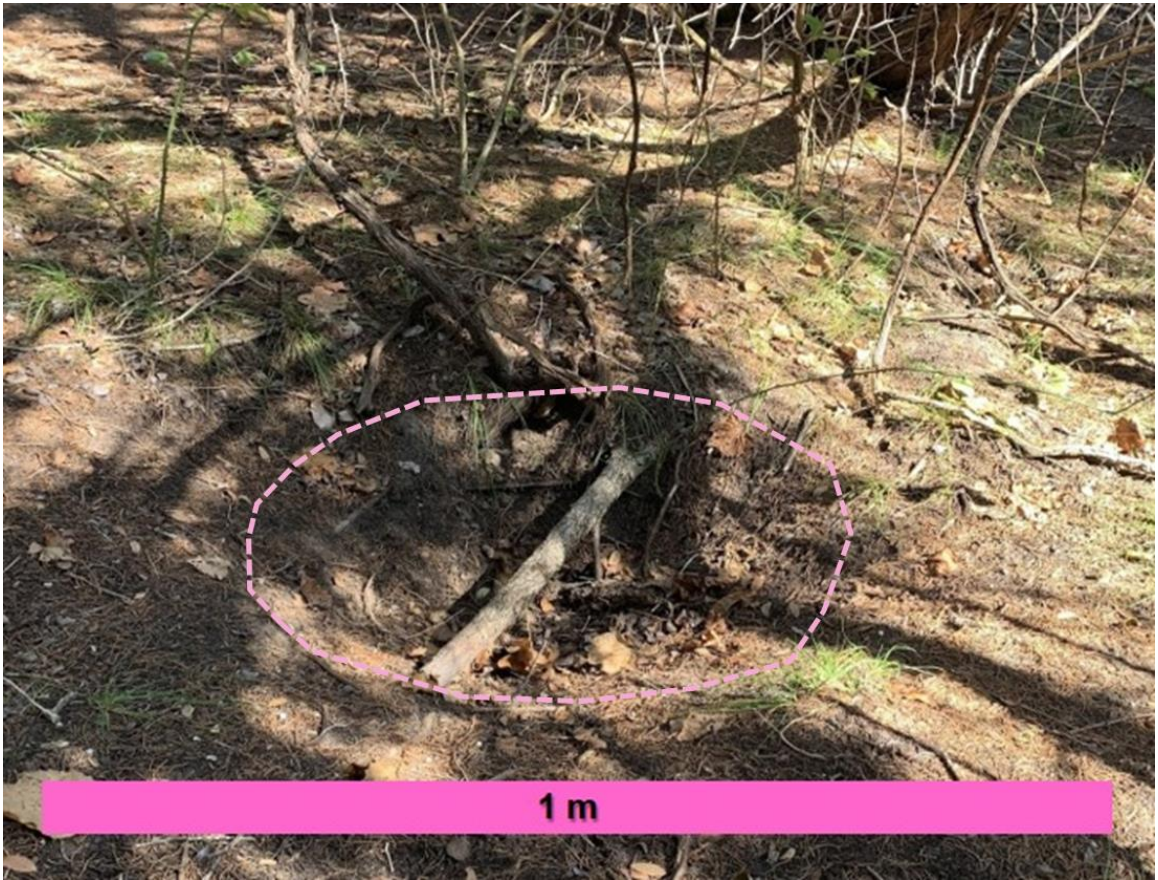


Figure 10: An example of a bowl like depression resulting from the subsidence of the ground.

Table 2: Summary table of karst features identified in traverse surveys 1-3.

Traverse Number	Sinkhole	Root Hole	Shelter Cave
1	35	30	3
2	27	6	-
3	25	31	-
Total	86	66	3
		Sum Total	157



Figure 11: An example of a shelter cave found during the traverse-based survey.



Figure 12: An example of a root hole (solutional conduit) found during the traverse-based survey.

The first section of traverses was located on the eastern side of the study area. A total of 68 features were identified and included three shelter caves, 35 sinkholes, and 30 root hole openings. In traverse 1, seven of the features identified interfered with filtering mechanisms. The features that interfered were categorized as either a root hole or a depression and interfered with the minor roads, land cover filter, or both. These features did not meet size and depth criteria to be accurately resolved by the LiDAR survey. In an area on the side of a ridge there was a cluster of 15 features identified and all features but one would not meet the size and depth criteria to be accurately resolved. Table 3 shows the average geometric properties and classification of each kind of karst feature identified in traverse 1.

The second section of traverses were located in the middle part of the study area. A total of 33 features were identified and included 27 sinkholes and 6 root holes. In traverse two, ten of the features identified interfered with filtering mechanisms. These features that interfered were categorized as sinkholes and interfered with minor roads, land cover filter, or both. These features did not meet size and depth criteria to be resolved by the LiDAR survey. Many of the sinkholes were found in areas of higher elevation. Table 4 shows the average geometric properties and classification of each kind of karst feature identified in traverse 2.

The third section of traverses were located on the western side of the study area. A total of 56 features were identified and included 25 sinkholes and

Table 3: Summary table of the average geometric properties of each type of karst feature identified in traverse survey 1.

Classification	Length (m)	Width (m)	Depth (m)	Circularity
Sinkhole	0.5053	0.4579	0.2791	1.1
Root Hole	0.3384	0.2261	0.5117	1.5
Shelter Cave	4.3180	0.7281	1.6425	5.7

Table 4: Summary table of the average geometric properties of each type of karst feature identified in traverse survey 2.

Classification	Length (m)	Width (m)	Depth (m)	Circularity
Sinkhole	1.0104	0.9238	0.2206	1.1
Root Hole	0.3260	0.2117	0.3514	2.1
Shelter Cave	-	-	-	-

Table 5: Summary table of the average geometric properties of each type of karst feature identified in traverse survey 3.

Classification	Length (m)	Width (m)	Depth (m)	Circularity
Sinkhole	0.9672	0.6970	0.3104	1.5
Root Hole	0.3908	0.3015	0.3220	1.5
Shelter Cave	-	-	-	-

31 root hole openings. In traverse three, five of the features identified interfered with filtering mechanisms. The features that interfered were categorized as sinkholes and interfered with minor roads, land cover, or the geology filter. These features did not meet size and depth criteria to be resolved by the LiDAR survey. Table 5 shows the average geometric properties and classification of each kind of karst feature identified in traverse 3.

Geographic Information Systems

In the past few decades, the increasing capabilities of GIS (Geographic Information Systems) and accuracy of geographically referenced data has made it possible to conduct more detailed terrain analyses and modeling (Liu, 2008). With the use of spatial interpolation and physical field checks, karst features can be delineated and characterized with greater accuracy and efficiency across larger areas. Previous methods for identifying karst features required intense labor and long periods of time in the field to manually survey the area on foot. This typically resulted in underestimating the number of potential sinkholes in an area (Wu et al., 2016).

Recent studies have implemented the use of LiDAR to delineate and analyze small-scale geomorphologic features, specifically sinkholes (Wu et al., 2016). This method provides an alternative for high-density and high-accuracy three-dimensional terrain point data collection (Liu, 2008). The data can then be used to create a digital elevation model (DEM) that represents the terrain of the

study area in great detail. With the use of GIS and geoanalytical methods, depressions can be classified and characterized more efficiently and accurately. Typically, the “fill difference” method is used to detect sinkholes. With this process, the sinkholes are filled and then the original DEM is subtracted from the filled DEM. The resulting raster contains all the possible depressions in the study area, including both karst and anthropogenically formed depressions. To ensure that only karst related depressions are included in the survey, extensive buffering and filtering mechanisms must be applied.

Light Detection and Ranging

LiDAR stands for Light Detection and Ranging, an active remote sensing technology that provides three-dimensional terrain point cloud data of a surveyed area. This type of surveying has become more useful than traditional photogrammetric methods for collecting elevation data for multiple reasons: it includes a high degree of vertical accuracy, the data collection and processing time is minimal, the high-density data sets can be used to create a variety of models, and surveys can be conducted in a wide range of conditions.

There are different types of LiDAR data and for this study, airborne LiDAR was used to survey the Fort Hood Military Installation. These airborne systems are made of three main components: a laser scanner unit, a Global Positioning System (GPS) receiver, and an Inertial Measurement Unit (IMU) (Lui, 2008). These systems are attached to a helicopter or the wing of an airplane and flown

over the area of interest (Fugro, 2011). The scanner unit emits laser pulses and then receives the scattered and reflected light from the surface (Figure 13). The precise times of each pulse as it is emitted and reflected is recorded and can then be used to find the line-of-sight distance (range) by multiplying the time difference between the emission and the reflection by the speed of light (Lui, 2008). Using Global Positioning System (GPS) and Inertial Measurement Units (IMU), the LiDAR data is transformed into measurements of land surface elevation relative to the Earth ellipsoid, or better known as XYZ coordinates (Tibouo, 2016). The collection parameters established for a LiDAR survey re based on project specifications and consist of point spacing and density, pulse rate, field of view, and the altitude and speed of the aircraft (Fugro, 2011). LiDAR systems are able to record multiple laser returns for each emitted pulse however, there are not always multiple returns for each emitted pulse. For example, if the area is open terrain, there will only be one return. The majority of systems usually detect up to four returns, some can record up to six returns or more for a single emitted pulse (Lui, 2008). For systems that record four returns: the first return measures tree canopy, the second return measures lower branches and vegetation, and the third or fourth return measure bare earth or the ground (Fugro, 2011).

In March of 2015, the U.S. Army Corps of Engineers (USACE) contracted Photo Science, a Quantum Spatial Company to conduct airborne LiDAR surveys.

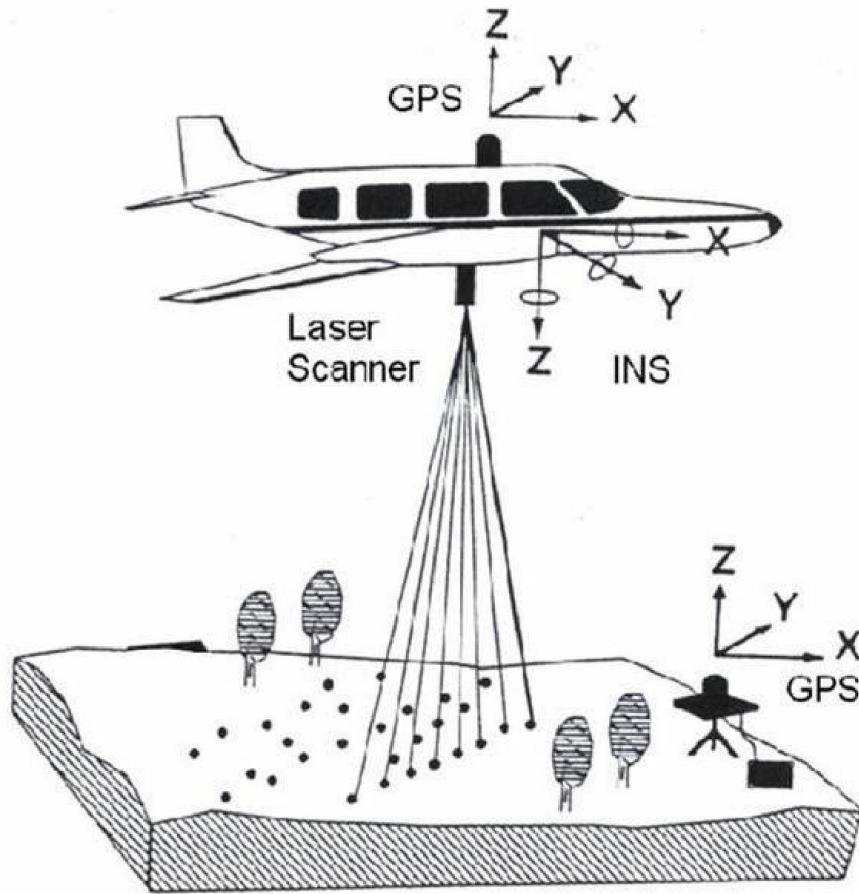


Figure 13: Diagram showing the data collection process for airborne surveys (Kao et. al., 2005).

The survey began on March 14th, 2015 and was successfully completed by March 17th, 2015. The positional accuracy of the raw LiDAR data was tested using ground control points in five distinct areas (Figure 14). The data was collected over 48 flight lines with 70 control points that covered an area of 880 km² over Fort Hood Military Installation. The raw data collected from the LiDAR survey was processed using the software package DASHMap produced by Optech, Inc. DASHMap generated a set of data points for each laser return in an LAS file by using the GPS, INS (Internal Navigation System), pitch, roll and heading information from the plane's onboard POS (Positioning Orientation System) (Quantum Spatial, 2015). The Root Mean Square Error (RMSE_(z)) of 0.039 m came from statistics that were calculated based on known ground control points and their respective laser returns. In a LiDAR survey, the vertical accuracy should be 1.96 times greater than the RMSE_(z), giving 95% confidence in a vertical accuracy of 0.077 m over the entire surveyed area (Flood, 2004). The ALS70 sensor used in this survey has a horizontal accuracy of 1.0 foot at 4,300 feet flight altitude. The altitude flown was 7,850 feet meaning the horizontal accuracy for the survey is 1.82 feet (0.55 meters) (Quantum Spatial, 2015). Quantum Spatial created classified LAS files that were then acquired by the Natural Resources Management Branch at Fort Hood Military Installation. Each point had up to 8 laser returns, however most of them had less than 4 returns. The last returns for each point designated as "ground" were converted to

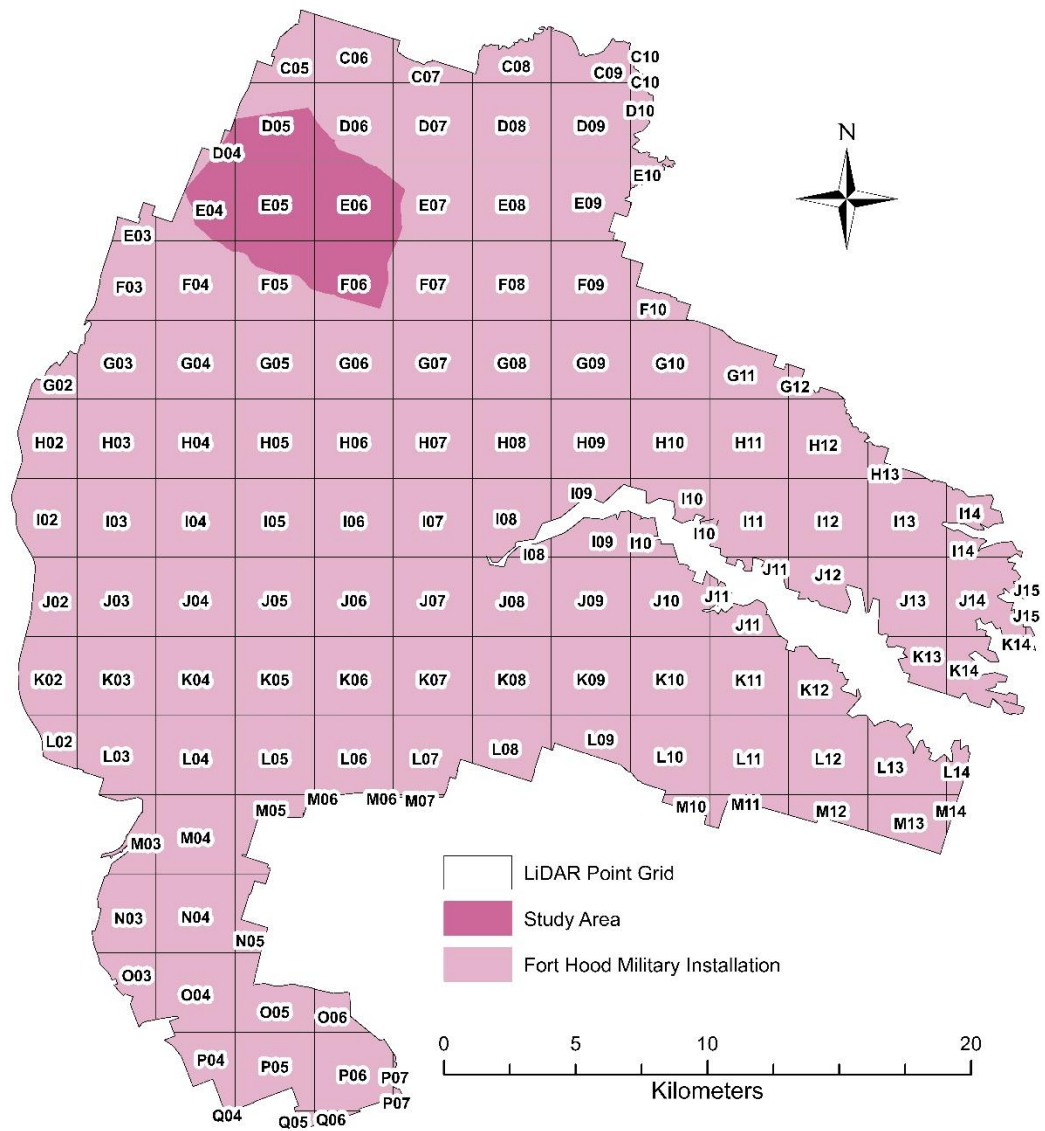


Figure 14: LiDAR grid tiles for all of Fort Hood Military Installation from the LiDAR survey acquired from the Natural Resources Management Branch.

multipoint format and stored in a geodatabase to be used in ESRI's ArcGIS Desktop 10.6 (Reece, 2018).

LAS Dataset and DEM

The high density and accuracy of airborne LiDAR surveys makes it possible to build geostatistical models with collected elevation points that can be used for terrain analysis. The raw point cloud data was imported into ESRI ArcGIS to build a digital elevation model to delineate and characterize karst features in the training areas at Fort Hood. To begin the process of creating a DEM, a LAS dataset was built to extract the data from the LiDAR point cloud LAS file. The study area consisted of nine LAS files, the digitized breaklines, and the study area shapefile that were used to create the LAS dataset using the *Create LAS Dataset* tool under the *Data Management tools* section (Figure 15). The study area boundary and digitized breaklines were defined as soft clip and hard line type. The boundary and breaklines defined the extent of the model and was used to identify areas that did not contain data so that they were omitted from the model interpolation process (ESRI, 2020). The resulting LAS dataset consisted of all the point cloud data collected during the LiDAR survey for the study area only. A DEM was built to analyze karst depressions and only displayed the ground points that represented the true surface topography of the area. The LAS Dataset Toolbar was used to specify a few options before the DEM was created. There are four dropdown tabs in the toolbar: LAS Dataset, Point Display, Surface

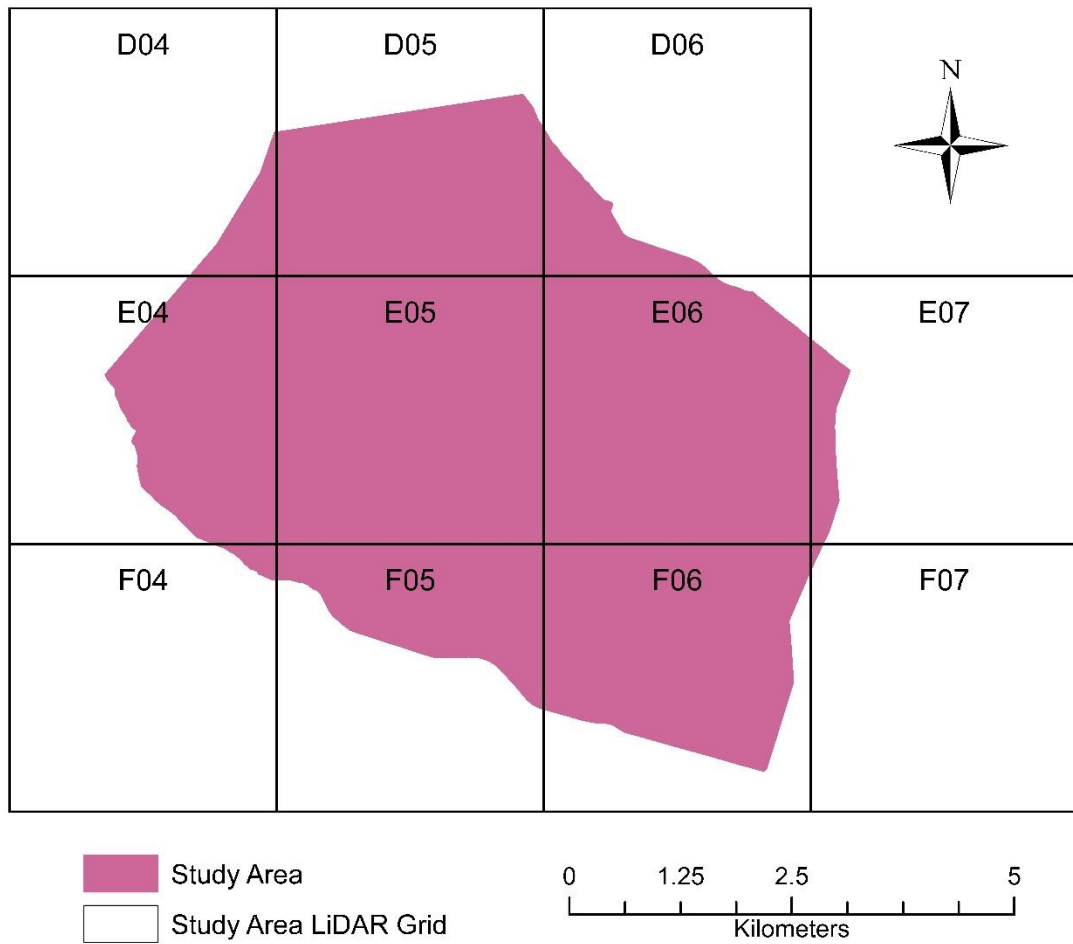


Figure 15: LiDAR grid tiles from the LiDAR survey acquired from the Natural Resources Management Branch that contain the study area.

Display, and Preset Filters.

The first dropdown known as “LAS Dataset” provides the option to look at the pan options and the profile tool options for the current layer. The pan option controls the offset that the panning tools will move when selected (ESRI, 2020). The profile tool option controls the number of points that can be displayed in a single cross section. For this LAS dataset, the point count budget was set to 150,000 to improve the display. The next three dropdowns can be used display the LiDAR point cloud data by criteria selected in the dropdown list (Figure 16). The “Point Symbology Renderers” option can be used to display the LiDAR point data by its elevation, class, or return. The elevation option will display the point cloud based on the elevation. The class option will display the LAS point cloud based on the classes that are within the dataset such as ground, high or low vegetation, water, unassigned etc. The return option displays the LAS point cloud data based on the return such as first, last, all, ground, etc. (ESRI, 2020). The “Surface Symbology Renderers” dropdown can be used to display a surficial view of the LiDAR point cloud data by elevation, aspect, slope, and contours. The elevation option will create a topographic display of real-world elevation data. The aspect option displays a downslope direction for the maximum rate of change (Ehrhart, 2016). The slope option will display the steepest part of each cell and be recorded in degrees. The contour option is similar to the elevation option in this dropdown that will create a real-world topographic map based on

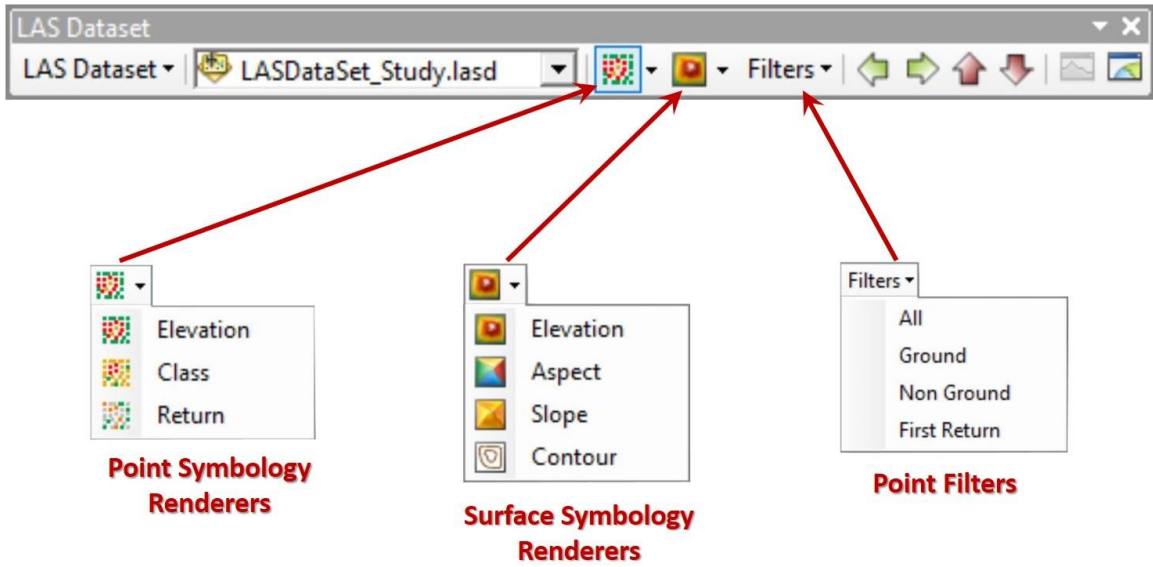


Figure 16: LAS Dataset Toolbar options as seen in ArcMap for Desktop V. 10.6.

the elevations of the area, but just display contour lines. The last “Point Filters” option is the most important one that was used to create the DEM required for further processing, and allows the ability to efficiently filter data. The process of creating a DEM is quick and simple using the *LAS Dataset to Raster tool*. However, it is important to remember that previously selected options will play a role in creating the final DEM when used (Ehrhart, 2016). Using the LAS dataset, ground (bare earth) preset filter, and the triangulation method; the *LAS Dataset to Raster* was used to create the DEM for the study area (Figure 17). The triangulation method derives cell values using a TIN (triangular irregular network) approach and will give a true interpolation of the data. The Natural Neighbor interpolation was used because it produces a smoother more precise model than other methods since it uses the surrounding cells to determine cell values of the DEM (ESRI, 2020). The sampling type was set to cell size, which can be determined by the resolution of the LAS data. If that is not known then the cell size (i.e. resolution) can be calculated by equation 1:

$$S = \sqrt{\frac{A}{n}}$$

Where S is the cell size, n is the total number of elevation points, and A is the area covered by the DEM (Hu, 2003). This means that the cell size should be the same as the point spacing of the original surveyed points (Lui, 2008). The cell size used for this model was set to 0.5 m. The resulting DEM was a high

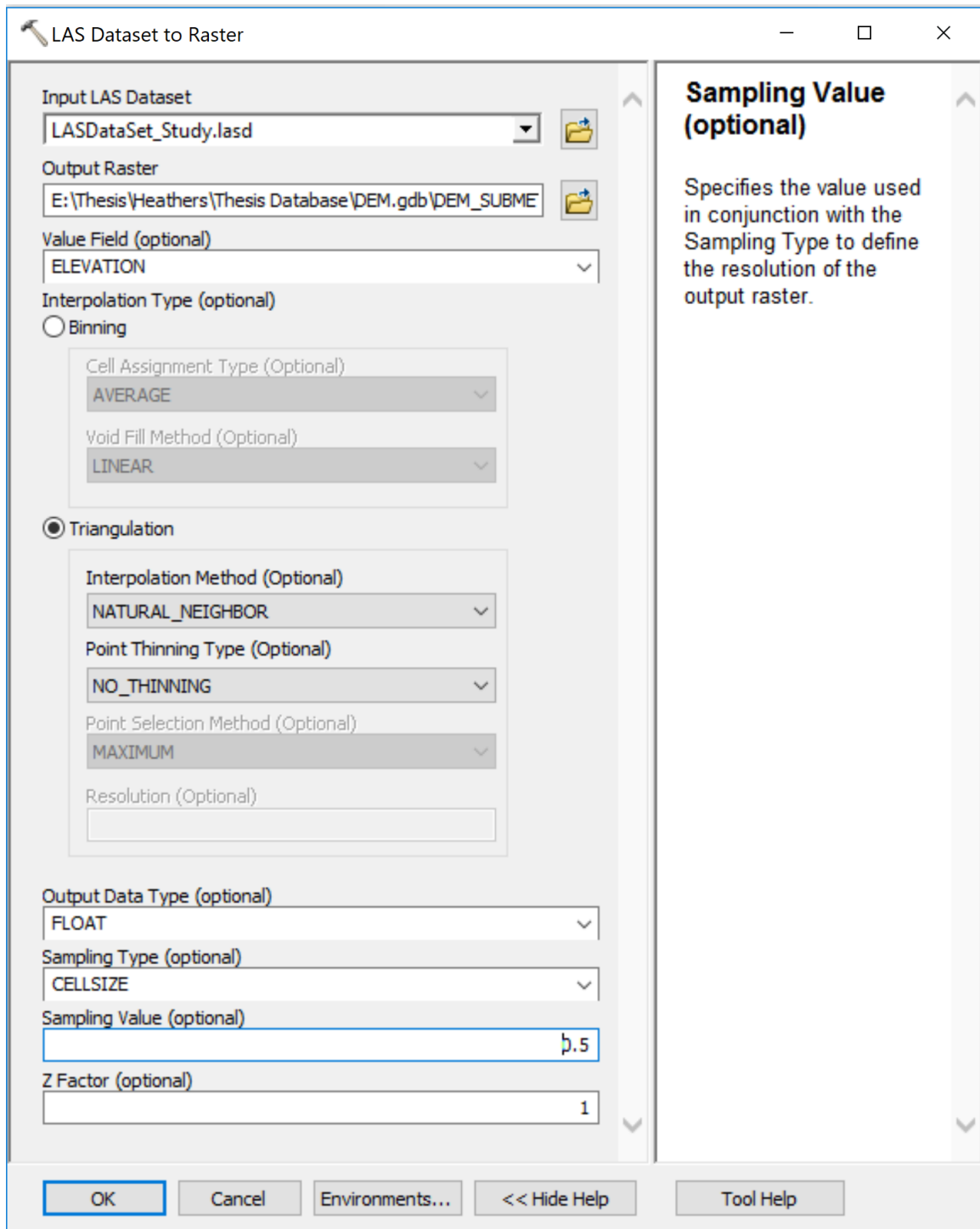


Figure 17: A screenshot of the LAS Dataset to Raster tool parameters. Interpolation type: Triangulation, Interpolation Method: Natural Neighbor, Sampling Type: Cell Size.

resolution (0.5 x 0.5 meter) model made with only bare earth (ground) points used to delineate karst features in the study area (Figure 18; Ehrhart, 2016).

Depression Identification

Digital Elevation Models (DEMs) with high resolution can be used to detect depressions in different ways. Sinkholes are often seen as hydrologic anomalies instead of topographic anomalies, where the connection to other locations of flow accumulation is taken into consideration (Reece, 2018). For this study, the *fill-difference method* was used to delineate depressions and sinkholes. This method uses a tool that was originally designed to reduce surface complexity and remove small imperfections in the data to extract features that have a pour point.

In order to identify depressions and sinkholes in this model, the *Fill* tool under the *Hydrology* section in ArcMap toolbox was used. When this tool was first created it was meant to be used to remove anomalies and smooth data so that flow calculations could be performed, but recently it has been used to identify depressions. The *Fill* tool is a combination of multiple tools, such as Focal Flow, Flow Direction, Sink, Watershed, and Zonal Fill, used together to locate sinks and fill them to their pour point. This process is repeated until all the sinks in the raster are filled, resulting in a depressionless DEM (ESRI, 2020). Once the DEM is filled, the *Raster Calculator* was used to subtract the original DEM from the filled DEM to get a fill-difference raster (Figure 19A). The *Raster*

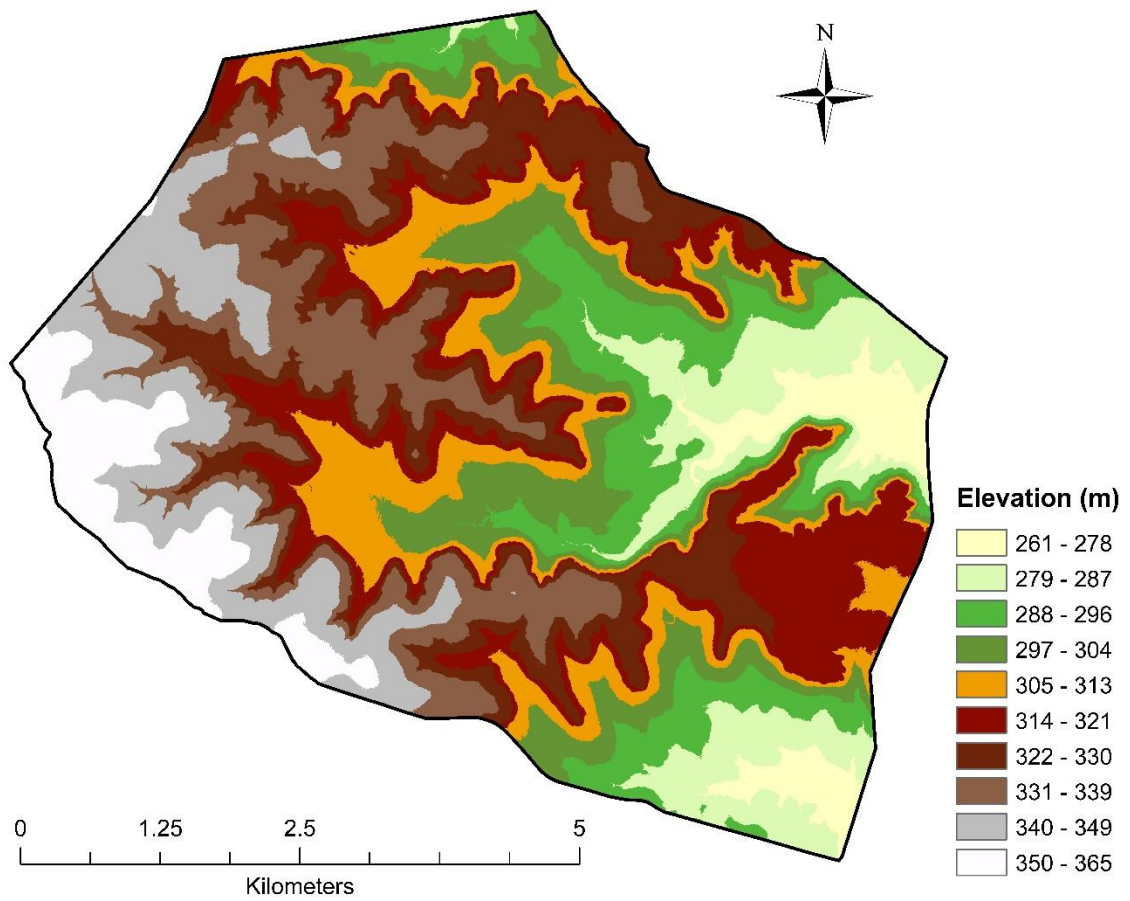


Figure 18: A 0.5-meter resolution digital elevation model of the study area created from ground returns.

Calculator tool builds and implements a single algebraic equation that will provide a resulting raster. This raster shows the depths of the depressions in the original raster, while all the other values become zero. The resulting values are reported in meters so the *Raster Calculator* was used to multiply all the values in the DEM by 100 to convert the units to centimeters. A minimum depth threshold was determined by the vertical accuracy of the LiDAR survey, which was 0.077 m (7.7 cm). With the command "VALUE <= 7.7", which classifies all values less than or equal to 7.7 as 'null' or 'No Data', resulting in a raster with depressions that have a depth greater than the vertical accuracy (Figure 19B). The remaining depressions raster cell values were converted from float to integer using the *Int* tool, which truncates the number. Now that each cell value is an integer, the *Raster to Polygon* tool was used to convert the raster image to a vector image so further spatial analyses could be done (Figure 19C). The polygons were then redefined to incorporate the surrounding areas and represent the overall size of the actual depression. First, the *Buffer* tool was used to add a 0.5-meter buffer to incorporate surrounding areas. Second, the *Dissolve* tool was used to dissolve any overlapping cell boundaries. When using this tool, the create multipart features was unchecked in order to not have a multipart feature class. Third, the *Smooth* tool was used to remove hard cell boundaries. The PAEK (polynomial approximation with exponential kernel) method was used and the smoothing tolerance was set to 0.25 meters. Lastly, the *Simplify* tool was used to remove

extraneous bends, but keep the general shape of the polygon. The bend simplify method was used and the smoothing tolerance was set to 1 meter (Figure 19D). The flow diagram in Figure 20 displays the entire process of delineating depressions from the DEM and converting them into polygon features with geometric attributes. Once that was complete, the depressions could be filtered based on their spatial attributes and relationship to other specific features. Each polygon in the model represents a single depression; after the delineation process, a total of 60,437 depressions remained in the database. The remaining depressions were classified based on filtering mechanisms that aided in determining whether the feature was a naturally formed karst feature or an anthropogenically formed feature.

Geometric Properties of Depressions

To further analyze the relative stage of depression development and determine the accuracy of the LiDAR model, geometric properties were calculated. ArcGIS 10.6 offers multiple built-in tools that can calculate these measurements as well as add attributes to the depression shapefile table that can be used to calculate other measurements. The following geometric properties for each sinkhole were calculated: area, depth, length, width, orientation, perimeter, and eccentricity.

The geometry for each depression was calculated using the *Zonal Statistics as a Table* tool and the *Minimum Bounding Geometry* tool. The *Zonal*

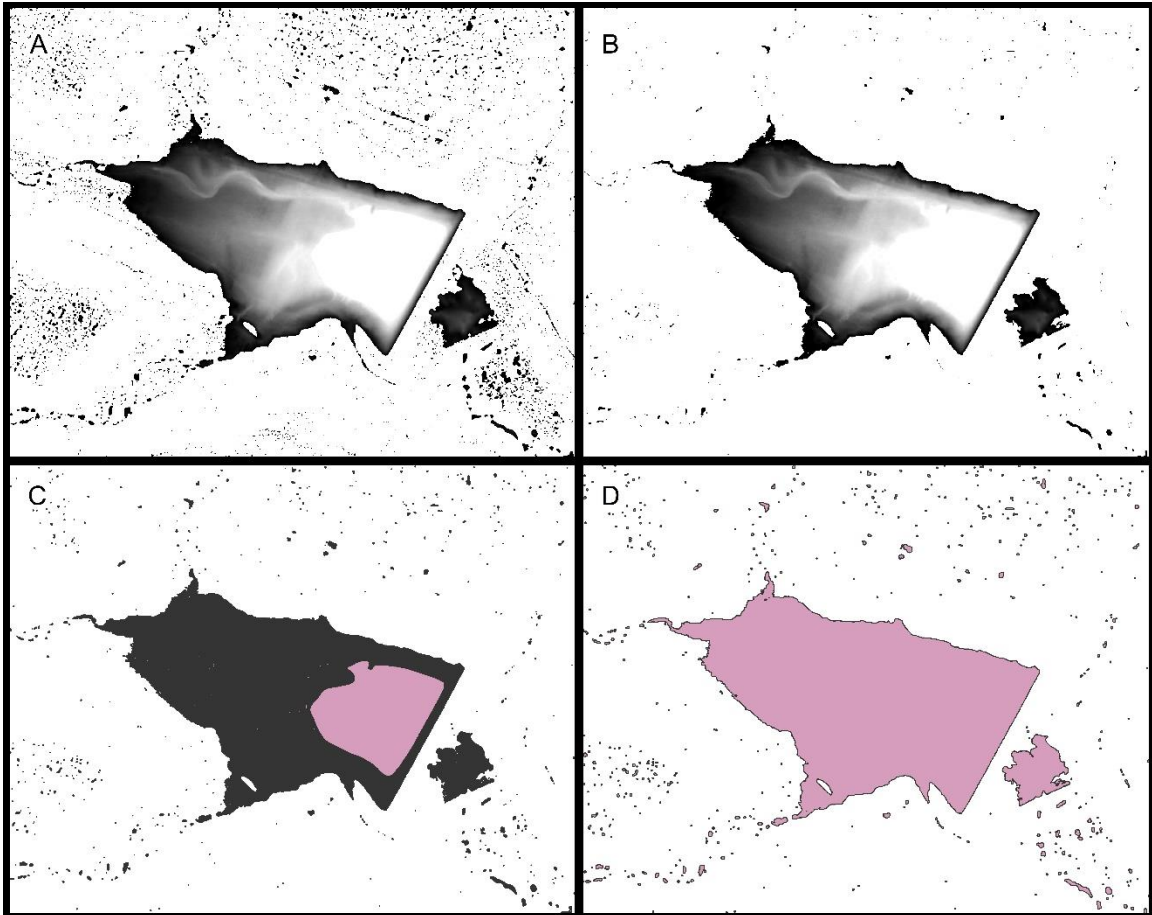


Figure 19: A) Fill difference DEM displaying delineated features. B) Fill difference DEM converted to integer displaying only depressions that are greater than the 0.077 m vertical accuracy. C) Polygon features created by running the *Raster to Polygon* tool. D) Polygons of delineated features with 0.5 m buffer, dissolved, smoothed, and simplified.

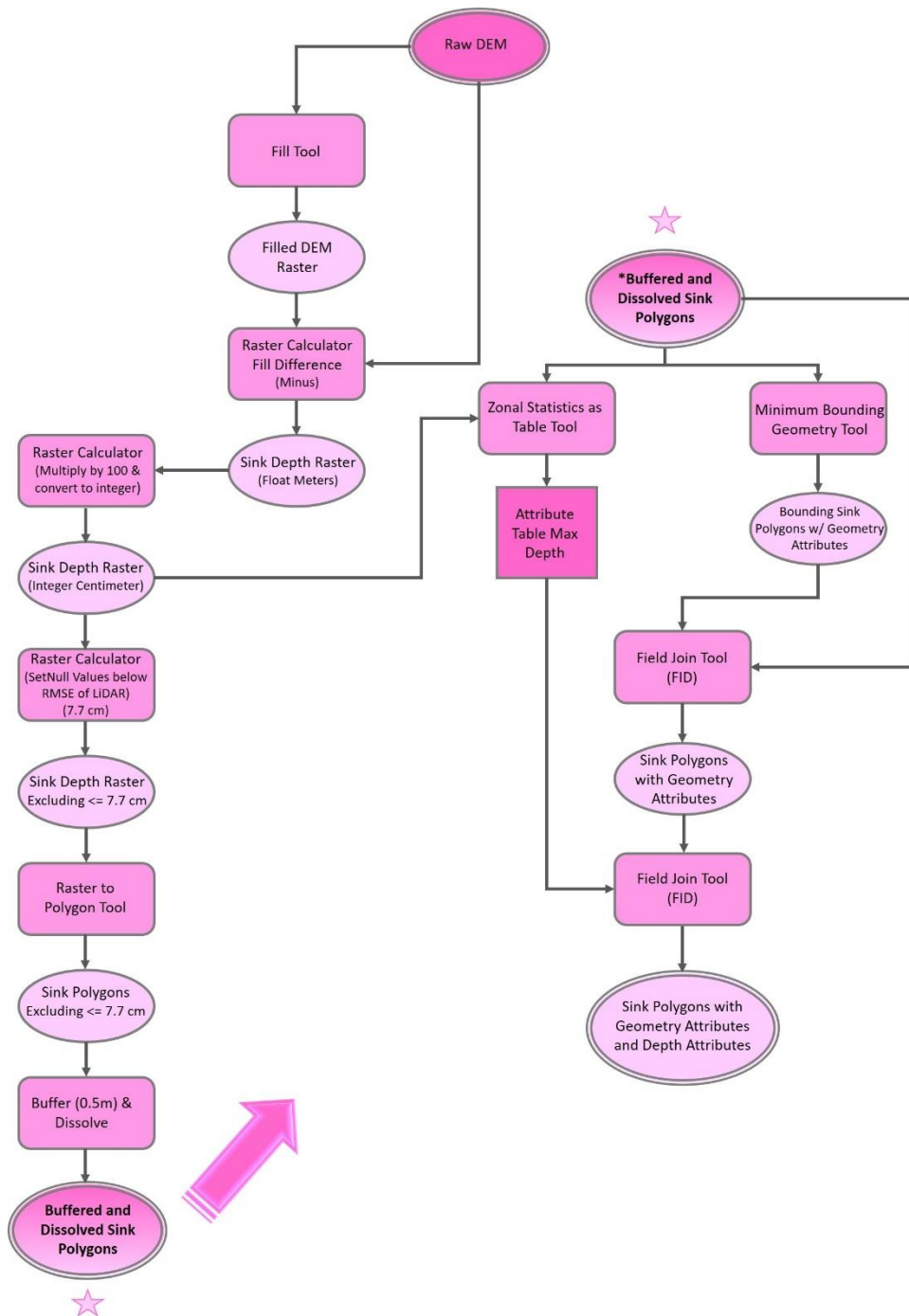


Figure 20: Flow chart for delineating features from the DEM and gathering geometric properties such as length, width, depth, etc.

Statistics Tool assigned a feature identification (FID) number to each depression attribute row that corresponded to the FID assigned to the original depression polygons. This tool then extracted data from the original DEM in the specific areas of the depression polygons. The geometric measurements calculated by this tool are depression area, as well as the maximum, minimum, and mean depth of each polygon. When the table was completed, it was then joined to the depression polygon using the *Field Join* tool. The *Minimum Bounding Geometry* tool was used to calculate other geometric properties of the polygons. The polygon type was set to *convex hull*, so that a convex polygon was digitized around the polygon of the depression. The resulting minimum bounding geometry polygons now have geometric attributes such as length of the major and minor axis and the orientation of the major axis. The *Field Join* tool was used again to add these new attributes to the polygon shapefile with the previous measurements. Lastly, additional fields can be added to the attribute table and measurements can be calculated using the *Field Calculator* or the *Calculate Geometry* tab. The *Field Calculator* can be used to build equations to calculate measurements based on other fields in the attribute table. For example, the eccentricity of each depression can be calculated by dividing the width by the length to get a ratio that helps determine circularity of the feature. The *Calculate Geometry* tab was used to automatically calculate the feature properties that are based on the spatial or geometric characteristics and the location (ESRI, 2020).

After all these calculations, each polygon contained the geometric properties in one attribute table.

Depression Classification

The depression identification process identified every depression that was present in the DEM, including non-karst forming features associated with streams, water bodies, roadways, and other anthropogenic influences. To be able to identify features that resulted from natural or anthropogenic activities, the depressions were filtered and classified by their spatial relationship to other existing features such as streams, water bodies, and roads. The underlying lithology of the depression is the most important factor in determining the influence of its formation. The geology must be susceptible to dissolution and localized topographic relief. The depth or range of elevation values that corresponded to an existing depression, the area, and the land cover classification of each depression was also used in the characterization process.

Depressions were first classified based on their underlying geology, as this is one of the most important factors in supporting the natural development of karst features (Figure 21). The Edwards and Comanche Peak formations are the only two units in the study area that are susceptible to naturally forming karst features. Any depressions that were not within those units were not considered to be natural karst features. When the filter was applied, a total of 16,922 features were removed because they did not lie within the Edwards or Comanche Peak.

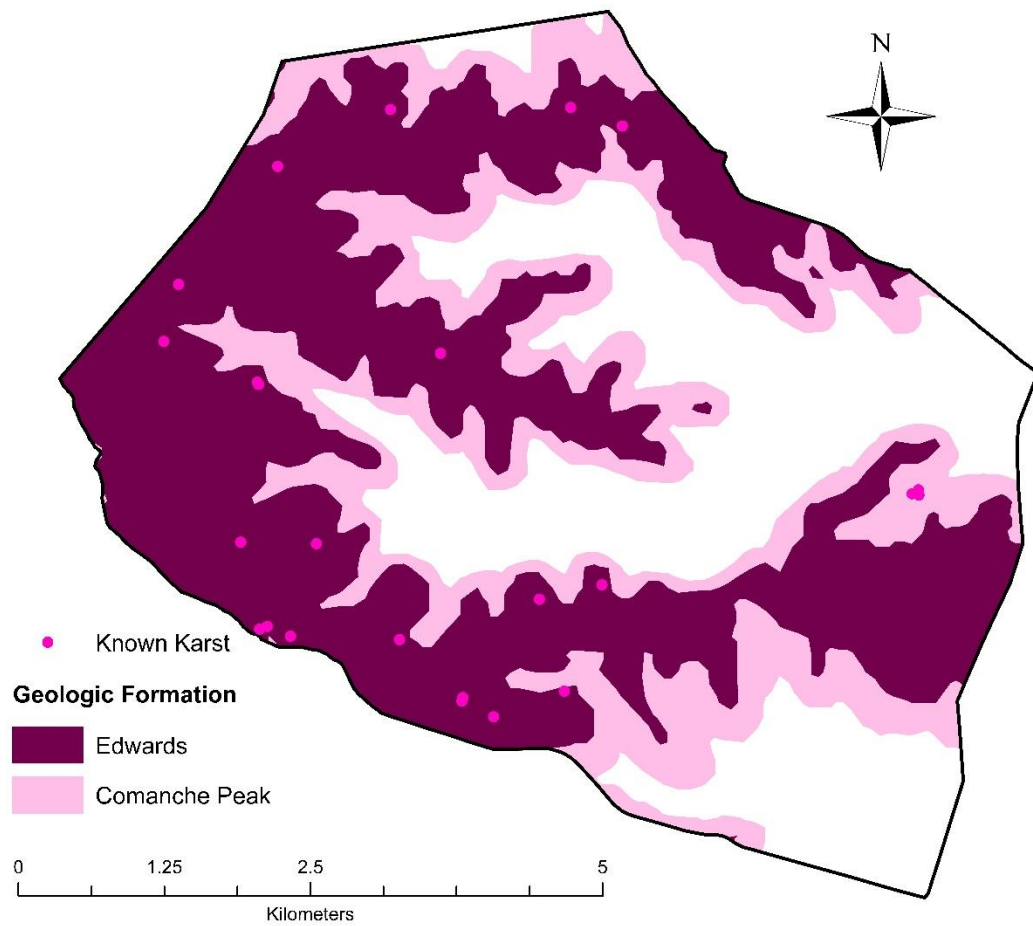


Figure 21: Map showing the extent of the Edwards and Comanche Peak formations, which are the only two formations within the study area that are susceptible to karst development.

Streams and bodies of water naturally incise the land creating anomalous lows in the stream beds or bodies of water than can appear to be sinkholes. However, these features are not karst features because they are not formed through karst processes. Streams were delineated using the Flow Accumulation tool. This tool creates a raster that measures the amount of accumulated flow into each cell, this is calculated by accumulating the weight for all cells that flow into cells with lower elevations (ESRI, 2020). Output cells that had a high flow accumulation can be used to map stream channels. The stream raster was then converted to a polyline shapefile using the *Raster to Polyline tool* (Figure 22). Streams throughout the study area range in size and depth, so buffering distances should not be the same for all streams. The *Slope Analysis tool* was used to conduct a slope analysis to look at the slope in the stream regions and define buffers based on the slope break of the streams (Figure 23). It was also used to look at the widths of different streams based on slope break in order to characterize streams into major and minor streams (Figure 24). Major streams on average were between 8-9 meters wide at the base of the stream and 26-28 meters wide from slope break to slope break. Features during traverses were discovered more than 11 meters away from a major stream. Therefore, major streams were buffered 10 meters to include areas that could be influenced by stream flow. Minor streams in the study area were on average three meters wide with shallow depths, so they were buffered one-meter buffer

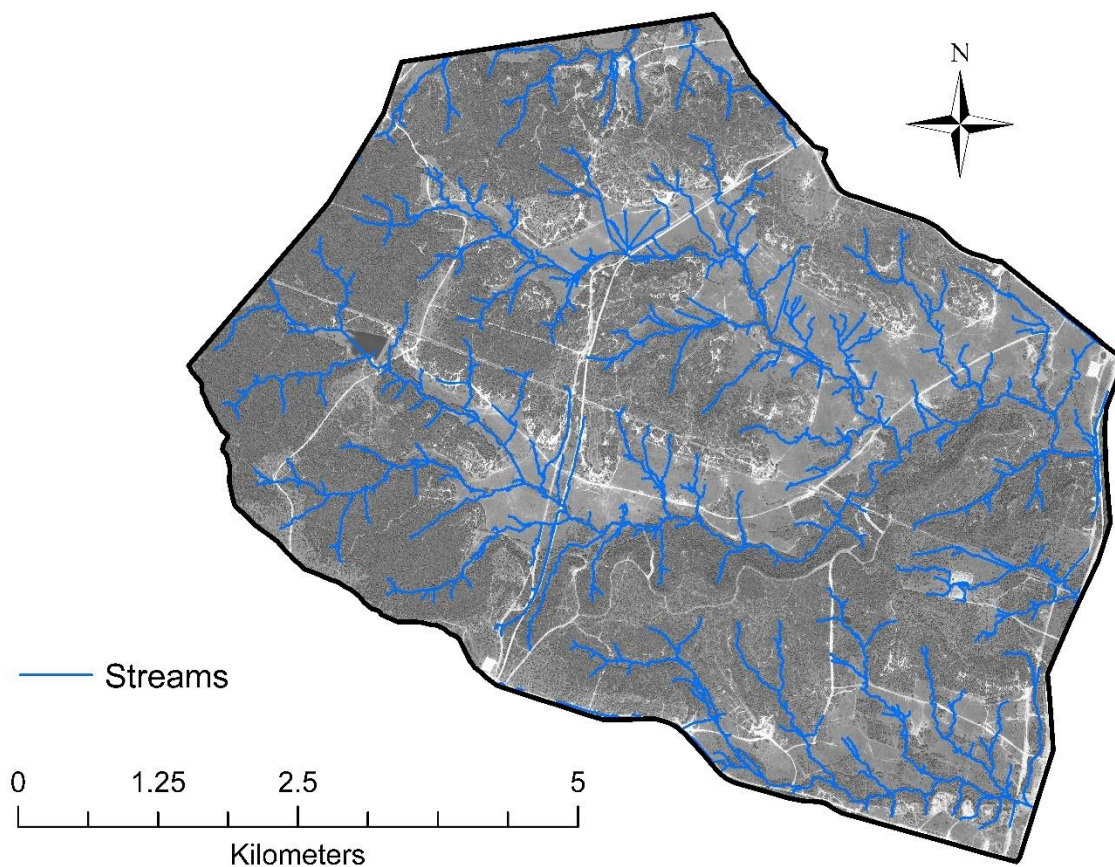


Figure 22: A map showing the stream network that was created using the *Flow Accumulation* tool. The DOQQ digital aerial imagery was collected by the National Agriculture Imagery Program during the 2018 agricultural growing season and through the winter and spring of 2019. They were downloaded from the Texas Natural Resources Information Systems on August 30, 2019.

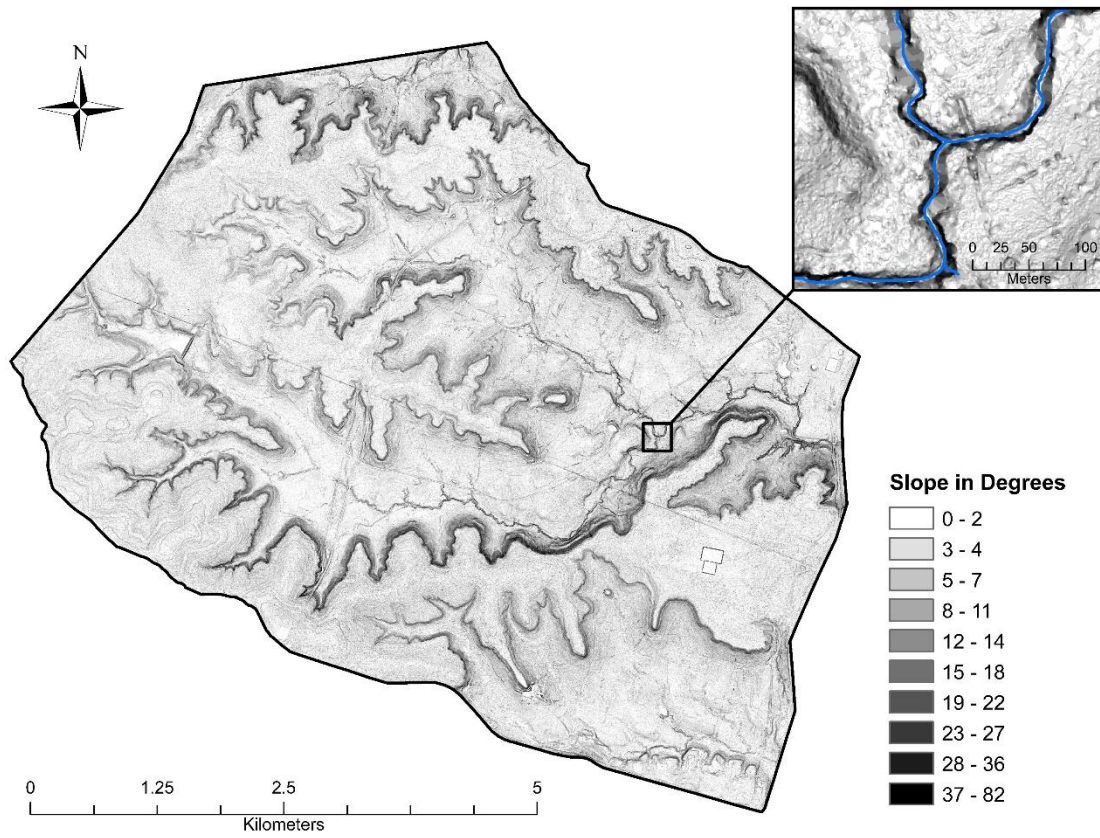


Figure 23: A slope analysis map used to characterize streams as major or minor streams based on slope breaks.

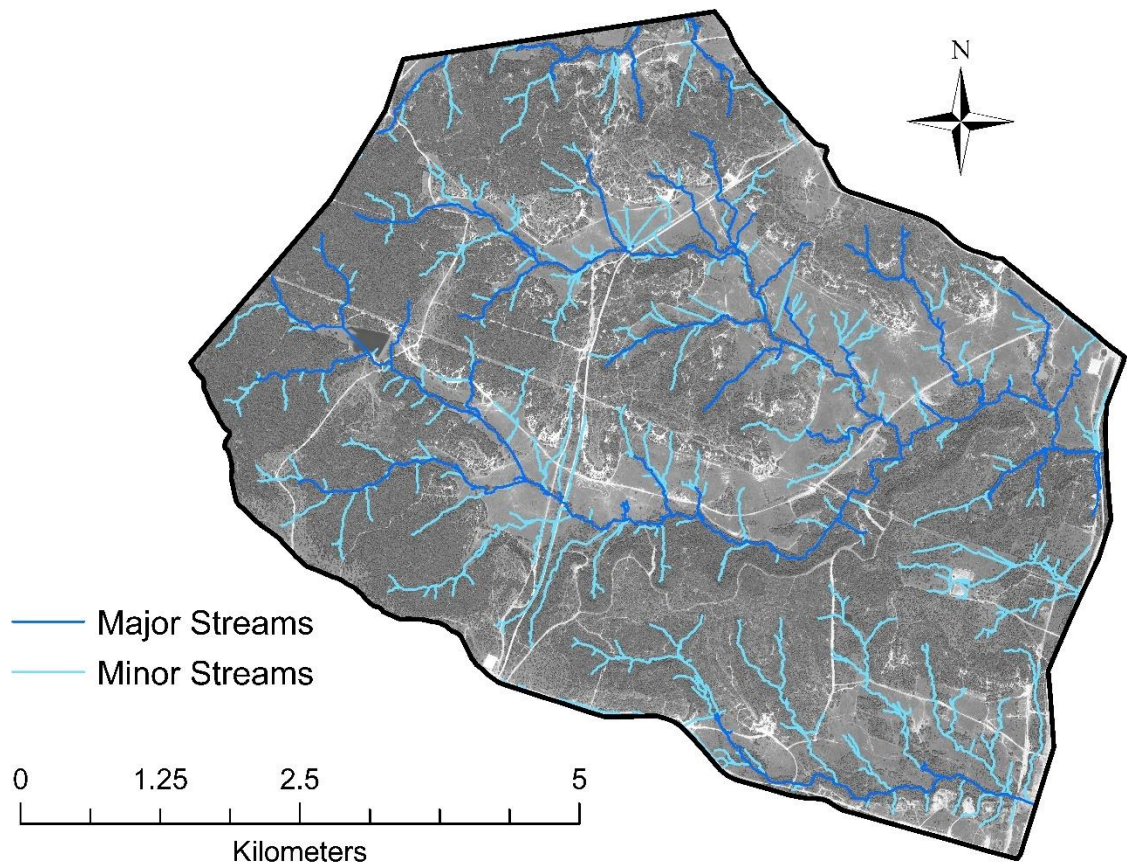


Figure 24: A map showing the major and minor streams filters. The DOQQ digital aerial imagery was collected by the National Agriculture Imagery Program during the 2018 agricultural growing season and through the winter and spring of 2019. They were downloaded from the Texas Natural Resources Information Systems on August 30, 2019.

on each side to include areas that could be influenced by stream flow. When these filters were applied 3,386 features were removed from the major streams filter and 3,917 features were removed with the minor streams filter. Water bodies were digitized using digital aerial imagery and the same slope analysis map used for the streams filter classification (Figure 25). The aerial imagery was a high resolution 60-centimeter digital aerial imagery that was downloaded from the Texas Natural Resources Information Systems. These images were acquired by the National Agriculture Imagery Program during the 2018 agricultural growing season and through the winter and spring of 2019. Just like the streams in the study area, the water bodies are also different depths and sizes. Some of these features are dry, making it difficult to identify the entirety of the feature. The slope analysis map was used to identify the locations of the bodies of water and look at the slope break to be sure the full size of the feature was included in the digitization process (Figure 26). The area of each digitized water body was calculated and resulted in water bodies being classified by their surface area as water bodies with an area greater than 1000 m² and water bodies with an area less than 1000 m² (Figure 27). Water bodies with an area greater than 1000 m² were buffered 20 m to include surrounding areas that could contain any features influenced by this feature. Water bodies with an area less than 1000 m² were buffered 10 m buffer to include surrounding areas that could contain any features influenced by this feature. When these filters were applied, 509 features were

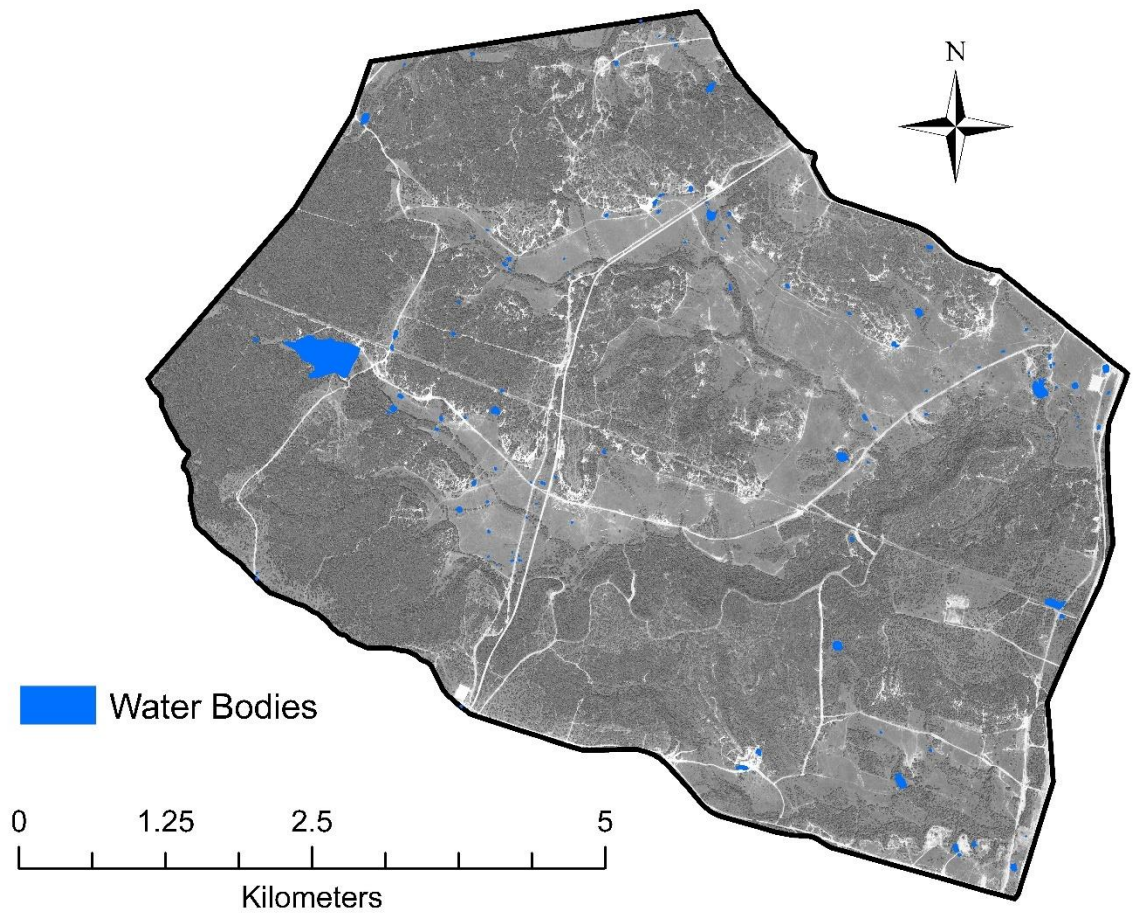


Figure 25: A map showing the water bodies that were digitized using the 60-centimeter high resolution digital aerial image. The DOQQ digital aerial imagery was collected by the National Agriculture Imagery Program during the 2018 agricultural growing season and through the winter and spring of 2019. They were downloaded from the Texas Natural Resources Information Systems on August 30, 2019.

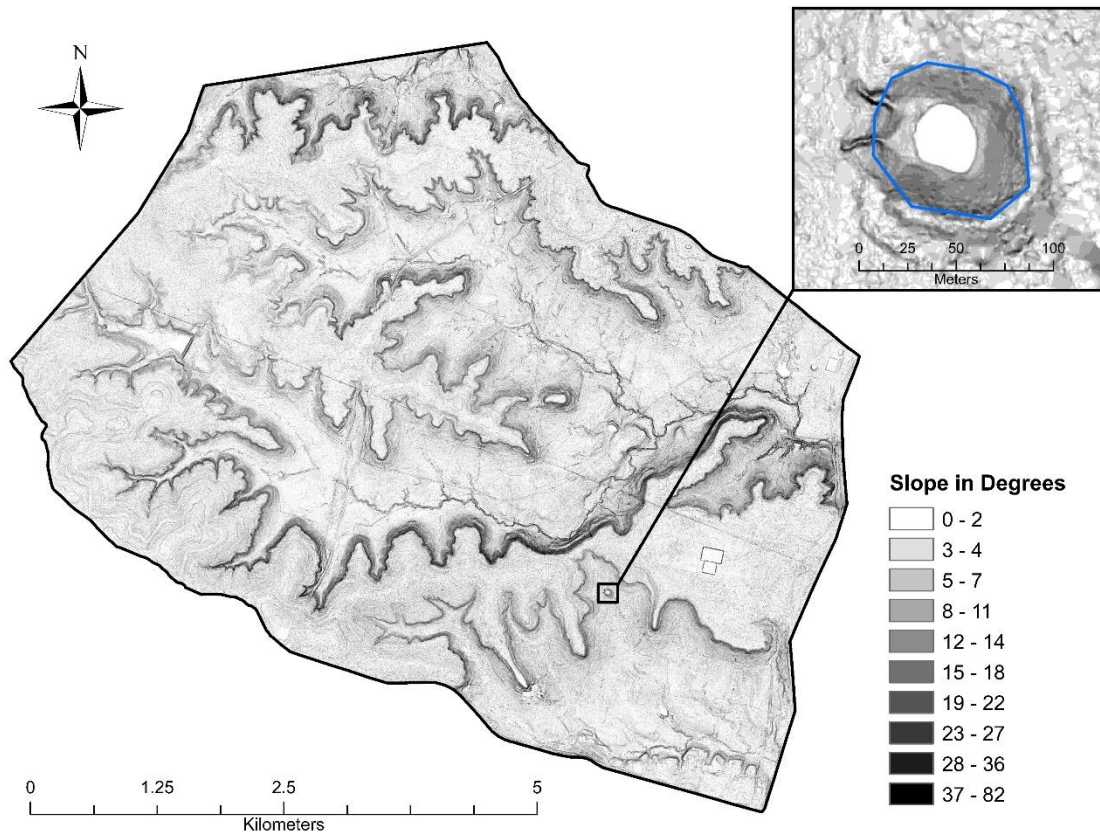


Figure 26: A slope analysis map used to digitize the full extent of water bodies to help characterize them into water bodies with an area greater than 1000 m² and water bodies with an area less than 1000 m².

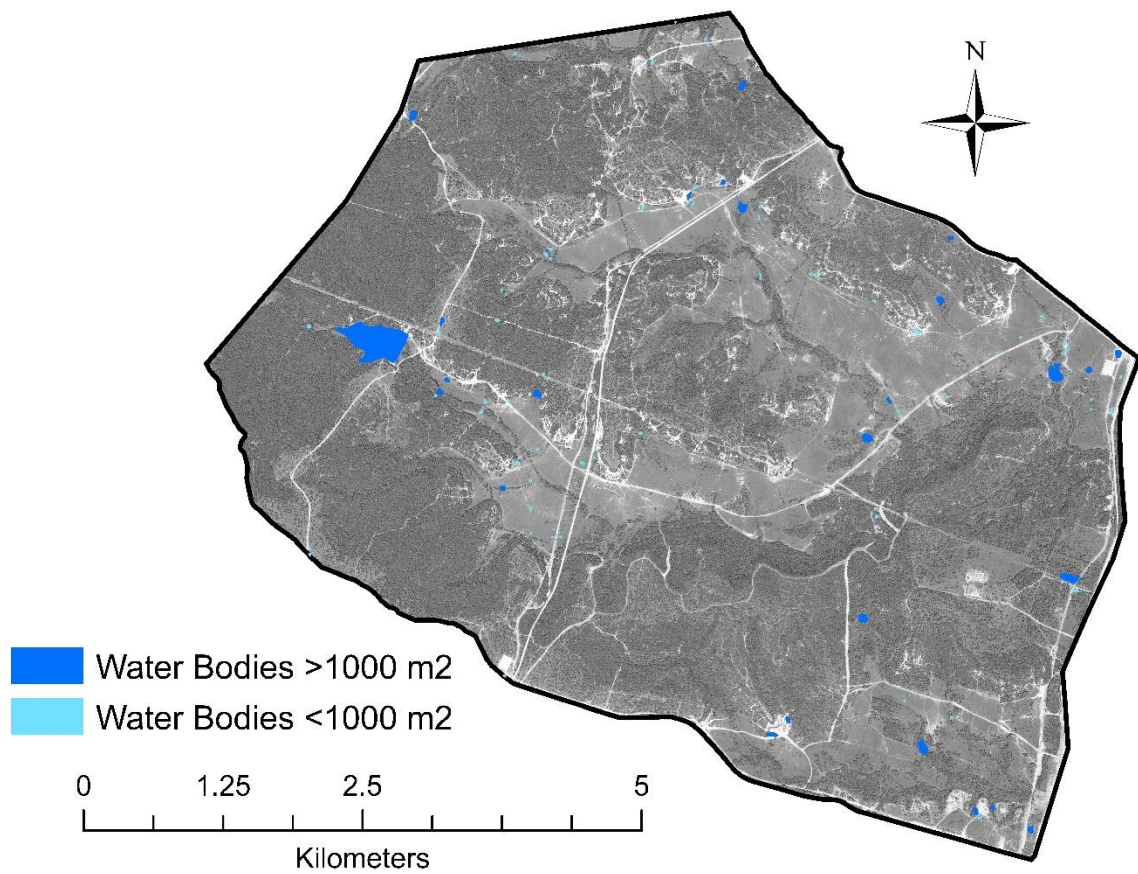


Figure 27: A map showing the water bodies with an area greater than 1000 m² and water bodies with an area less than 1000 m². The DOQQ digital aerial imagery was collected by the National Agriculture Imagery Program during the 2018 agricultural growing season and through the winter and spring of 2019. They were downloaded from the Texas Natural Resources Information Systems on August 30, 2019.

removed with the water bodies greater than 1000 m² filter and 303 features were removed with the water bodies less than 1000 m² filter.

The study area contains a vast network of paved and unpaved roads that run through all areas of the installation. The same 60-centimeter, high resolution digital aerial imagery that was used to digitize streams and water bodies was used to manually digitize all roads within the study area. An existing road database acquired from the Natural Resource Management Branch is updated as new roads are developed over time to utilize training areas. The major roads consisted of large paved roads, tank roads, and the pipeline that runs east to west through the study area. Therefore, the major roads were classified as either a paved road or an unpaved road (Figure 28). The two paved roads within the study area are the main highways with one running along the eastern side of the study area and one running through the middle of the study area. These roads were divided into two lanes and buffered 16 meters to include drainage ditches. The unpaved roads are built throughout the base to access areas for training. They are not typically the width of normal paved roads and features in the traverse survey were found approximately 14 meters from unpaved roads. These roads were buffered 13-meter buffer to include the road and areas around it that could be modified because of the equipment traveling on it. When the filters were applied, 348 features were removed with the paved roads filter and 3802 features were removed with the unpaved roads filter. The minor roads are continuously

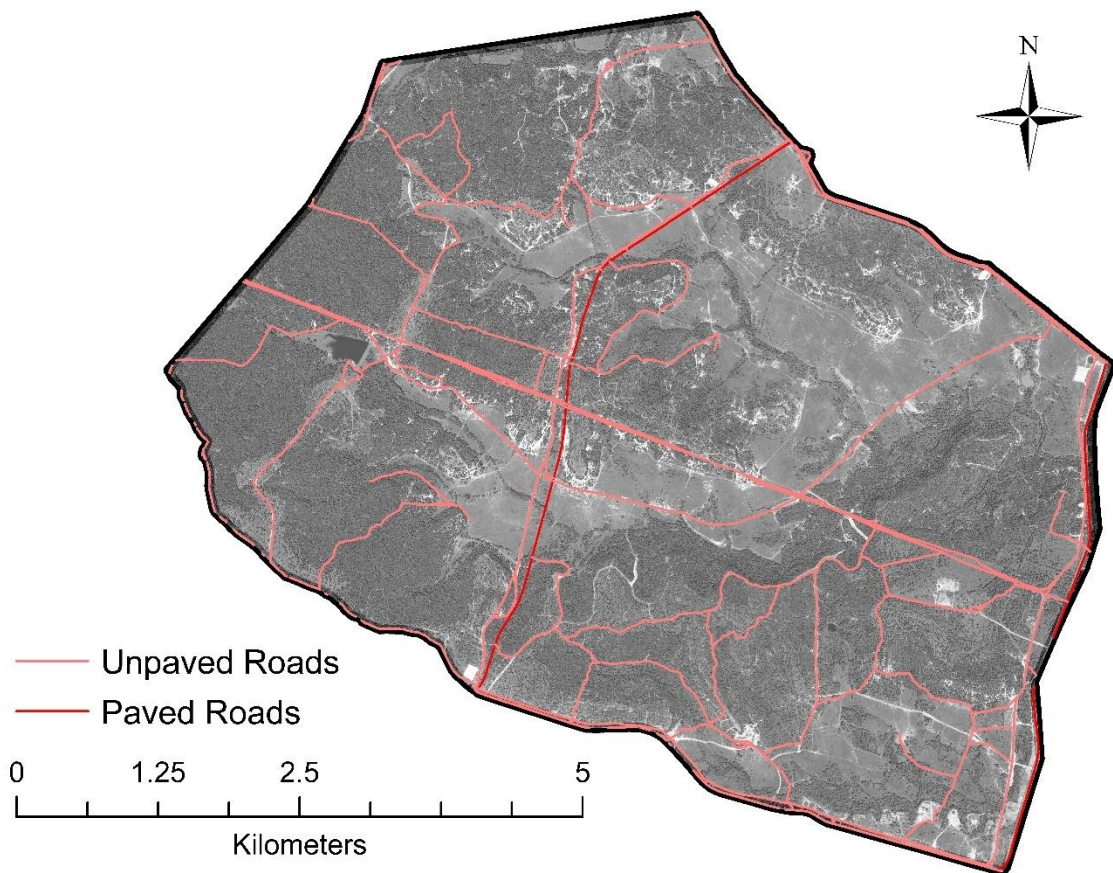


Figure 28: A map showing the paved and unpaved major roads delineated using an existing roads database that was acquired from the Natural Resources Management Branch at Fort Hood. The DOQQ digital aerial imagery was collected by the National Agriculture Imagery Program during the 2018 agricultural growing season and through the winter and spring of 2019. They were downloaded from the Texas Natural Resources Information Systems on August 30, 2019.

being created and changing throughout the study area due to military activity. They typically consist of game trails, tank/humvee trails, smaller tank roads, and dirt roads that connect to the main roads (Figure 29). Features discovered during field traverses were found within approximately 10 meters from minor roads. These roads were buffered a 9-meter buffer from the center to only include the surrounding trail areas. When this filter was applied, 19,093 features were removed with the minor roads filter.

Depressions were classified based on their land cover type and their area. The land cover types were determined by using several different datasets. When a LiDAR survey is conducted, the reflection of surfaces is measured in terms of intensity (Figure 30). Intensity values represent the strength of the return signal or the reflectivity of the surface targeted by the laser pulse (ESRI, 2020). The intensity values are also related to the vegetation cover type. Certain cover types in the area are known to have been heavily modified anthropogenically. Areas that are considered disturbed vegetation or bare ground cannot be preserved because karst features could be masked or covered by the road building, parking pads, etc. They also contain features that are not true karst features and may be the result of the equipment transport. High intensity values represent high reflectance and low intensity values represent low reflectance. The LiDAR data acquired by the Natural Resource Management Branch at Fort Hood Military Installation also included intensity images from the LiDAR survey. Along with the

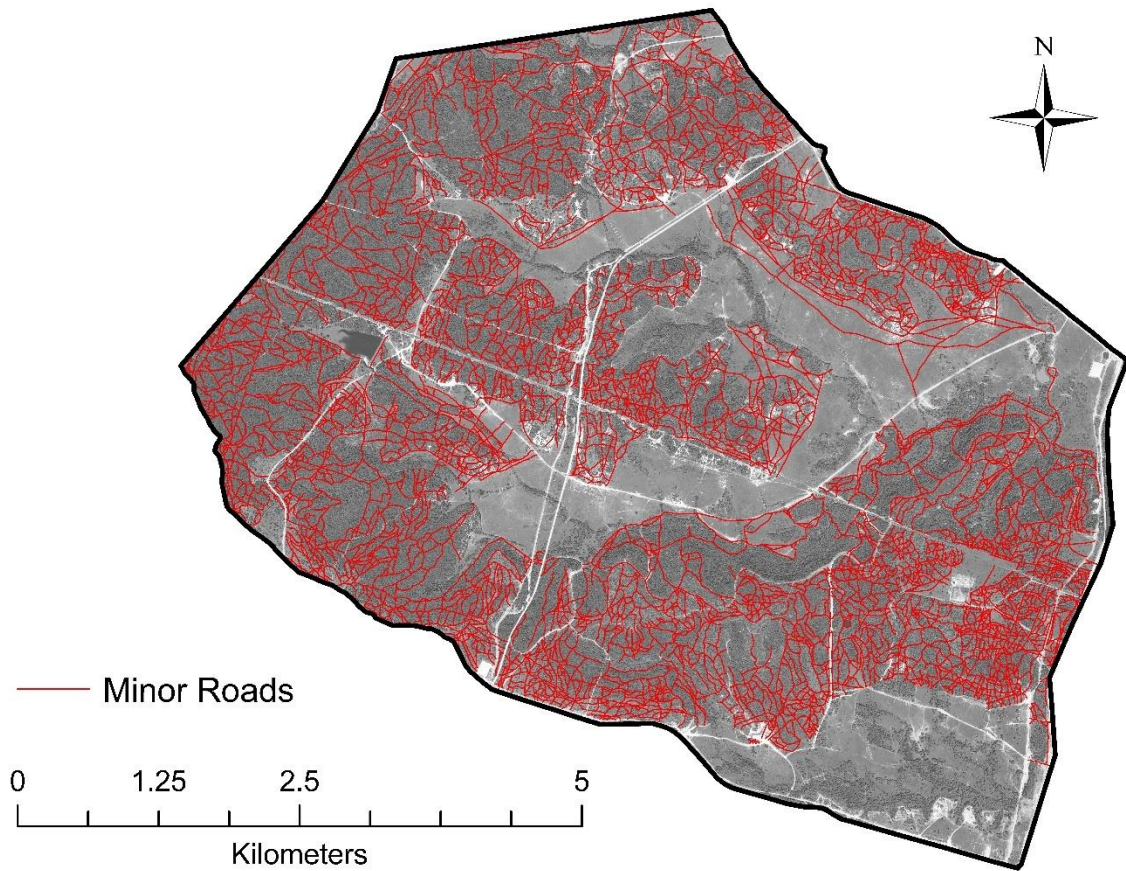


Figure 29: Minor roads delineated through digitization using 60-centimeter high resolution digital aerial imagery. The DOQQ digital aerial imagery was collected by the National Agriculture Imagery Program during the 2018 agricultural growing season and through the winter and spring of 2019. They were downloaded from the Texas Natural Resources Information Systems on August 30, 2019.

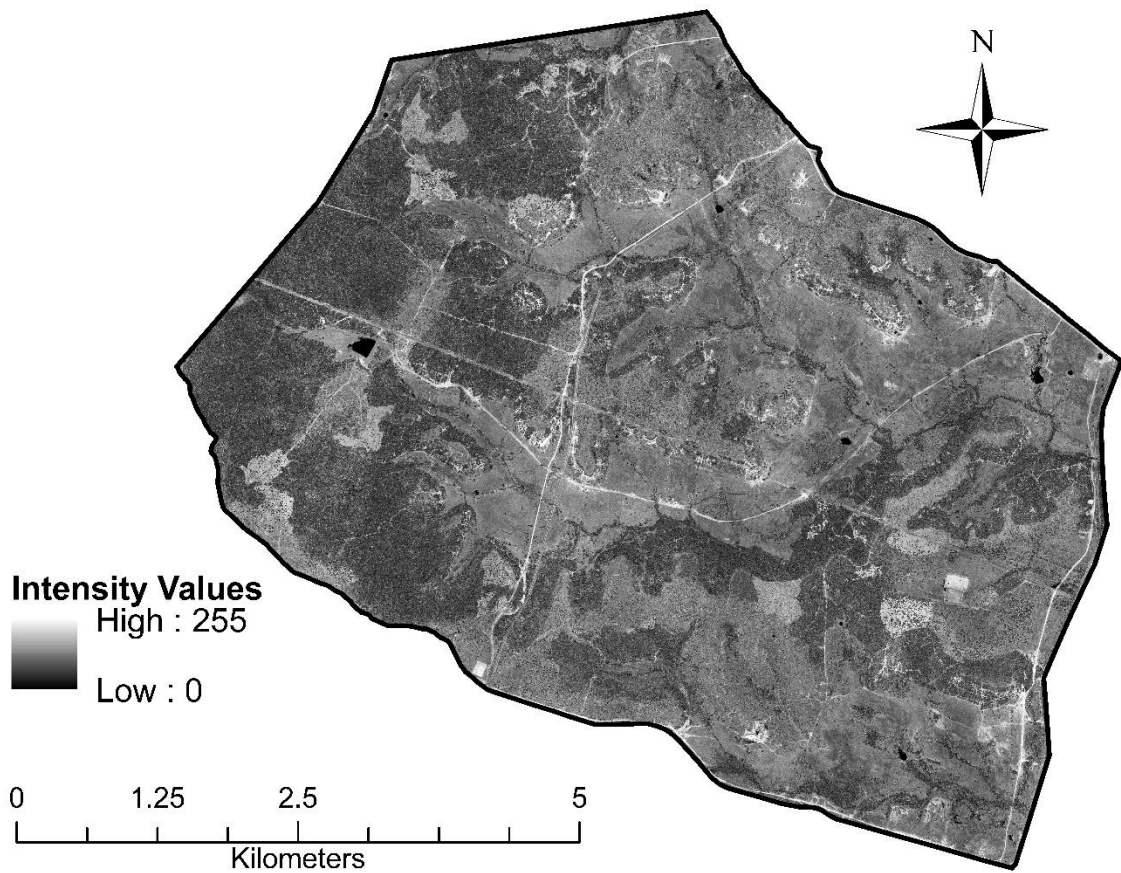


Figure 30: Intensity values for bare ground and disturbed vegetation were determined using the above intensity image that was acquired from the LiDAR survey data acquired by the Natural Resources Management Branch at Fort Hood.

LiDAR data, a vegetation classification map was acquired and used to help determine the mean intensity values for the land cover types. The same digital aerial imagery acquired from Texas Natural Resources Information System (TNRIS) used for digitized streams, water bodies, and roads was also used to update the classification map. With the combination of all the datasets, the intensity values for the land cover types were determined. Cover types were classified as either disturbed vegetation or bare ground (Figure 31). The mean intensity value for disturbed vegetation was 123.4 with a standard deviation of 28.8. This means any depression whose mean intensity value was within 94.6 and 152.2 was removed and classified as being disturbed vegetation. The land cover map was specifically based on whether the land was identified as bare earth or disturbed vegetation. The mean intensity value for bare ground was 152.8 with a standard deviation of 46.9. This means that any depression whose mean intensity value was within 105.9 and 199.7 was removed and classified as being bare ground. When this filter was applied 28,176 features were removed as either being within the bare ground or disturbed vegetation cover type. Features were based on a threshold of having an area less than 4 m² to remove artificially enhanced features (Figure 32). There are many smaller artifacts that are more than likely not true karst features. The buffering processes during the depression identification process artificially inflated the size and circularity of these features. A single cell features will be 2.25 m² because of buffering and a

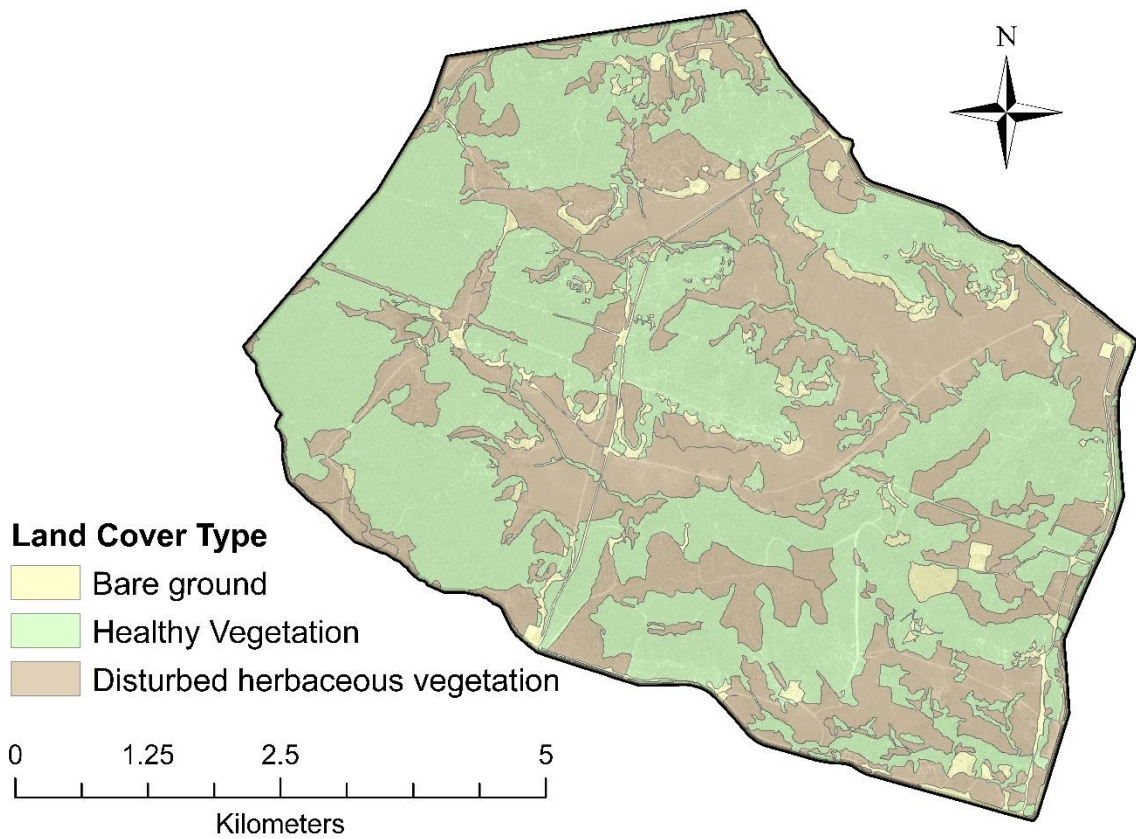


Figure 31: Landcover map showing the areas of healthy vegetation, bare ground, and disturbed vegetation. An existing vegetation map was updated using digital aerial imagery from TNRIS and the intensity images acquired with the LiDAR survey from the Natural Resource Management Branch at Fort Hood.

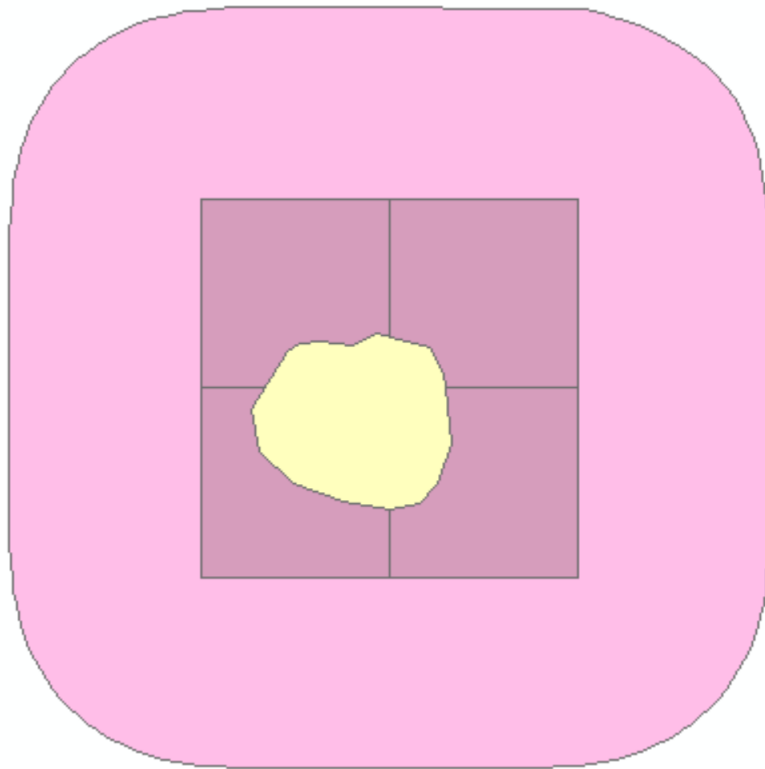


Figure 32: A figure illustrating the purpose of removing artificially inflated artifacts with an area less than 4m^2 as a result of processing.

two by two cell will be 4m² when because of buffering. When this filter was applied 35,559 features were removed because they did not have an area greater than 4 m².

After the depression database was filtered based on possible interferences with natural processes, data processing artifacts, and artificial structures, the remaining polygons represented depressions that did not interfere with any of the filtering mechanisms. Table 6 shows the number of features that interfered with each filtering mechanism. The total number of depressions that remained in the database was 4,886 (Figure 33).

Table 6: Table that contains the filter mechanisms and buffering distances used to remove features during the classification process and the number of features that interfered with each filter. Some features interfered with more than one filter and resulted in the interference count being greater than the total number of features in the database.

Interference Type	Filter	Interference Count
Geology	Lithology Shapefile	16,922
Paved Roads	16 m	348
Unpaved Roads	13 m	3802
Minor Roads	9 m	19,093
Major Streams	10 m	3,386
Minor Streams	1 m	3,917
Water bodies > 1000 m ²	20 m	509
Water bodies < 1000 m ²	10 m	303
Land Cover	Land Cover Shapefile	28,176
Area	> 4 m ²	35,559

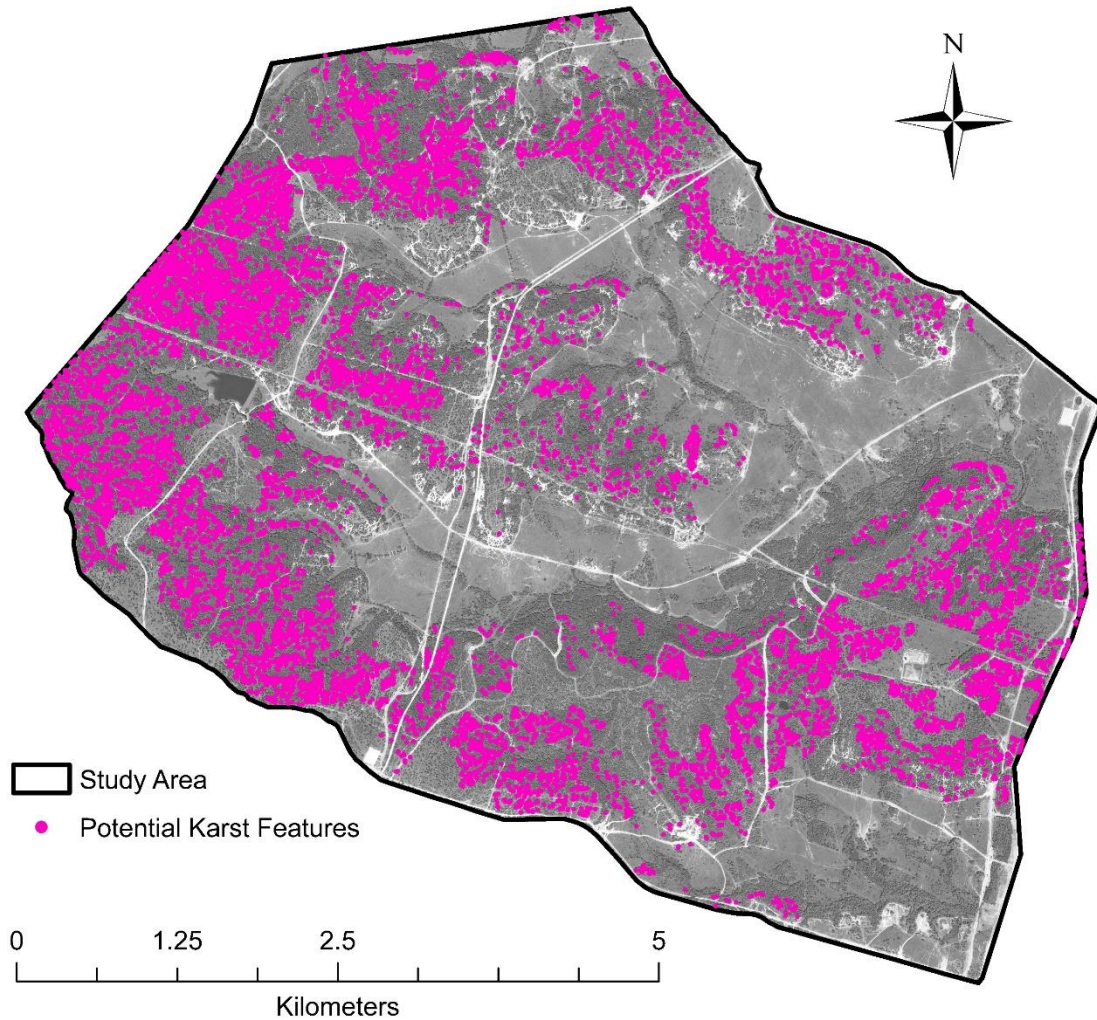


Figure 33: A map showing the remaining 4,886 potential features after the depression classification process. The DOQQ digital aerial imagery was collected by the National Agriculture Imagery Program during the 2018 agricultural growing season and through the winter and spring of 2019. They were downloaded from the Texas Natural Resources Information Systems on August 30, 2019.

RESULTS

Sinkhole Morphology and Lineament Analyses

Previous studies conducted in western Fort Hood found that the majority of karst features are the result of partial collapse and should display a near circular shape (Reddell et al., 2011). The geometric characteristics for the remaining features after filtering were calculated and used to quantitatively evaluate the remaining sinkholes in the database after filtering mechanisms were applied. Calculating circularity aids in determining the relative stage of development through the degree of collapse, which can also help determine the accuracy of the LiDAR model. The circularity of a sinkhole is determined by the ratio between the major axis (length) and minor axis (width). For a sinkhole to display perfect circularity, the ratio must be 1:1 and should not be more than 2:1. If the ratio is greater than 2:1, then the depression has an ellipsoidal shape. Many of the features in the karst potential model were too small to be accurately characterized with 0.5-meter resolution LiDAR, so the following sinkhole morphology and lineament analyses was done with features with an area greater than 10m².

The dimensions for each feature with an area greater than 10m² was entered into a spreadsheet in Microsoft Excel, and a scatter plot was generated

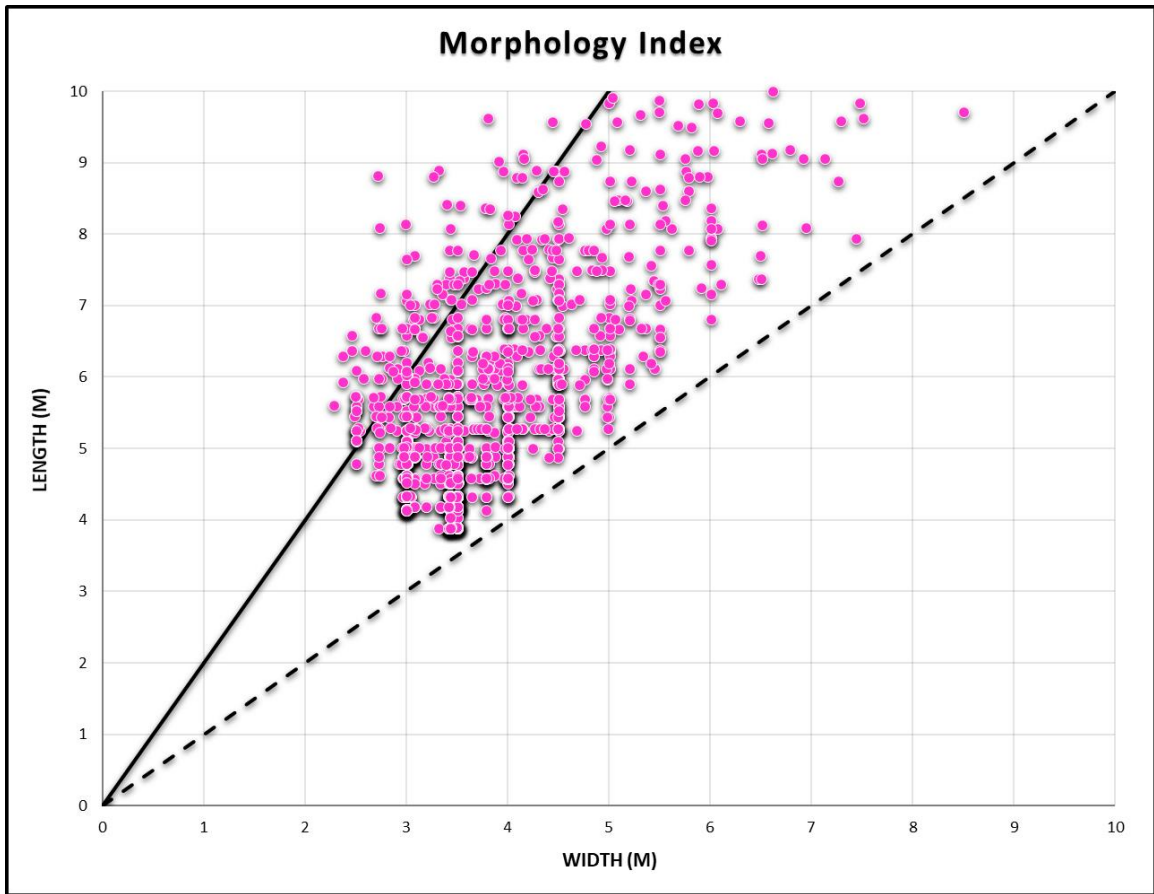


Figure 34: A graph plotting all features remaining after the filtering mechanisms were applied ($n=1,253$). The width vs length ratio in the potential karst features where length represents the major axis. The lower trend represents circular shaped features ($L/W = 1$) and the upper trend represents elliptical shaped features ($L/W = 2$).

to analyze the length-to-width ratio (Figure 34). Two lines with a slope of one and two were plotted to show the relative shape of the features. The upper trend line with a slope of two represents features that are more elliptical in shape and are structurally developed from fractures and joints, while the lower trend line with a slope of one represents features that are more circular in shape and develop from collapse. Features that plotted between the two lines had a circular to ellipsoidal morphology. A histogram of all features with an area greater than 10m^2 was created to show the morphology distribution; this data showed an average circularity ratio of 1.55 (Figure 35). This showed a right skewed distribution with points clustering towards the left. Most features were between 1.2 and 1.4, which is a more circular shape, indicating that most features are of collapse or subsidence origin. However, there is a cluster of sublinear features, which indicates there could be joint-controlled and fracture-controlled components contributing to the formation of these features or are solutional sinkholes.

The orientation of the long axis of each feature with an area greater than 10m^2 was calculated; these orientations were classified by the azimuthal direction with values ranging from 0-180 degrees. The values were then entered into the GeoRose Software to display the orientation trends (Figure 36). The orientation of major axes of GIS defined sinks trend with major drainage and ridge alignment in the study area. These trends do not correlate with major

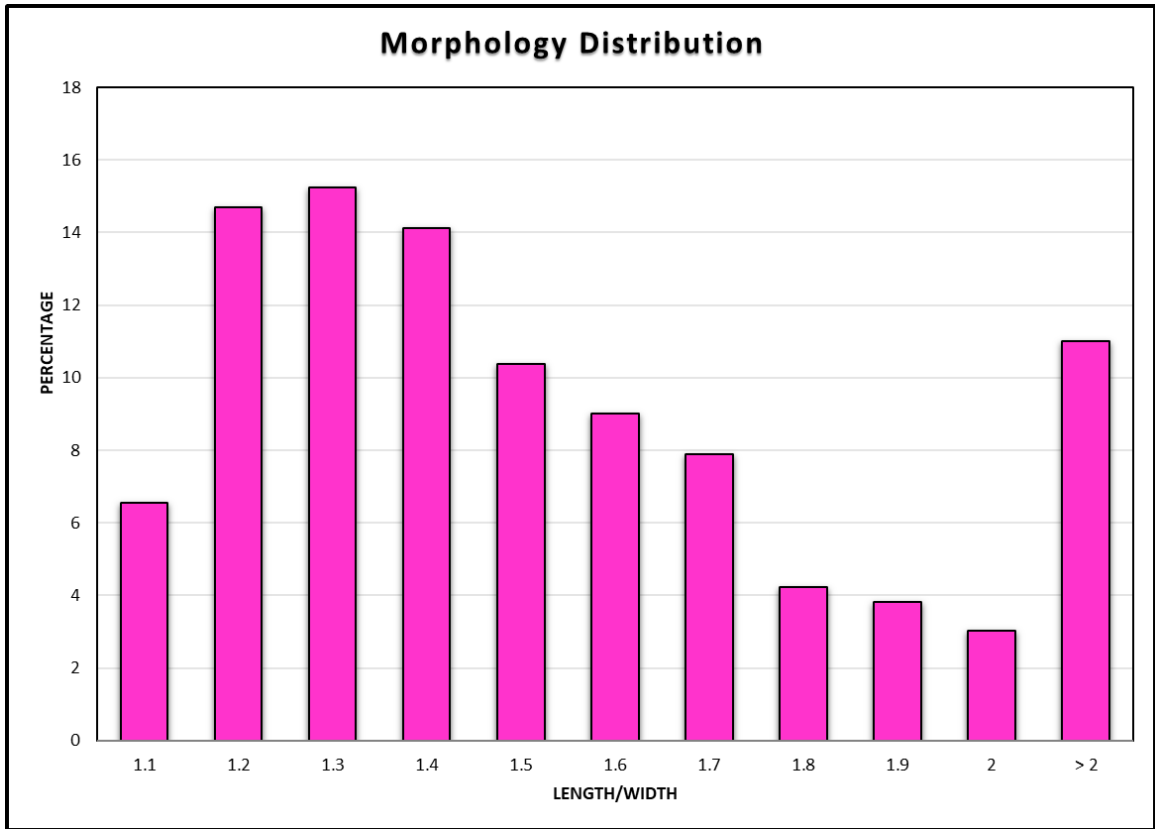


Figure 35: Histogram showing the circularity distribution of potential features with an area greater than 10 m² (n=1,253). Many of the points are within the circular shape and have an average circularity ratio of 1.55:1.

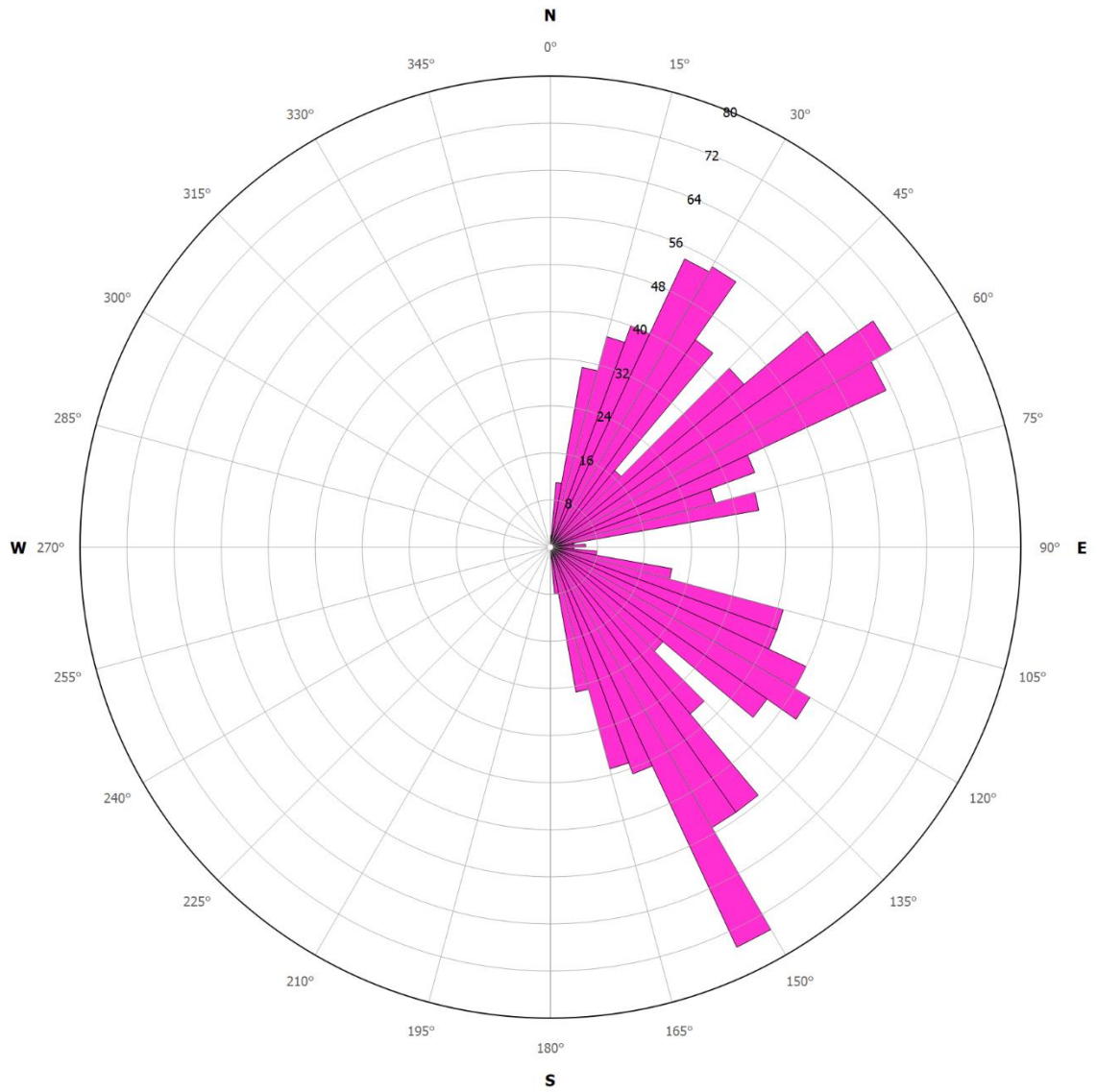


Figure 36: A rose diagram representing the orientations of the major axis of features with an area greater than 10 m² (n=1,253).

deformational events (Balcones/Ouachita trend) or the lineament analyses conducted in the Owl Mountain Province (Faulkner et al., 2019) suggesting more research needs to be conducted to understand the major lineament trends in the region and their influence on karst development.

Depression Density and Surface Area

Depression density maps were created to show the distribution and concentration of potential karst features before filtering was applied, and the non-interfering karst features after filtering. The polygons were converted to point maps using the *Feature to Point* tool, which resulted in a point map that contained the centroid of each depression. The *Kernel Density* tool was used to create four different maps.

The first two maps show the number of depressions found within one km² search radius for the depressions in the study area before and after filtering. The depression density map for all depressions showed high density areas are near minor roads or classified as either disturbed vegetation or bare ground where the military has been conducting training exercises (Figure 37). The depression density map for non-interfering depressions shows areas of high density are located on the topographically high regions, specifically the high ridges and steeper scarps (Figure 38).

The last two maps depict surface area in terms of density to illustrate the spatial distribution of depressions in terms of magnitude (Bryant, 2012). These

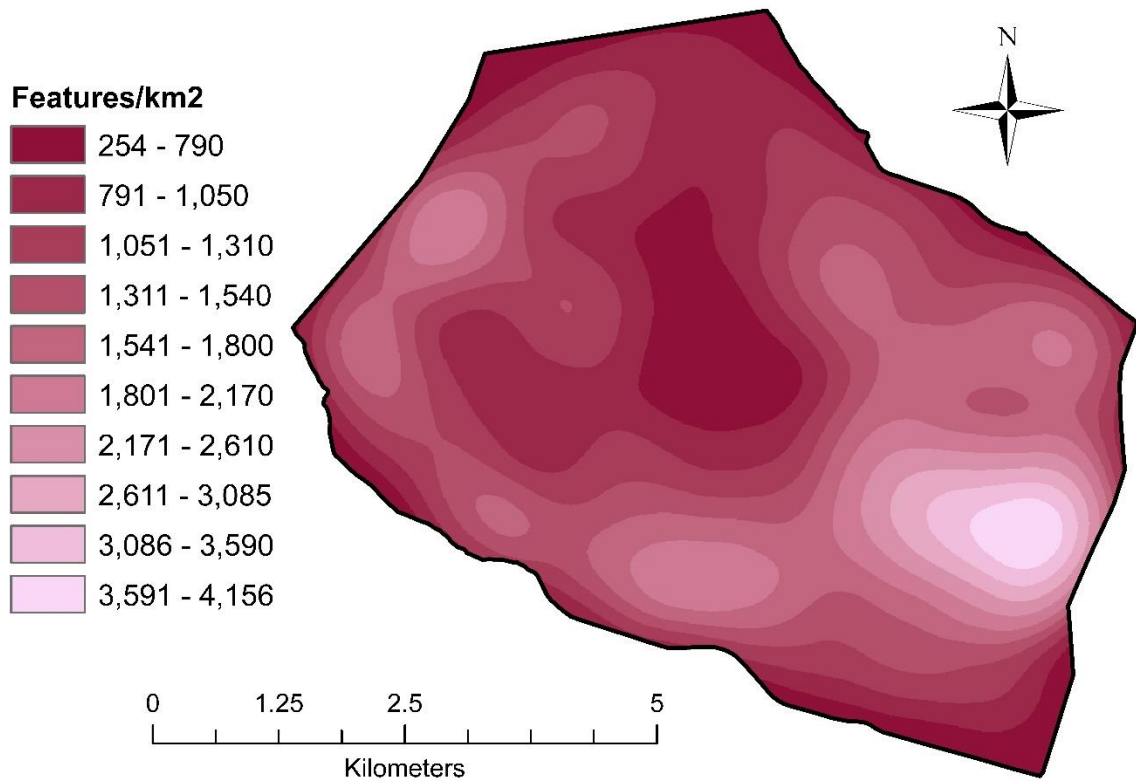


Figure 37: Depression density map for all delineated depressions within the database (n=60,437).

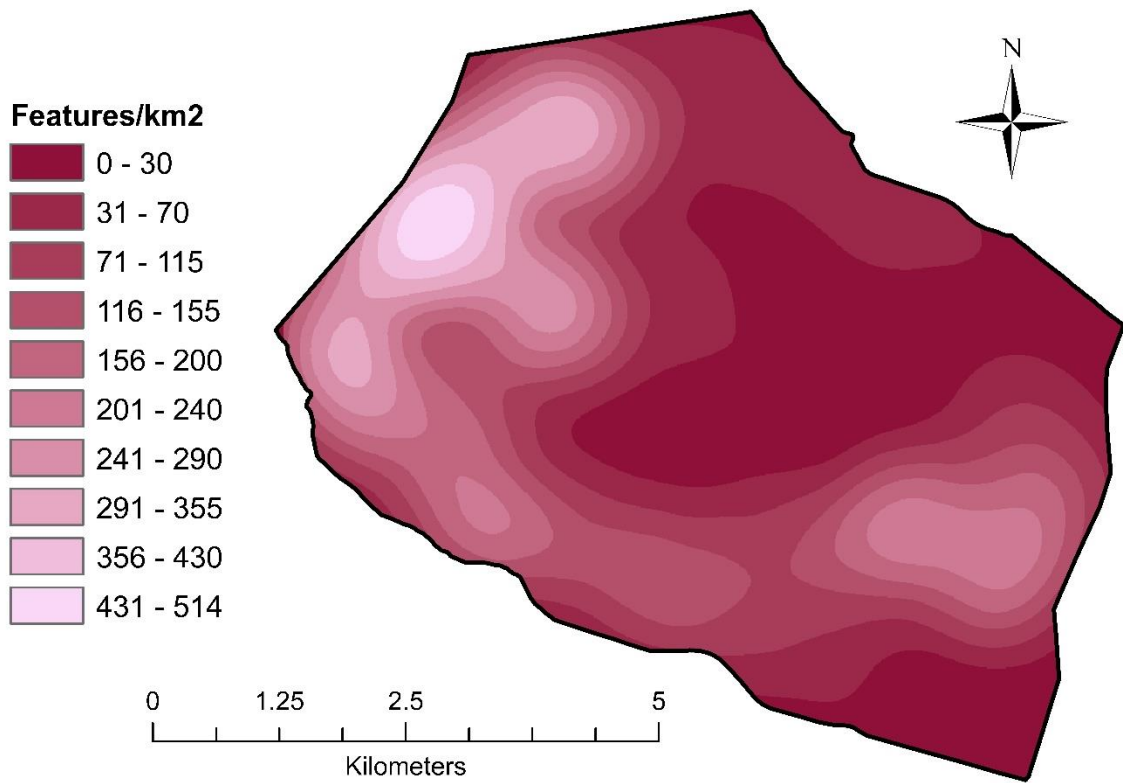


Figure 38: Depression density map of non-interfering depressions within the database after filtering (n=4,886).

maps show the weighted point density of depressions in a one km² area. The surface area map for all depressions shows that the largest coverage of depressions occur in the southwestern portion of the study area and in areas classified as disturbed vegetation and bare ground (Figure 39). The surface area map for all non-interfering depressions shows that the areas with the largest coverage of depressions occurred in clusters on topographic high ridges in the western portion centered in the middle of the ridge. There were some larger features in the eastern portion as well (Figure 40).

Accuracy Assessment

To determine the accuracy of the depression database, random points were selected using the Create Random Points tool in ArcMap and verified during field investigations. The first field checks focused on areas that contained obvious artificial features that were not formed by natural karst developing process and previously documented karst features (Figure 41). The location, shape, and size of these features were compared to the spatial and geometric attributes computed from the LiDAR survey. The positively corresponding locations and geometric properties supported the decision to proceed with further field verifications of potential karst features in the model.

To generate a list of features for field verifications of the previously used filter and buffering parameters, the *Create Random Points* tool was used to select 50 points from the potential features and 60 features (10 points from each

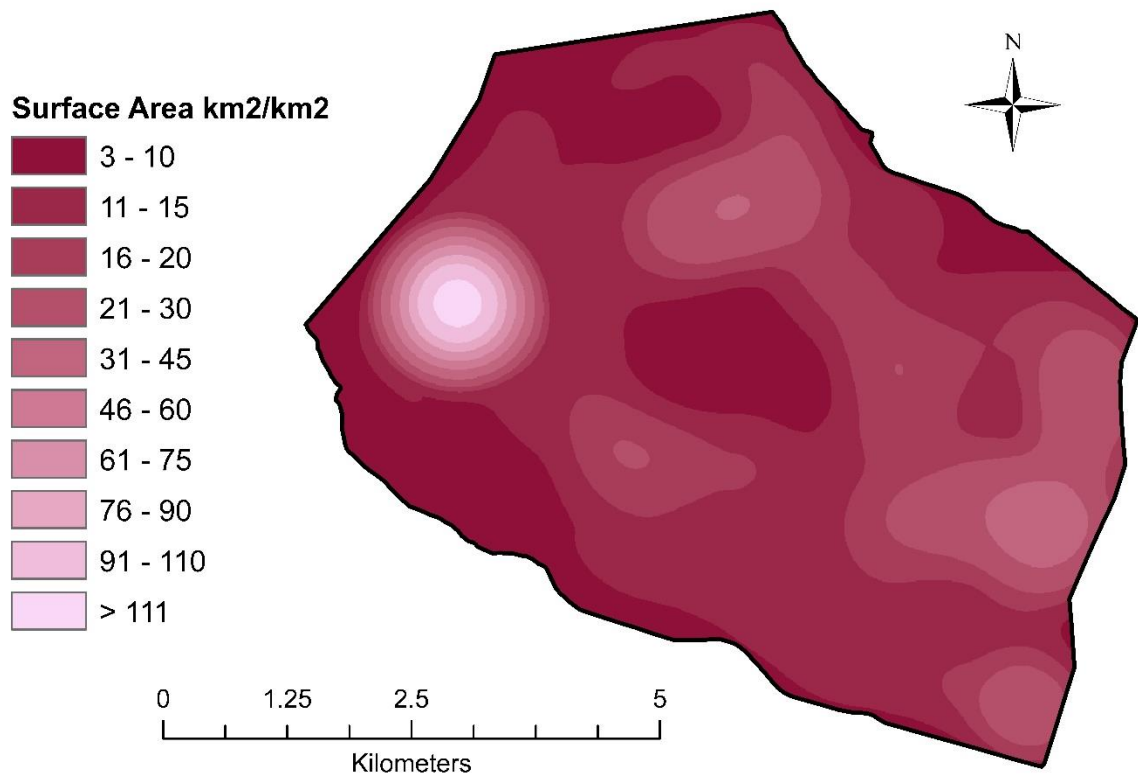


Figure 39: Surface area density map for all delineated depressions within the database (n=60,437).

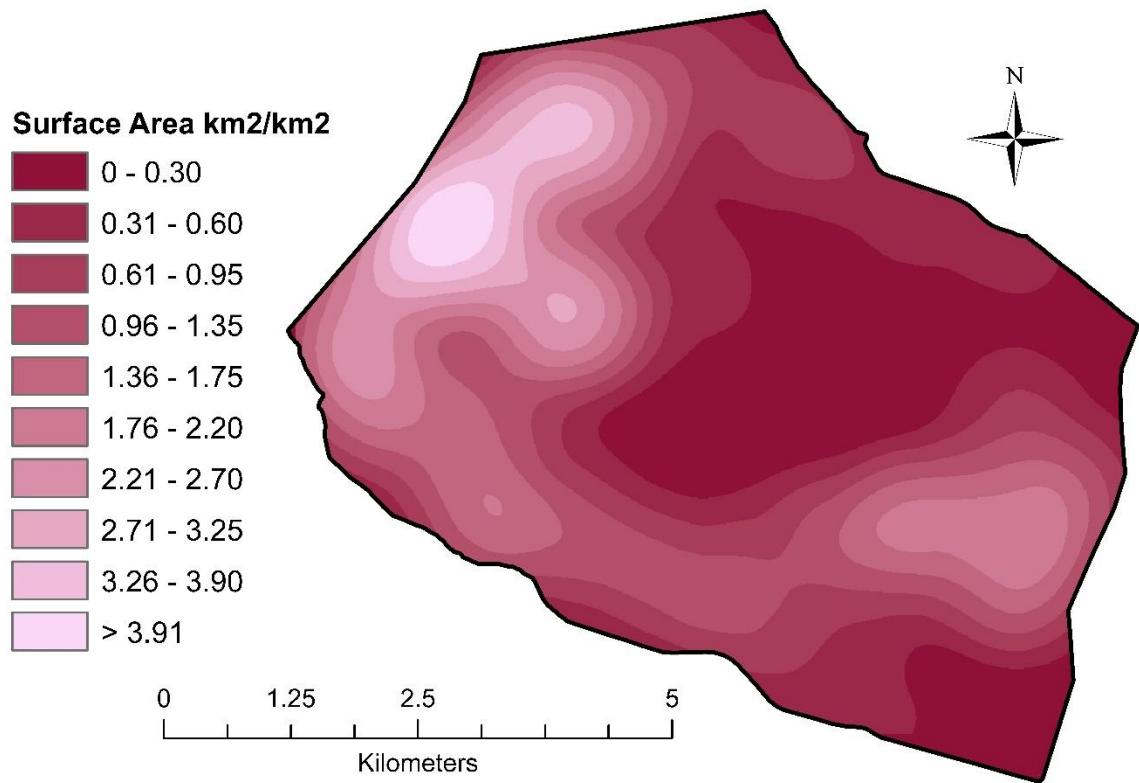


Figure 40: Surface area density map for all non-interfering depressions within the database after filtering (n=4,886).



Figure 41: A previously mapped feature in the study area from Brokeback Cave.

original filter) from the depressions removed by filtering mechanisms to evaluate the accuracy of the filtering mechanisms (Figure 42). During field investigations, each point was located and geometric measurements (major axis, minor axis, depth, orientation, etc.) were recorded for each feature. A total of 110 individual features were used in this accuracy assessment. The results for both verifications were categorized by their predicted and true conditions and entered into a confusion matrix to show the error percentages and overall true accuracy of the model. Of the 50 potential features, 28 features were characterized as real features, this gave a commission error of 56%. Of these features, many of them were semicircular, bowl-like depressions. Out of the 60 removed features, only three features were considered false negatives, with an omission error of 95%. The non-karst forming features were mainly found in drainage areas along major roads, tank/humvee ruts along minor roads, and in disturbed vegetated areas and bare ground. The overall true accuracy of the model was 77.3% and the Kappa statistic was 52.7% (Table 7).

The same set of points used to verify the previous filters and buffering parameters were then used to verify the new set of filters and buffering parameters to see if these filters improved the model. When the new filters were applied only 107 of the features could be verified, 57 from the filtered features and 50 from the true features (Figure 43). Out of the 107 total features 90 of the points were confirmed to agree with the new filters and buffering parameters. Out

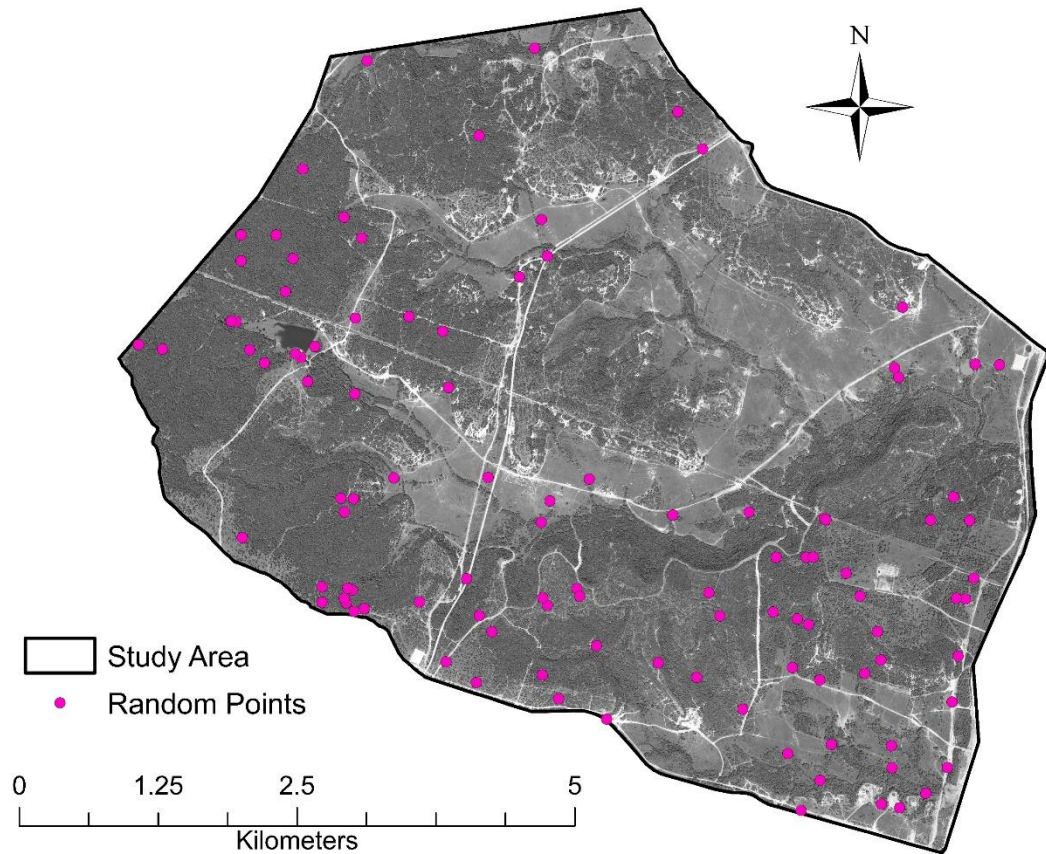


Figure 42: Map showing the location of the location of the random evaluation points (n=110). The DOQQ digital aerial imagery was collected by the National Agriculture Imagery Program during the 2018 agricultural growing season and through the winter and spring of 2019. They were downloaded from the Texas Natural Resources Information Systems on August 30, 2019.

Table 7: Confusion matrix with the features that were surveyed to assess the accuracy of the previous filters and buffering parameters.

<i>Total Depressions:</i> 110	<i>True Positives</i>	<i>True Negatives</i>	
<i>Predicted Positives</i>	28	22	Commission Error: 44%
<i>Predicted Negatives</i>	3	57	Omission Error: 5%
			<i>Overall Accuracy:</i> 77.3%

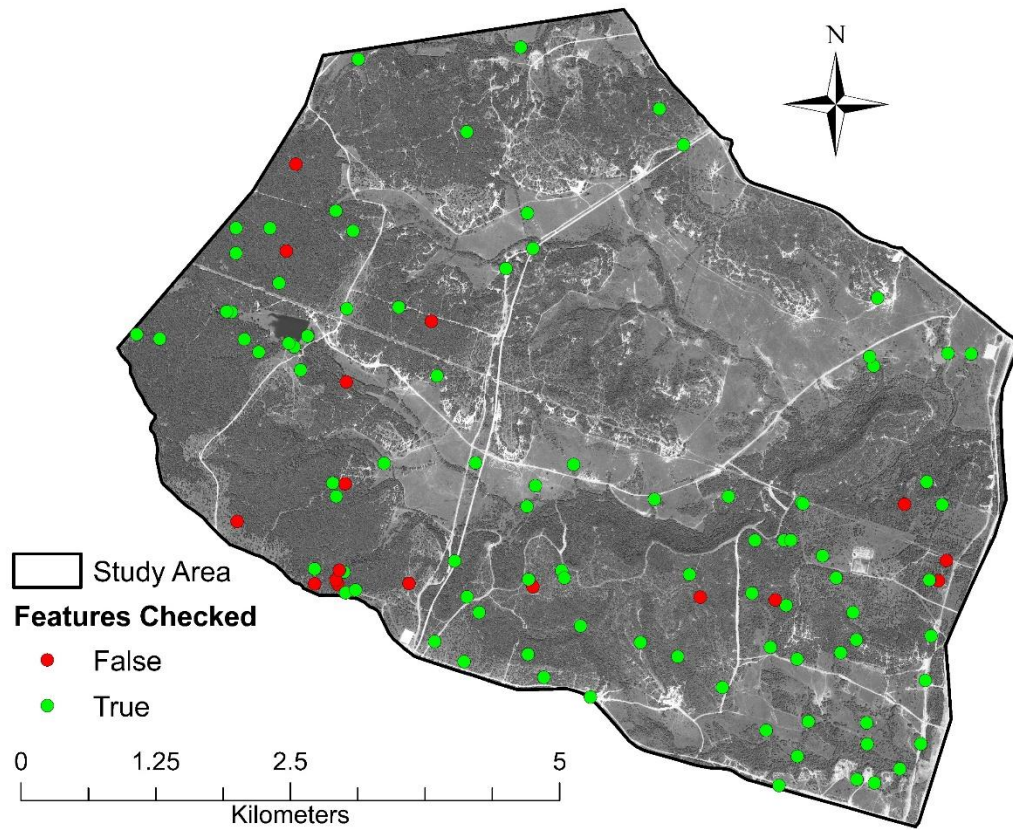


Figure 43: Map showing the location of the random evaluation points that were verified as true and false features with the new filters and buffering parameters (n=107) The DOQQ digital aerial imagery was collected by the National Agriculture Imagery Program during the 2018 agricultural growing season and through the winter and spring of 2019. They were downloaded from the Texas Natural Resources Information Systems on August 30, 2019.

of the 50 points that were said to be true features 17 of these features were classified wrong, which gave a commission error of 66%. The 33 features that agreed with the filtering parameters consisted of true features that were confirmed as true karst features in both datasets and field verifications and true karst features that were actually false positives in the field that now would have been removed from the database with the new filters and buffering parameters. Figure 44 shows examples of depressions that were positively identified in both models. Out of the 57 removed features, all 57 of these features were confirmed as features that should be filtered from the database, which gave an omission error of 100%. Figure 45 shows examples of features removed from the filtering processes in both models. The overall true accuracy of the model with the new filters and buffering parameters was 84.1% and the Kappa statistic was 67.4% (Table 8).

Remote Verification

A remote verification was conducted to further verify that the new filters and buffering parameters were in fact removing features influenced by infrastructure, water bodies, and anthropogenic processes. The Create Random Points tool was used to select 10 features from each filter, excluding the area filter. These points were verified using the same digital aerial image that was used for digitizing roads, water bodies, and land cover (Figure 46). Out of 100 points 89 of them were verified and 11 of them could not be verified based on the



Figure 44: A subsidence feature that was detected by the LiDAR survey and verified during the random point sample survey and agreed with both sets of filters and buffering parameters.



Figure 45: An example of a feature that was delineated during the depression identification process, but removed by the water body filter in both sets of filters and buffering parameters.

Table 8: Confusion matrix with the features that were surveyed to assess the accuracy of the new filters and buffering parameters.

<i>Total Depressions:</i> 107	<i>True Positives</i>	<i>True Negatives</i>	
<i>Predicted Positives</i>	33	17	Commission Error: 66%
<i>Predicted Negatives</i>	0	57	Omission Error: 100%
			<i>Overall Accuracy:</i> 84.1%

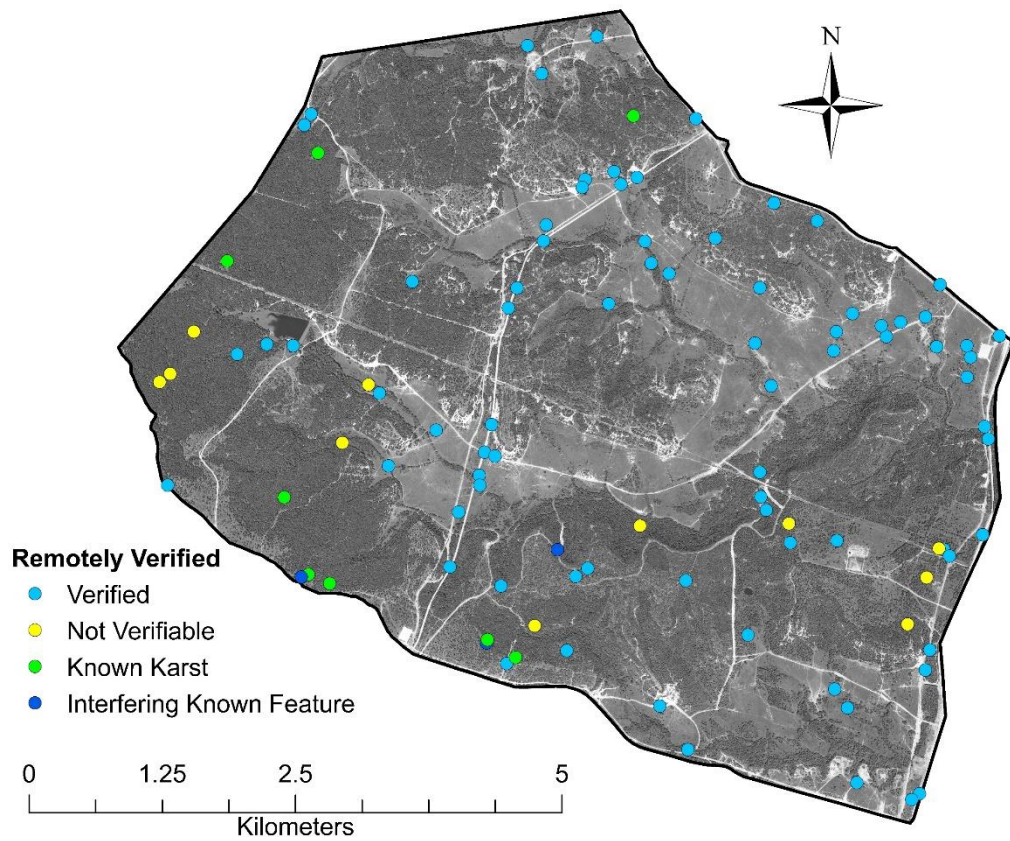


Figure 46: Map showing the location of the remote verification points (n=111). The DOQQ digital aerial imagery was collected by the National Agriculture Imagery Program during the 2018 agricultural growing season and through the winter and spring of 2019. They were downloaded from the Texas Natural Resources Information Systems on August 30, 2019.

digital aerial imagery. Known karst features that were identified in previous karst studies were also remotely verified to see if they interfered with any of the new filters and buffering parameters. Out of the 11 known karst features, three features interfered with the minor roads filter. The minor roads filters are problematic because the area is frequently modified by military activities as new minor roads are continually created and aerial imagery used to digitize minor roads cannot pick up smaller trails masked by dense vegetation.

DISCUSSION

LiDAR surveys result in high-density and high-accuracy datasets that can be used to create models to delineate and characterize karst depressions in areas of interest. This high-density data produces complex models where error within the model is likely to occur. When characterizing features over large areas, these high-density datasets can impose some complications. The 0.5 m resolution LiDAR data used for this study was collected in March 2015 and had a vertical accuracy of 0.077 m. Any feature with a depth less than 0.077 m could not be accurately identified in this model. Over 60,000 possible karst features resulted from using the fill-difference method. After incorporating a new set of filtering mechanisms to remove features based on their spatial relationship to natural and anthropogenic influences, 4,886 features remained as being potential sinkholes that met the size, depth, and location criteria.

Many karst features have been previously discovered at Fort Hood. Due to the use of heavy machinery and military training activities, the land in western Fort Hood is continually altered. During the four months that field work was conducted, seasonal changes reduced the vegetation density (Figure 47 and Figure 48). Ground cover increased associated with defoliation, deforestation, mulching, and controlled burns conducted in training areas (Figure 49 and Figure



Figure 47: The vegetation in the study area during the peak growing season (September 2019).



Figure 48: The vegetation defoliation during the winter season (December 2019).



Figure 49: An area where deforestation and mulching has been done.



Figure 50: An area where recent controlled burns were conducted.

50). During field verifications, locating true potential karst features was challenging since the LiDAR data used to create the model was collected nearly five years ago, and anthropogenic modifications associated with military land use and road building have continued, which altered the training areas.

The greatest error in the random point sample for both the previous and new filters and buffering parameters came from the association of depressions with minor roads that had not been identified during the digitization processes and the land cover filter because areas are always being modified by military activity. Unlike paved major roads that have not changed much in the past few years, minor roads are being continually modified associated with military training area access. Some of the minor roads were hidden in areas of dense vegetation, which made it difficult to recognize them from the 60-centimeter high resolution digital aerial imagery acquired from TNRIS. Error came from the removal of land cover types because training areas can be altered for military exercises in a relatively short period of time, which allows for some discrepancies between data sources. Areas included in the land cover filter were classified with intensity images that were included with the LiDAR data acquired from 2015 and the 60-centimeter high resolution digital aerial imagery from 2018 acquired from TNRIS. The filters used for removing depressions associated with natural features contained less error; streams and bodies of water tend to change very slowly over time, and the underlying lithology in the area remains constant.

However, formation contacts in the study area not always accurate when compared to areas in the field and elevation.

CONCLUSIONS

The use of LiDAR data to delineate and characterize karst depressions in large areas has become more common. These surveys are able to accurately identify any feature that is larger than the survey resolution and greater than the vertical accuracy. This 0.5-meter resolution model detected over 60,000 possible features and after filtering based on spatial relationships to natural and anthropogenic activities, 4,886 features remained that met the size and depth requirements. Any feature within this data set that had a diameter less than 0.5 meters and a depth less than the 0.077-meter vertical accuracy could not be accurately interpreted and was omitted from the model.

Based on the field traverses, many of the features identified did not meet the size or depth requirements for the survey and therefore would have been removed from the potential karst features database. Many of the features identified during the random field checks had very shallow depths or were located in areas that had been recently modified, making it difficult to determine whether the feature was truly a karst feature or an artifact resulting from training activities or heavy machinery.

As for the filters and buffering parameters. The lithology of the area does not change; however, field mapping of the geology should be conducted to have

a more accurate representation of the formation contacts. Land cover and minor roads filters are problematic and must continuously be updated with new data for digitizing with the frequency of training area modifications due to military activities. A newer intensity image along with field checks for land cover should be used to update that filter. Paved roads remain consistent; however, unpaved roads used to access training areas change often and should be reevaluated every time a new study begins. Depending on the type of equipment that travels on minor roads, they can vary in their width, drainage infrastructure, and frequency of use. As for streams and water bodies, they do not change very often. However, they should still be analyzed in greater detail when it comes to categorizing their morphology, and should be updated with newer data for digitizing the features.

Although LiDAR can be a very useful tool for delineating karst features, the survey area needs to be taken into consideration. The ideal places for LiDAR analyses are areas that are not being constantly altered, and only changed by natural influences. For places like the Fort Hood Military Installation that are continually modified, the use of LiDAR data is not applicable unless it is (1) a recently conducted LiDAR survey, (2) has a high resolution to pick up smaller features, and (3) used in areas that are not being constantly altered.

FUTURE WORK

Airborne LiDAR Surveys have proven to be a useful tool in delineating and characterizing karst features. The implementation of filtering mechanisms is used to determine the origin of these features as being karst features through karst processes or features that are influenced by infrastructure, water bodies, and anthropogenic processes. Further studies are required to refine some of these filtering mechanisms to hopefully create a more accurate model for delineating karst features. Geologic mapping of the formation contacts should be done to create a more accurate lithology filter. Another future study could be a major lineament analyses and their influence on karst development in western Fort Hood. Future areas of research should include the western side of the installation to confirm with further field verifications that these filters and buffering parameters do in fact improve filtering of naturally and anthropogenically formed features. Models such as these can also be used to delineate features in the impact range where live fire training is conducted and access to the area is limited.

REFERENCES

- Adkins, W.S., and M.B. Arick, 1930, *Geology of Bell County, Texas*. The University of Texas Bulletin No. 3016, Austin: Bureau of Economic Geology.
- Amsbury, D.L., T.A. Jr. Bay, and F.E. Lozo, 1984, *A Field Guide to Lower Cretaceous Carbonate Strata in the Moffatt Mound Area near Lake Belton, Bell County, Texas*. Guidebook for SEPM Field Trip NO. 3. San Antonio: Gulf Coast Section of the Society of Economic Paleontologists and Mineralogists Foundation, 1-19.
- Anaya, R., 2004, *Conceptual Model for the Edwards-Trinity (Plateau) Aquifer System, Texas*. Report 360, Texas Water Development Board, 21-58 p.
- Anaya, R., and Jones, I., 2009, *Groundwater Availability Model for the Edwards-Trinity (Plateau) and Pecos Valley Aquifers of Texas*. Report 373, Texas Water Development Board, p. 103.
- Barker, R.A., Bush, P.W., Baker, E.T. Jr., 1994, *Geologic History and Hydrogeologic Setting of the Edwards-Trinity Aquifer System, West-Central Texas*. U.S. Geological Survey: Water-Resources Investigations Report 94-4039, p. 1-55.
- Bradley, R.G., Malstaff, G., 2004, *Dry Periods and Drought Events of the Edwards Plateau, Texas*. Austin (TX): Texas Water Development Board.
- Bryant, A.W., 2012, *Geologic and Hydrogeologic Characterization of Groundwater Resources in the Fredericksburg Group, North Nolan Creek Province, Bell County, Texas*. Master's Thesis, Nacogdoches: Stephen F. Austin State University.
- Colligan, J., 1951, *Geology of Belton Reservoir Area, Leon River, Bell County, Texas*. East Texas Geological Society, p. 24-28.
- Collins, E.W., 2005, *Geologic Map of the West Half of the Taylor, Texas, 30 x 60 Minute Quadrangle: Central Texas Urban Corridor, Encompassing Round Rock, Georgetown, Salado, Briggs, Liberty Hill, and Leander*. Miscellaneous Map No. 43, Bureau of Economic Geology, 16 p.

- Ehrhart, J. T., 2016, Speleogenesis and Delineation of Megaporosity and Karst Geohazards Through Geologic Cave Mapping and LiDAR Analyses Associated with Infrastructure in Culberson County, Texas. Master's Thesis, Nacogdoches: Stephen F. Austin State University.
- Elliot, W.R., and Veni, G., 1994, *The Caves and Karst of Texas*, in *Convention of the National Speleological Society*, 1994 guidebook: National Speleological Society and Texas Parks and Wildlife Department, p. 26-28.
- ESRI, 2020, ArcGIS Desktop 10 Resource Center. <https://support.esri.com/en/Products/Desktop/arcgis-desktop> (first accessed January 2019).
- Faulkner, M.G., McBroom, M.W., Farrish, K.W., Stafford, K.W., 2019, *Structural Control of Mesic Vegetation Communities within the Owl and Bear Creek Watersheds, Fort Hood Military Installation, Texas*. JOURNAL OF GEOGRAPHY AND EARTH SCIENCES. 7. 10.15640/jges.v7n1a1.
- Faulkner, M. G., 2016, *An Investigation of Hydrogeologic, Stratigraphic, and Structural Controls on Acer Grandidentatum Communities In a Karst Landscape, Owl Mountain Province, Fort Hood Military Installation, Texas*. SFA Scholar Works, p. 15-24.
- Faulkner, M. G., Stafford, K. W., Bryant, A. W., 2013, "*Delineation and Classification of Karst Depressions Using LiDAR: Fort Hood Military Installation, Texas*". *Faculty Publications*. 2.
- Ferrill, D.A., and Morris, A.P., 2008, Fault Zone Deformation Controlled by Carbonate Mechanical Stratigraphy, Balcones Fault System, Texas: American Association of Petroleum Geologists Bulletin, v. 92, no. 3, pp. 359-380.
- Ferrill, D.A., Sims, D.W., Morris, A.P., Franklin, N.M., Schultz, A.L., 2004, Structural Framework of the Edwards Aquifer Recharge Zone in South-Central Texas: Geological Society of America Bulletin, v. 116, no. 3/4, pp. 407-418.
- Fisher, W.L., and Rodda, P.U., 1969, *Edwards Formation (Lower Cretaceous), Texas: Dolomitization in a Carbonate Platform System*. American Association of Petroleum Geologists 53, no. 1: p 55-72.
- Flood, Flood, M., 2004, *ASPRS Guidelines Vertical Accuracy Reporting for LiDAR Data*, ASPRS, p. 1-20.

- Ford, D.C., and Williams, P., 2007, *Karst Hydrogeology and Geomorphology*, Wiley, p. 339-351.
- Fugro Earthdata INC., 2011, *LiDAR Mapping Fact Sheet*, FurgroEarthdata, INC., p. 1-5
- Hammer, M.L., 2011, *Introduction and site description, in Endangered Species Monitoring and Management at Fort Hood, Texas*. Fort Hood: Fort Hood, Directorate of Public Works, Natural Resources Management Branch.
- Hu, Y., 2003, *Automated extraction of digital terrain models, roads and buildings using airborne LiDAR data*, University of Calgary, Department of Geomatics Engineering, pp. 85-88.
- Jones, I.C., 2003, *Groundwater Availability Model: Northern Segment of the Edwards Aquifer, Texas*. Report 358, Austin: Texas Water Development Board, p. 75.
- Kao, D., Kramer, M., Luo, A., Dungan, J., and Pang, A., 2005, *Visualizing Distributions from Multi-Return LiDAR Data to Understand Forest Structure*, *The Cartographic Journal*, Vol. 42, No. 1, pg. 35-47.
- Klimchouk, A.B., 2007, *Hypogene Speleogenesis: Hydrogeological and Morphogenetic Perspective*. Special Paper no.1, National Cave and Karst Research Institute, Carlsbad, NM, 106 pp.
- Klimchouk, A.B., 2009, *Principal Characteristics of Hypogene Speleogenesis, in Advance in Hypogene Speleogenesis, Symposium 1*, National Cave and Karst Research Institute, p. 1-11.
- Lui, X., 2008, *Airborne LiDAR for DEM Generation: Some Critical Issues*, *Progress in Physical Geography*, Vol. 32, No. 1, p. 1-49.
- Lui, H., and Wang, L., 2008, *Mapping Detection Basins and Deriving Their Spatial Attributes from Airborne LiDAR Data for Hydrological Applications*, Vol. 22, *Hydrological Processes*, p. 2358-2369.
- Nelson, H.F., 1973, "The Edwards Reef Complex and Associated Sedimentation." *The Geological Society of America*. Dallas: Bureau of Economic Geology, 1-35.
- Pugsley, W S., 2001, *Imprint on the Land, Life Before Camp Hood, 1820-1942*,. Prewitt and Associates.

- Quantum Spatial, 2015, *Field Survey Report of Photo ID Ground Control Points*, Quantum Spatial Inc.
- Reddell, J.R., Fant, J., Reyes, M., and Warton, M., 2011, *Karst Research on Fort Hood, Bell and Coryell Counties, Texas*. Unpublished Report, Fort Hood: Fort Hood Natural Resources Management Branch.
- Reece, C., 2018, *Delineation of Karst Potential Using LiDAR and GIS Analyses Fort Hood Military Installation, Coryell County, Texas*. Master's Thesis, Nacogdoches: Stephen F. Austin State University.
- Rose, P.R., 1972. *Edwards Group, Surface and Subsurface, Central Texas*, Report of Investigations, no. 74, Bureau of Economic Geology, 198 p.
- Senger, R. K., Kreidler, C.K., Collins, E.W., 1990, *Hydrogeology of the Northern Segment of the Edwards Aquifer, Austin Region*, Report of Investigations, no. 192, Bureau of Economics Geology, p 1-56.
- Tibouo, F.N., 2016, *Use and Elevation of LiDAR for Mapping Sinkholes in Royal Spring Groundwater Basin*, University of Kentucky Master's Theses Graduate School.
- Veni, G., 1994, *Hydrogeology and Evolution of Caves and Karst in the Southwestern Edwards Plateau, Texas*. The Caves and Karst of Texas, National Speleological Society, Huntsville, Alabama. 252 pp.
- Walker, L.E., 1979, *Occurrence, Availability, and Chemical Quality of Ground Water in the Edwards Plateau Region of Texas*, Report 235, Texas Department of Water Resources, p. 336.
- Wermund, E.G., 1996, *Physiographic Map of Texas*, Bureau of Economic Geology, 1 sheet.
- Wu, Q., Deng, C. and Chen, Z., 2016, *Automated Delineation of Karst Sinkholes from LiDAR-Derived Digital Elevation Models*, *Geomorphology*, vol. 226, p. 1-10.

APPENDIX (A) DATA

TRAVERSE FEATURES IDENTIFIED

Traverse lines were established to ensure that all types of areas included in filtering mechanisms were covered in order to include smaller features that may not have been picked up by the LiDAR survey. The traverse survey was conducted by walking three sections of north-south trending traverse lines from the top to bottom edges of the study area. There was a section of traverses running through the east side, middle, and west side of the study area to be sure that it was adequately surveyed. Each section covered 100 meters and was traversed in increments of 10 meters, and included 11 traverse lines for each section.

A total of 157 karst features including sinkholes, caves, shelter caves and solutional conduits augmented by root structures, were recorded during the field traverses. These features were typically located on the ridges and plateaus, topographically high areas capped by the Edwards Formation and along the hydrogeologic boundary between the Edwards and Comanche Peak formations.

Traverse 1

The first section of traverses were located on the eastern side of the study area. A total of 68 features were identified and included 3 shelter caves, 35

sinkholes, and 30 root holes. Table 8 shows geometric properties and classification of each feature identified in traverse 1.

Traverse 2

The second section of traverses were located in the middle part of the study area. A total of 33 features were identified and include 27 sinkholes, and 6 root holes. Table 9 shows geometric properties and classification of each feature identified in traverse 2.

Traverse 3

The third section of traverses were located on the western side of the study area. A total of 56 features were identified and include 25 sinkholes, and 31 root holes. Table 10 shows geometric properties and classification of each feature identified in traverse 3.

Table 9: Summary table of the geometric properties for each karst feature found in traverse survey 1.

Name	Classification	Azimuth	Length (m)	Width (m)	Depth (m)	Circularity
T1.1	Sinkhole	42	0.3048	0.2032	0.4064	1.5
T1.2	Depression	-	0.3556	0.3556	0.1016	1.0
T1.3	Depression	70	0.3810	0.1778	0.0508	2.1
T1.4	Root Hole	-	0.3048	0.3048	0.4064	1.0
T1.5	Root Hole	-	0.5080	0.2540	0.3048	2.0
T1.6	Root Hole	72	0.3556	0.2540	0.4572	1.4
T1.7	Root Hole X9	-	0.1524	0.1524	0.2540	1.0
T1.8	Depression	-	0.2794	0.2794	0.1778	1.0
T1.9	Root Hole	-	0.3048	0.3048	0.7366	1.0
T1.10	Sinkhole	-	0.4064	0.4064	0.3048	1.0
T1.11	Sinkhole	-	0.3302	0.3302	0.1524	1.0
T1.12	Sinkhole	-	0.1524	0.1524	0.2540	1.0
T1.13	Root Hole	-	0.2286	0.2286	0.4572	1.0
T1.14	Root Hole	39	0.3048	0.2032	0.2286	1.5
T1.15	Root Hole	-	0.1270	0.1270	0.3048	1.0
T1.16	Root Hole	-	0.3048	0.3048	0.2540	1.0
T1.17	Sinkhole	20	0.4064	0.3556	0.4064	1.1
T1.18	Depression	-	0.5080	0.5080	0.0762	1.0
T1.19	Root Hole	-	0.6096	0.6096	0.6350	1.0
T1.20	Root Hole	129	0.4572	0.2286	0.4826	2.0
T1.21	Root Hole	-	0.2286	0.2286	0.3810	1.0
T1.22	Shelter Cave	61	1.5240	0.6096	0.3048	2.5
T1.23	Sinkhole	-	0.1524	0.1524	0.2032	1.0
T1.24	Depression	-	0.3556	0.3556	0.1016	1.0
T1.25	Root Hole	37	0.2286	0.1524	0.3048	1.5
T1.26	Depression	-	1.2192	1.2192	0.2794	1.0
T1.27	Depression	61	1.8288	1.5240	0.1524	1.2
T1.28	Depression	-	0.8636	0.8636	0.2286	1.0
T1.29	Sinkhole	-	0.3048	0.3048	0.6096	1.0
T1.30	Root Hole	28	0.3048	0.1524	0.2286	2.0
T1.31	Depression	-	1.9812	1.9812	0.4064	1.0
T1.32	Depression	35	0.7620	0.3556	0.1016	2.1
T1.33	Sinkhole	117	0.1524	0.1016	0.2540	1.5
T1.34	Depression	157	1.3208	0.9144	0.3048	1.4

Table 9: (continued)

T1.35	Depression	-	0.7112	0.7112	0.1270	1.0
T1.36	Root Hole	104	0.3048	0.1524	0.1778	2.0
T1.37	Root Hole	25	0.2286	0.1524	0.3302	1.5
T1.38	Depression	-	0.4064	0.4064	0.0762	1.0
T1.39	Root Hole	31	0.2540	0.1524	0.1524	1.7
T1.40	Root Hole	23	0.2286	0.1270	0.5080	1.8
T1.41	Root Hole	87	0.2540	0.1016	0.7366	2.5
	Root Hole	-	0.1016	0.1016	0.4572	1.0
T1.42	Root Hole	59	0.3048	0.2032	0.9144	1.5
T1.43	Depression	53	0.1524	0.1016	0.1905	1.5
T1.44	Root Hole	48	0.4826	0.1270	0.8636	3.8
T1.45	Root Hole	54	2.1336	1.0414	3.5052	2.0
T1.46	Sinkhole	-	0.4064	0.4064	0.2286	1.0
T1.47	Depression	-	0.3048	0.3048	0.2032	1.0
	Sinkhole	-	0.2032	0.2032	0.2286	1.0
T1.48	Root Hole	116	0.1270	0.0762	0.2540	1.7
T1.49	Shelter Cave	31	7.7724	0.7620	3.0480	10.2
T1.50	Shelter Cave	7	3.6576	0.8128	1.5748	4.5
T1.51	Sinkhole	-	0.4318	0.4318	1.4224	1.0
T1.52	Root Hole	8	0.2032	0.1270	0.2540	1.6
T1.53	Root Hole	52	0.2032	0.1524	0.2286	1.3
T1.54	Sinkhole	23	0.2032	0.1270	0.2032	1.6
T1.55	Depression	-	0.0762	0.0762	0.2032	1.0
T1.56	Root Hole	57	0.3048	0.2032	0.5080	1.5
T1.57	Sinkhole	-	0.4572	0.4572	0.1524	1.0
T1.58	Depression	-	0.2032	0.2032	0.0762	1.0
T1.59	Root Hole	127	0.2540	0.2032	0.4064	1.3
T1.60	Root Hole	-	0.1016	0.1016	0.2540	1.0
T1.61	Root Hole	-	0.1270	0.1270	0.2667	1.0
T1.62	Root Hole	64	0.4572	0.3556	0.6096	1.3
T1.63	Sinkhole	-	0.4064	0.4064	0.3048	1.0
T1.64	Depression	-	0.6096	0.6096	0.2540	1.0
T1.65	Depression	-	0.3048	0.3048	0.2032	1.0
T1.66	Depression	-	0.4572	0.4572	0.7620	1.0
T1.67	Sinkhole	-	0.1270	0.1270	0.1778	1.0
T1.68	Depression	-	0.3048	0.3048	0.1524	1.0

Table 10: Summary table of the geometric properties for each karst feature found in traverse survey 2.

Name	Classification	Azimuth	Length (m)	Width (m)	Depth (m)	Circularity
T2.1	Root Hole	28	0.1270	0.0254	0.0762	5.0
T2.2	Depression	12	1.2192	0.7620	0.1016	1.6
T2.3	Root Hole	155	0.4572	0.3810	0.2540	1.2
T2.4	Depression	39	1.5240	1.0668	0.0762	1.4
T2.5	Sinkhole	-	0.6096	0.6096	0.4064	1.0
T2.6	Root Hole	128	0.2286	0.2032	0.4318	1.1
T2.7	Root Hole	148	0.2540	0.1778	0.5080	1.4
T2.8	Depression	17	1.2192	1.0922	0.1016	1.1
T2.9	Depression	-	1.2192	1.2192	0.1270	1.0
T2.10	Depression	154	0.5080	0.4572	0.1524	1.1
T2.11	Depression	-	0.9144	0.9144	0.3048	1.0
T2.12	Depression	-	3.0480	3.0480	0.4318	1.0
T2.13	Root Hole	-	0.4826	0.3048	0.4572	1.6
T2.14	Root Hole	72	0.4064	0.1778	0.3810	2.3
T2.15	Depression	126	0.8128	0.6604	0.2286	1.2
T2.16	Sinkhole	-	0.7366	0.7366	0.4572	1.0
T2.17	Depression	-	0.9652	0.9652	0.3810	1.0
T2.18	Depression	-	0.6096	0.6096	0.1270	1.0
T2.19	Sinkhole	-	0.3048	0.3048	0.4826	1.0
T2.20	Sinkhole	7	0.3556	0.3048	0.2286	1.2
T2.21	Depression	142	1.2192	1.0922	0.1143	1.1
T2.22	Depression	-	1.5240	1.5240	0.1524	1.0
T2.23	Depression	68	0.7112	0.4826	0.2286	1.5
T2.24	Depression	-	0.9144	0.9144	0.3048	1.0
T2.25	Depression	167	0.7620	0.6096	0.1016	1.3
T2.26	Depression	-	1.2192	1.2192	0.1524	1.0
T2.27	Depression	-	1.5240	1.5240	0.1524	1.0
T2.28	Depression	9	0.7112	0.4826	0.1270	1.5
T2.29	Depression	-	1.2192	1.2192	0.2032	1.0
T2.30	Sinkhole	-	0.3302	0.3302	0.3302	1.0
T2.31	Depression	-	1.3208	1.3208	0.1778	1.0
T2.32	Depression	-	0.9398	0.9398	0.1016	1.0
T2.33	Depression	135	0.8382	0.5334	0.2032	1.6

Table 11: Summary table of the geometric properties for each karst feature found in traverse survey 3.

Name	Classification	Azimuth	Length (m)	Width (m)	Depth (m)	Circularity
T3.1	Root Hole	21	0.4826	0.4318	0.3048	1.1
T3.2	Depression	8	1.0922	1.0160	0.1524	1.1
T3.3	Depression	117	1.0414	0.9652	0.1270	1.1
T3.4	Sinkhole	50	0.7874	0.1778	0.7112	4.4
T3.5	Root Hole	75	0.4318	0.3302	0.3048	1.3
T3.6	Root Hole	55	0.5080	0.2032	0.4318	2.5
T3.7	Root Hole	8	0.4318	0.1524	0.3810	2.8
T3.8	Root Hole	13	0.3302	0.1016	0.3048	3.3
T3.9	Root Hole	155	0.4572	0.3556	0.3556	1.3
T3.10	Sinkhole	-	0.2032	0.2032	0.2286	1.0
T3.11	Root Hole	168	0.3048	0.1778	0.3048	1.7
T3.12	Sinkhole	9	0.3810	0.1778	0.4064	2.1
T3.13	Sinkhole	-	0.2794	0.2794	0.1778	1.0
T3.14	Root Hole	57	0.2794	0.1778	0.3048	1.6
T3.15	Root Hole	32	0.4064	0.3556	0.2540	1.1
T3.16	Root Hole	5	0.3810	0.2540	0.4064	1.5
T3.17	Root Hole	131	0.3048	0.2032	0.1778	1.5
T3.18	Depression	22	6.0960	4.4450	0.5334	1.4
T3.19	Depression	-	0.5334	0.5334	0.1016	1.0
T3.20	Root Hole	37	0.2540	0.1524	0.2794	1.7
T3.21	Root Hole	-	0.1016	0.1016	0.1778	1.0
T3.22	Sinkhole	161	0.3810	0.2794	0.4318	1.4
T3.23	Root Hole	33	0.3810	0.2794	0.2794	1.4
T3.24	Root Hole	1212	0.5080	0.4318	0.1524	1.2
T3.25	Root Hole	61	0.3048	0.1524	0.3556	2.0
T3.26	Sinkhole	-	0.3048	0.3048	0.2286	1.0
T3.27	Sinkhole	31	0.2540	0.1524	0.1016	1.7
T3.28	Root Hole	5	0.3810	0.1524	0.3556	2.5
T3.29	Root Hole	8	0.4064	0.1524	0.4318	2.7
T3.30	Root Hole	104	0.3048	0.2286	0.3810	1.3
T3.31	Root Hole	128	0.1524	0.1016	0.2540	1.5
T3.32	Root Hole	101	0.4064	0.3048	0.3048	1.3
T3.33	Sinkhole	160	0.4064	0.3048	0.5588	1.3
T3.34	Depression	-	1.0414	1.0414	0.2540	1.0

Table 11: (continued)

T3.35	Root Hole	-	0.6604	0.6604	0.4826	1.0
T3.36	Sinkhole	-	0.4826	0.4826	0.3302	1.0
T3.37	Sinkhole	-	0.5334	0.5334	0.1778	1.0
T3.38	Sinkhole	63	0.3810	0.3048	0.5334	1.3
T3.39	Sinkhole	-	0.4826	0.4826	0.4572	1.0
T3.40	Root Hole	-	0.5080	0.5080	0.2794	1.0
T3.41	Depression	36	2.5400	1.2700	0.5588	2.0
T3.42	Depression	65	2.1336	0.9906	0.2794	2.2
T3.43	Root Hole	-	0.3048	0.3048	0.1778	1.0
T3.44	Root Hole	62	0.6350	0.5842	0.7874	1.1
T3.45	Root Hole	-	0.3302	0.3302	0.2032	1.0
T3.46	Root Hole	-	0.3302	0.3302	0.1524	1.0
T3.47	Root Hole	-	0.4064	0.4064	0.4572	1.0
T3.48	Depression	114	0.8890	0.4318	0.1016	2.1
T3.49	Root Hole	-	0.6096	0.6096	0.4064	1.0
T3.50	Root Hole	-	0.5080	0.5080	0.3302	1.0
T3.51	Root Hole	-	0.3048	0.3048	0.2032	1.0
T3.52	Depression	31	0.2540	0.1270	0.2286	2.0
T3.53	Depression	57	0.5080	0.3556	0.4826	1.4
T3.54	Depression	-	1.4224	1.4224	0.1143	1.0
T3.55	Depression	64	1.4224	0.8128	0.1524	1.8
T3.56	Sinkhole	-	0.3302	0.3302	0.3302	1.0

VITA

Heather J. Dailey graduated from Klein Oak High School in Spring, Texas in May of 2012. Heather attended Houston Baptist University in fall of 2012. In the spring of 2013 Heather began attending Stephen F. Austin State University in Nacogdoches, Texas where she received her Bachelor of Science in Geology with a General Business minor in August 2017. After receiving her bachelor's degree Heather began pursuing a Master of Science in Geology with a Spatial Science minor. Heather will receive her Master of Science degree in May, 2020.

Permanent Address:

16407 Solvista Hill Court.

Houston, Texas 77044

Style manual designation: Geological Society of America

This thesis was typed by Heather J. Dailey